Self-Mixing Diode Laser Interferometry

A thesis submitted to the

University of Waikato

for the degree

of

Masters of Engineering

by

Pawan Kumar Shrestha

THE UNIVERSITY OF
WAIKATO
Te Whare Wānanga o Waikato

Hamilton, New Zealand

Feburary 2010

Dedicated to
my dad

Abstract

Self-mixing interferometry in a laser diode is a very powerful tool in measurement science. The Self-mixing interferometer is a very robust and low cost interferometer with extreme simplicity in alignment and setup. In this thesis, a self-mixing interferometer is analysed and developed. The measurements of the self-mixing interferometer are verified using a Michelson interferometer. It is then followed by the signal processing of the detected signal. Three different methods are developed to retrieve the movement of the target. Results obtained by applying these methods to different experimental data sets are presented.

In the later part of the thesis, a phase locked self-mixing interferometer is developed. This slightly modified interferometer follows the target movement. As a result no additional circuitry or signal processing is necessary for the recovery of the target movement. Phase locked interferometer developed in this thesis was able to measure down to 1 nm of vibration. It is then followed by a novel method to detect cracks in eggshells using the phase locked vibrometer. The proposed method is tested and proved to be capable of differentiating between the intact and cracked eggs.

Acknowledgements

This thesis would not have been possible without the help and support of many amazingly helpful people, and I owe my deepest gratitude to them. It was an honor for me to do this research under the supervision of Associate Professor Dr. Rainer Künnemeyer. I am really grateful for his guidance and support. His valuable feedback helped me throughout the research and writing of this thesis. Despite his busy schedule, Dr. Künnemeyer always had time and patience for my problems.

I would also like to thank Professor Jonathan Scott, Senior Lecturer Nihal Kularatna and Dr. Adrian Dorrington for their ideas and fruitful discussions we had. Also thanks to Dr. Michael Cree for helping me with programming in Matlab and helping me understand the Wavelet principles. To Dr. Paul Martinson from Hort Research, I am more than grateful for many discussions we had and his generosity in lending the equipment. I also owe my gratitude to the technical staff of the Department of Engineering. In particular I would like to thank Stewart Finlay for letting me use equipment from his laboratory. Thanks to Yuanji Zhang, Peter Jarman, Viking Zhou, David Nicholls and Ian Honey for all the support you have provided in numerous ways. I would also like to thank Biju Cletus for all the timely help and ideas about experiments. I am indebted to Matthew O'Donnell of Newport Corporation, USA, for his guidance in building the phase locked vibrometer. His thesis and email communications served as a light at the end of the tunnel during this research.

Words are not enough to describe the love and support I received from my wife Prajina. I appreciate her continuous encouragement to write the thesis on time and not to get carried away only with research and experiments. I can never thank her enough for her diligent proof reading and understanding me during weekends and late nights. Thanks also to her dad, mum and sisters for enormous encouragement and patience throughout the research. Above all, I would like to thank my mum for her unconditional love and support over the years which has helped me weave my dreams to become who I am.

Contents

List of Figures

Chapter 1

Introduction

Interferometry is a very powerful technique for the precision measurement of displacement, vibration, velocity, etc. in both solids and fluids. In this technique, the light wave is split into two waves. They are delayed by unequal distances and are recombined. Then the intensity of their superposition is detected. The instrument used to interfere the waves is called the interferometer.

In 1801, Thomas Young introduced the idea of the interference of light waves. In 1881, Albert Michelson invented the famous interferometer known as Michelson interferometer (Halliday et al. 2000). The invention of the laser in the 1960's unleashed the full capability of interferometers. It is now applied in mechanical metrology, fluid anemometry, vibrometry, gyroscope, optical fiber sensors, space telemetry, etc. According to the configuration, interferometry can be classified into three different types: external interferometry, internal interferometry and self-mixing interferometry (Donati 2004). This thesis focuses on self-mixing interferometry.

Self-mixing interferometry is also commonly known as injection, feedback or induced modulation interferometry. In this technique a fraction of light reflected or scattered back by the remote target is allowed to re-enter the laser cavity. If the external light is phase shifted, and it is coherently mixed in the original laser light, interference occurs. Since the interference information is carried by the laser beam, it can be easily detected either by the monitor photodiode placed behind the laser or at the remote target location or anywhere in between (Bosch et al. 2001). The main advantage of the self-mixing configuration compared to the conventional interferometry (Michelson, Mach-Zehnder or Sagnac interferometry) is, it is very simple, compact (part count saving) and robust. Since this configuration has only one optical axis, no alignment is necessary. If the monitor photodiode behind the laser is used to monitor the signal, no light filtering is required before the photodiode.

The aim of this research is to investigate the physics behind the self-mixing interference, develop the self-mixing diode laser interferometer in the laboratory,

reconstruct the movement of the target and apply it for the detection of eggshell crack.

In the next chapter laser interferometry and the Doppler effect are introduced. Semiconductor laser diode fundamentals are covered in depth followed by two popular models of self-mixing interferometry namely, the three mirror model and, the Lang and Kobayashi equation. Literature relevant to the research is reviewed in this chapter.

Experimental setups for the velocity and vibration measurement using self-mixing interferometry are presented in chapter three. The measurements for both setups are verified using alternative methods.

Chapter four focuses on the reconstruction of the displacement signal. Three different algorithms are developed in this section and realised using the MATLAB program. Each method is applied in different experimental data sets and results are presented.

A phase locked self-mixing vibrometer is developed in chapter five. Based on the active phase nulling technique, this vibrometer follows the target movement eliminating the need to reconstruct the displacement signal. The vibrometer is capable of measuring displacement far less than half of the wavelength of a laser. The chapter also includes the application of this vibrometer for the detection of eggshell crack in a novel way. The final chapter concludes that the thesis aims have been achieved and discusses possible improvements that can be made in the future.

Chapter 2

Background Theory of Self-Mixing Interferometry

Since the 1980's, the number of papers published in international, peer-reviewed scientific journals on self-mixing interferometry has been increasing with a notable rapid growth in recent years. The numbers confirm that self-mixing is well known and a well established technique among the international scientific community (Giuliani et al. 2002). There are numerous theoretical model devised to explain the self-mixing effect. In this chapter we present the history of the self-mixing effect. This is followed by a brief introduction of interferometry and the Doppler effect. Then we discuss semiconductor laser fundamentals and ultimately two most popular theoretical models: the three mirror model and the Lang-Kobayashi equations of self-mixing in laser diodes.

2.1   Historical Development of Self-Mixing Interference

Back-reflection was recognized as a serious source of disturbance soon after the invention of the laser in 1960 (Bosch et al. 2001). This lead to the discovery of a new exciting field called optical feedback interferometry. The first laser-feedback interferometry device for distance and velocity measurement was demonstrated in 1963 at an exhibition of the Institute of Physics and The Physical Society by King and Steward (King and Steward 1963). In their experimental setup the output from a continuously operated Helium-Neon (He-Ne) laser was modified by an external mirror providing the optical feedback (King and Steward 1963). In 1968, Rudd employed a He-Ne laser to demonstrate the first laser Doppler velocimeter (Rudd 1968). Rudd states that the efficiency of his velocimeter, employing the laser as a mixer oscillator, is comparable to that of a conventional system, such as a Michelson interferometer. The first complete interferometer/vibrometer with up and down fringe counting was reported in 1978 by Donati using a He-Ne laser (Donati 1978).

Waveform asymmetry in a laser Doppler velocimeter was observed by Shimizu in 1987. By employing a series of band-pass filters, he showed that the phase of the second harmonic of the Doppler signal inverts as the target changes the

direction of its movement (Shimizu 1987). However he did not offer a physical explanation for this phenomenon. An optically simple and small laser Doppler velocimeter was described using self mixing diode lasers (Jentink et al. 1988). The authors assumed that the mode pattern of the emitted light is not altered by the optical feedback. However, the beat signal generated in a backscatter-modulated laser diode cannot be adequately explained simply in terms of the coherent mixing of independent light waves of two different optical frequencies. The three-mirror Fabry-Perot cavity model, which is now one of the most popular models, to describe self-mixing interferometry, tried to describe waveform asymmetry. Intensity modulation is explained by the change of the carrier density inside the laser cavity (de Groot et al. 1988). Shinohara et al. (1989) developed a self-mixing type laser Doppler velocimeter (SM-LDV), which was able to measure velocities with directional discrimination in the range of 23 mm·s^{-1} to 23 m·s^{-1}. To date, experimental results for velocities up to 200 km·h^{-1} (i.e. 55 m·s^{-1}) with a maximum relative error of 5% have been observed (Giuliani et al. 2002).

The paper published by Lang and Kobayashi presenting results of experimental and theoretical analysis of the influences of the externally reflected light on the static and dynamic behaviour of semiconductor lasers was one of the turning points in the history of self-mixing interferometry (Lang and Kobayashi 1980). The three mirror model is simple to work with and explains most of the phenomena. But the rate equations first derived by Lang and Kobayashi are more rigorous, fully account for the laser physical parameters including the effects specific to a semiconductor laser and are more complete (Bosch et al. 2001).

de Groot et al. (1988) discovered that the sign of the quasi saw tooth waveform depended on whether one monitored the laser output from the front or back facet. When a beam splitter and second detector were introduced between the focusing lens and the target they found that the signals for the two emission directions were inverted with respect to each other. Similar observation was made by Wang et al. (1993). de Groot et al. (1988) mentioned coherence length as a limiting factor for the range in self-mixing interferometry. Koelink et al. (1992b) also support the coherence length to limit the range of maximum measurable distance using self-mixing. This was later challenged by Wang et al. (1993) supported, through another separate research, by (Bosch et al. 2001).

Self-mixing interferometry can be used to measure vibrations larger than $\lambda / 2$ using the fringe counting technique. With the introduction of phase locked self-mixing interferometry, the resolution has dramatically improved. Suzuki et al. (1999) demonstrated a phase locked self-mixing interferometer. The phase locked vibrometer is based on the idea of locking the interferometer to half a fringe. Research has been carried out by Giuliani et al. (2003) in this area too. The authors claim to experimentally obtain sensitivity of 10 pmHz$^{-1/2}$ and the maximum amplitude of vibration measured to be 180 µm.

The self-mixing signal can be obtained from any type of single-longitudinal mode Fabry Perot laser diode for which the side mode suppression is larger than 7 to 8 dB. Giuliani et al. (2002) have claimed to have successfully tested laser diodes with emission wavelengths ranging from 635 nm to 1550 nm with either Fabry Perot, Distributed Feedback (DFB) or External Cavity (ECL) structures. Gregory et al. (2000) used three electrode distributed Bragg reflector (DBR) structure to measure distance using the self mixing effect. The self-mixing effect has also been observed in multi-quantum well (Suzuki et al. 1999; Wang et al. 2006), vertical-cavity surface-emitting lasers (VCSELs) (Porta et al. 2002; Tucker et al. 2007) and superluminescent diodes (Rovati and Docchio 1998). Jentink et al. (1988) used a multilongitudional mode diode laser for a self-mixing velocimeter. The authors stated the change in amplitude of the Doppler signal when the distance between diode laser and the target was altered. This theory was later supported by Koelink et al. (1992b) in a separate experiment.

Self-mixing interferometry has then been exploited extensively by many research teams in various ways. Lots of work has been published in velocimetry. (Shinohara et al. 1986; Jentink et al. 1987; Callan and McInerney 1992; de Mul et al. 1992; Koelink et al. 1992b; Shibata et al. 1999; Raoul et al. 2004). Papers are published in displacement, distance and vibration measurement as well (Wang et al. 2000; Norgia et al. 2004; Jong Sup and Shylo 2004; Donati et al. 2006; Giuliani et al. 2008). It has also been applied in biomedical optics (de Mul et al. 1992; Koelink et al. 1992a; Ozdemir et al. 1999; Scalise et al. 2001; Hast et al. 2002a, 2002b; Meigas et al. 2003; Zakian et al. 2005; Ozdemir et al. 2008).

2.2   Background Theory

2.2.1 Laser interferometry

Laser interferometry uses the superposition of two or more waves to create interference. The term interference was coined by the British scientist Thomas Young. Young's historic experiment proved the wave nature of light. The discovery of the laser, i.e. coherent source, significantly improved the classical interferometric methods. It also led to new types of interferometric techniques, e.g. holography, Doppler, Sanyak effect, speckle and self-mixing (Karasik et al. 1995).

In this section we start with Young's experiment which shows the relationship between wavelength of light, fringe spacing, spacing between light sources and the distance between source and screen and discuss one of the most popular interferometers, the Michelson interferometer.

2.2.1.1 Young's experiment

Light from a monochromatic point source falls on an opaque mask containing two parallel slits. Each slit thus acts as a source of cylindrical waves. As shown in Figure 1, the expanding cylindrical waves from these two sources are then superposed on the screen placed at the distance D. Points on the screen where the waves from the two slits are in phase appear bright (corresponding to constructive interference) and where the waves are out of phase appear dark (corresponding to destructive interference). So if X_1 and X_2 are the distances from the point on the screen to the two slits, the condition for the maximum constructive interference is just

$$| X_1 - X_2 | = n\lambda \tag{2.1}$$

where λ is the wavelength of light and n=0,1,2... Similarly, destructive interference occurs whenever the distances X_1 and X_2 are

$$| X_1 - X_2 | = (n + \frac{1}{2})\lambda. \tag{2.2}$$
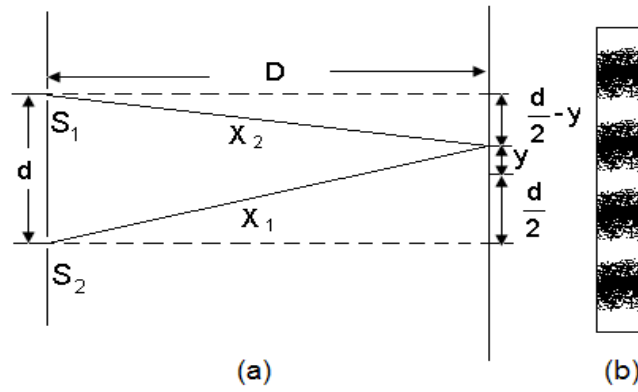
Figure 1 - (a) Geometry used in Young's slits experiment; (b) Dark and bright fringes.

In Figure 1(a) let d be the distance between the two parallel slits and y be any point on the screen. The distance from either of slit from a point on the screen can be calculated as follows.

$$X_1^2 = D^2 + (\frac{d}{2} + y)^2,$$

$$X_2^2 = D^2 + (\frac{d}{2} - y)^2,$$

$$X_1^2 - X_2^2 = 2yd,$$

$$y = \frac{X_1^2 - X_2^2}{2d}.$$

Since, $X_1 + X_2 \approx 2D$ in the farfield

$$y = (X_1 - X_2)\frac{D}{2d}. \qquad (2.3)$$

Substituting equation (2.1) in equation (2.3) for the constructive interference leads to

$$y = n\frac{\lambda D}{d}.$$

Hence the fringe spacing can be given by,

$$\Delta y = \frac{\lambda D}{d}.$$

2.2.1.2 Michelson interferometer

The Michelson interferometer was invented by the American physicist Albert Michelson and used in the 1880s by himself and his colleague Edward W. Morley

in a famous experiment that paved the way for the theory of relativity (Wolfson and Pasachoff 1990).

Figure 2 shows the basic design of the Michelson interferometer and Figure 3 shows the Michelson interferometer setup in the laboratory. The light beam, U_0, from the light source is split by a beam splitter into two beams, U_1 and U_2. Each of them reflects off a flat mirror and returns to the beam splitter where they recombine causing constructive or destructive interference depending on the difference of path length between the two beams.
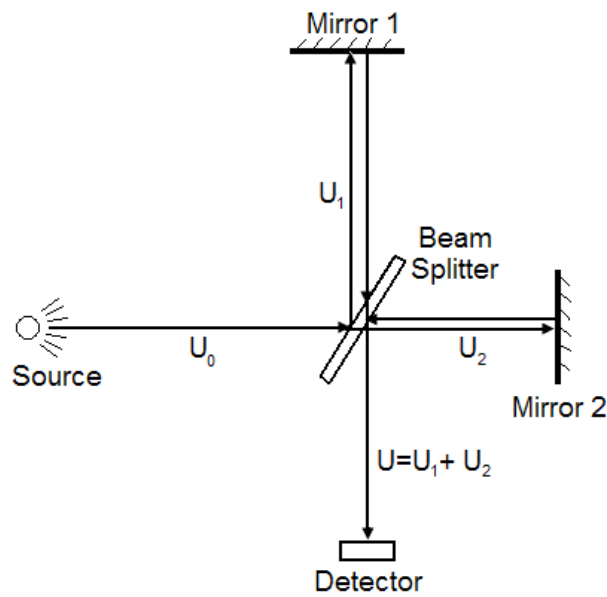
Figure 2 - Michelson Interferometer.
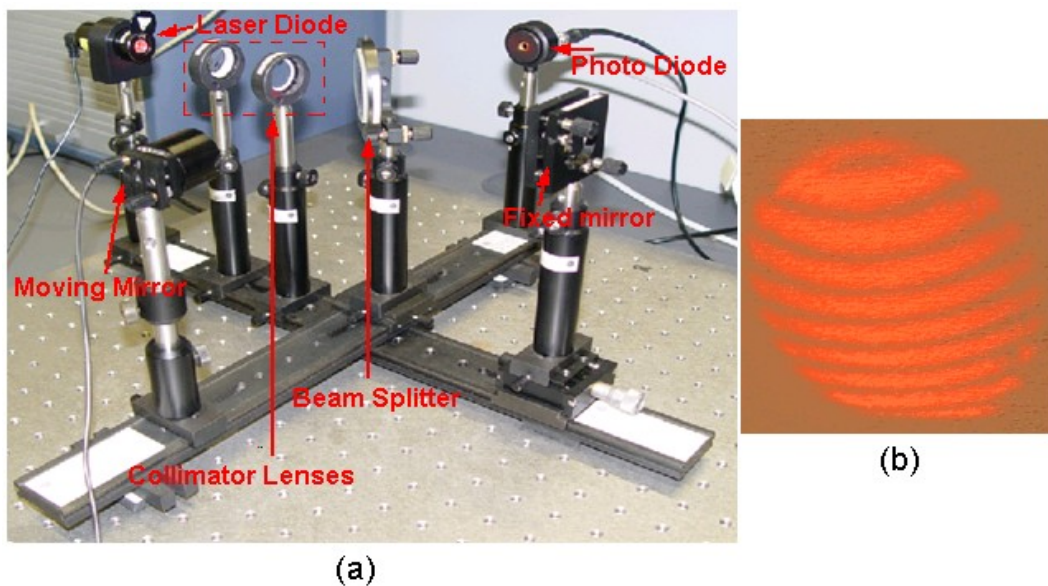
Figure 3 - (a) Setup of Michelson Interferometer in the laboratory; (b) Close-up of the interference fringes formed on the photodiode by tilting a mirror.

Now suppose one mirror is moved by half of a wavelength. This will add an extra full wavelength to the round-trip path. That results in a shift of fringe patterns, moving dark fringes to where light ones were and vice-versa. This is how one can use an interferometer for precise distance or velocity measurement.

2.2.2 The Doppler effect

When the source emitting a wave and a receiver detecting the wave are in motion relative to each other, there is a change or apparent change in the frequency of the wave. This is known as the Doppler effect. One common example that demonstrates the Doppler effect is a car passing a stationary observer with its horn sounding. The horn's pitch appears to be higher as the car approaches and lower as it moves away.

It also describes the situation where a light source and receiver are stationary relative to each other, and the wave is reflected off a moving object. This is the case for Laser Doppler Velocimetry.

2.2.2.1 Moving receiver with stationary source

In Figure 4 a detector is moving at the speed, u, towards a stationary source emitting waves of wavelength, λ, and frequency, v. c is the wave front velocity, and θ is the angle between the direction of motion and a line passing through both the source and detector. If both, the source and the detector, were stationary the frequency detected by the detector would be v. However, since the detector is moving into the wave fronts, the rate of interception is greater and thus the detected frequency, v', is greater than v (Halliday et al. 2003).

The new velocity is
$$c' = c + u\cos\theta.$$
(2.4)

The frequency perceived by the receiver is therefore
$$v' = \frac{c + u\cos\theta}{\lambda}$$

or
$$v' = v(1 + \frac{u}{c}\cos\theta).$$
(2.5)
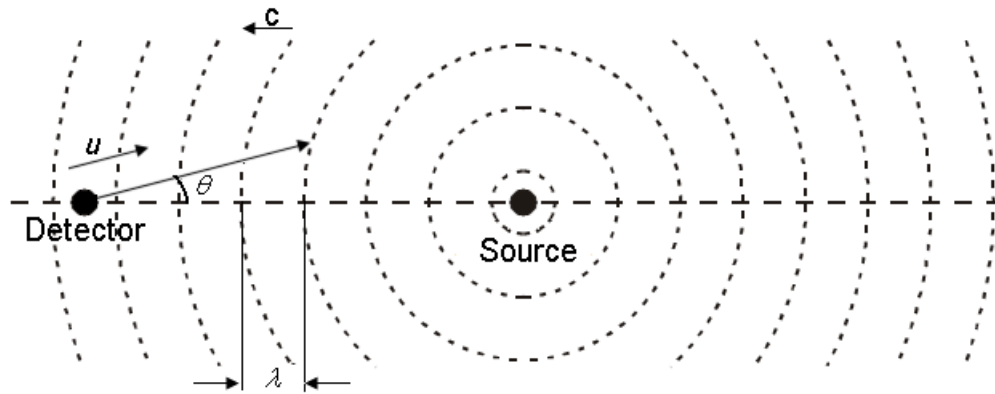
Figure 4 - Doppler shifts with a moving detector.

The increase in the frequency (beat frequency) perceived by the receiver is thus given by

$$\Delta v = \frac{u \cos \theta}{\lambda}.$$ (2.6)

2.2.2.2 Moving source with stationary receiver

Now let us consider the case of the source moving towards a stationary detector. The motion of the source reduces the wavelength of the emitted waves because by the time a new wave front is emitted, the source has moved closer. As a result, the receiver perceives a shorter wavelength and hence higher frequency.
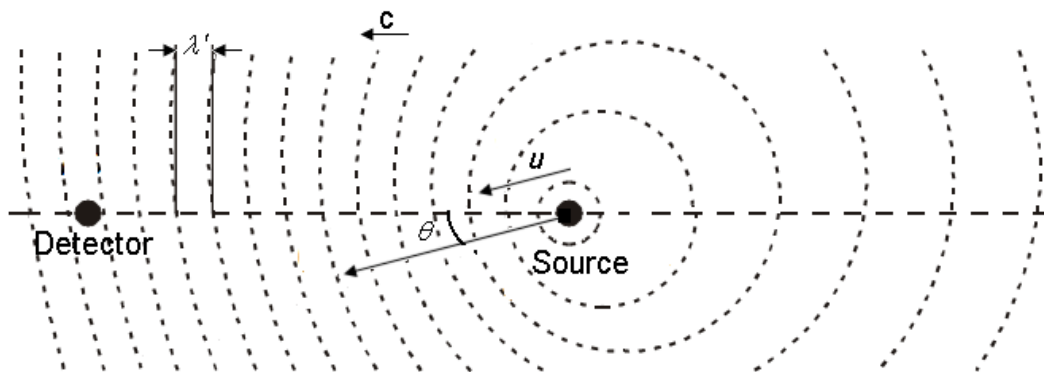
Figure 5 - Doppler shifts with a moving source.

$$v' = \frac{c}{\lambda'}$$

or

$$v' = \frac{c}{\dfrac{c}{v} - \dfrac{u \cos \theta}{v}}$$

$$v' = \frac{v}{1 - \frac{u}{c}\cos\theta}. \tag{2.7}$$

These derivations do not hold for light or other electromagnetic waves in vacuum as the speed of light is constant irrespective of the source and receiver's relative motion. We have to treat the problem using principles of the special theory of relativity.

2.2.2.3 Doppler shifting by back-scattering

For self-mixing interferometry, we only consider the case of back-scattering. The following derivation is based on Drain (1980). Figure 6 illustrates a beam incident at an angle, θ, onto a mirror and is scattered back through the same path.

When the mirror moves perpendicular to its own plane, there is a Doppler shift. Let us assume the velocity of the mirror is in direction, u. The position of the mirror at t and δt is shown in Figure 6, and the distance between two positions is $u\delta t$.
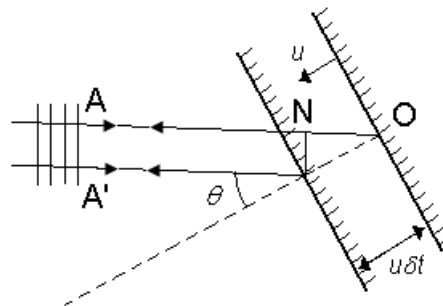
Figure 6 - Illustration of Doppler shifting by back scattering (Adapted from (Drain 1980)).

During time, δt, the optical path length between incident wave front and the back-scattered wave front decreases by

$$\delta l = NO + ON = 2u\delta t\cos\theta.$$

Hence, by using $c = v\lambda$, the Doppler shift is

$$\Delta v = \frac{1}{\lambda}\frac{dl}{dt} = \frac{2u\cos\theta}{\lambda}. \tag{2.8}$$

This is the basis of our velocimeter sensor.

2.3   Semiconductor Laser Diode Fundamentals

Semiconductor lasers have proven to be most versatile and widespread because of their convenience, efficiency and compatibility with the modern electronics. Pumping and modulation by electric current injection is easy in laser diodes. However the spectral linewidth of semiconductor laser is typically larger than that of other lasers. In general they are simply a pn-junction combined with an optical resonator formed by cleaving.

The laser diode (LD) is similar to the light emitting diode (LED). In both devices, the source of energy is an electric current injected into a pn-junction. However, the light emitted from LEDs is generated by spontaneous emission, whereas the light emitted from an LD arises from stimulated emission.

The first semiconductor lasers were similar to semiconductor diodes consisting of p-type and n-type material. These devices were called homostructure or homojunction lasers simply because those two layers were made from the same compound semiconductor. The diode lasers based on this structures required cooling even to operate in pulsed mode. The laser diodes were improved by replacing homojunction with a heterojunction between layers of semiconductors with different composition (Hecht 2008).
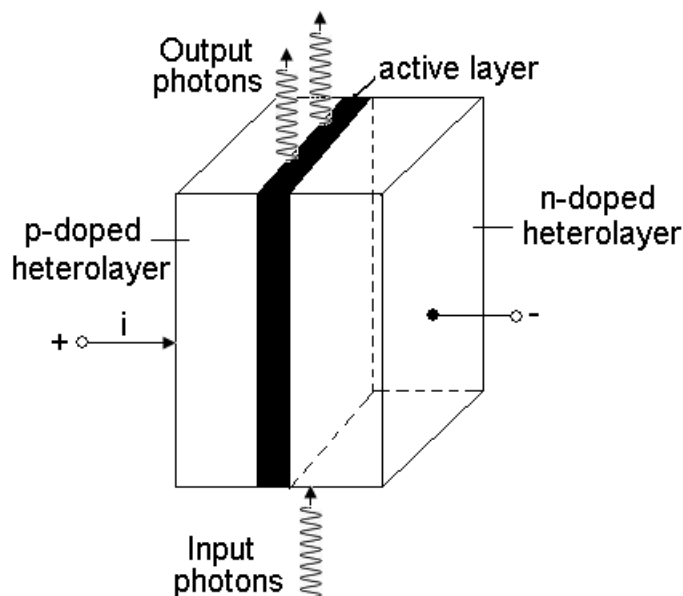
Figure 7 - Basic structure of a double heterostructure semiconductor laser showing charge carriers travelling perpendicular whereas photons travelling in the plane of the junction (Saleh and Teich 1991).
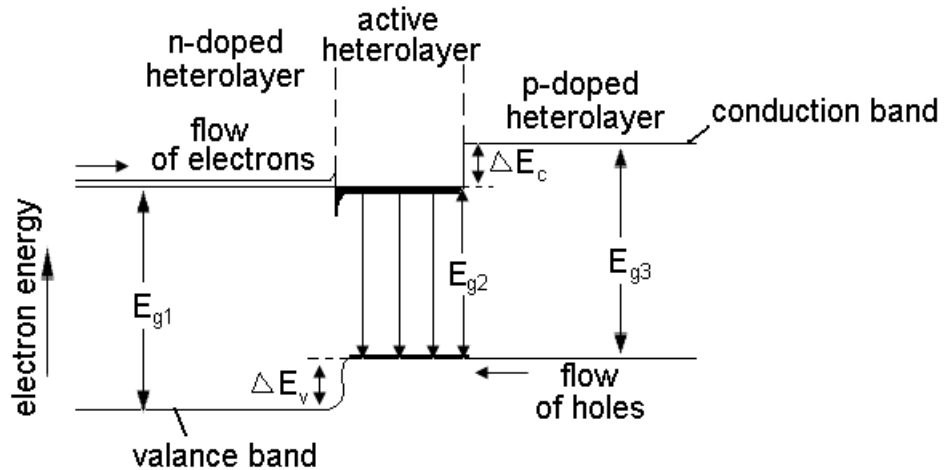
Figure 8 - Band diagram of a double heterostructure laser diode under forward current excitation (Petermann 1991).

The carrier density required for laser operation is rather high which was further improved effectively by the use of double heterojunction. The active layer (in which carriers recombine) is embedded between heterolayers. Let E_{g1}, E_{g2} and E_{g3} denote the energy gaps of the n-doped heterolayer, the active heterolayer and the p-doped heterolayer, respectively. When the current is applied, electrons diffuse from the n-doped heterolayer and holes diffuse from p-doped heterolayer into the active layer. At the junction, electrons have to overcome the energy gap ΔE_c to pass into the p-doped heterolayer and holes have to overcome the energy gap ΔE_v to pass into the n-doped heterolayer. The injected carriers may therefore only recombine in the active layer since there the electrons in the conduction band find holes in the valance band with which they can recombine. As a result of the recombination of electrons and holes, photons are emitted with the frequency $v = E_{g2}/h$, where h is the Planck's constant. At each end of the active layer, an optical cavity is built by cleaving the semiconductor crystal. This produces two parallel facets or mirrors allowing for resonant mode selection and energy storage. The length of a typical laser diode is 100 µm to 500 µm. Reflection occurs at the facets because of the mismatch between the index of refraction of the semiconductor ($\mu \approx 3.6$) and the surrounding air. About 30 to 40% of the incident optical power is reflected by each facet which is sufficient for laser operation. One facet is exposed and becomes the output aperture of the laser diode (Petermann 1991).

The following derivation is based on Petermann's field approach (Petermann 1991). In order to derive the static conditions necessary for lasing to occur, the transverse electric field amplitudes, $E(z)$, will be considered instead of optical power $P(z) \sim |E(z)|^2$.
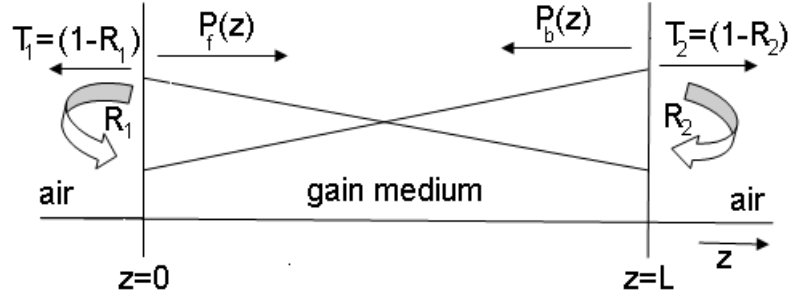
Figure 9 - A schematic drawing of a power flow in forward and backward direction in a laser diode cavity.

In Figure 9, the laser diode's facets are semiconductor-air interfaces and are located at $z = 0$ and $z = L$ with reflectivities R_1 and R_2 respectively. The forward travelling complex electric field is

$$E_f(z) = E_{f0} \exp(-j\beta z + \frac{1}{2}(g - \alpha_s)z), \tag{2.9}$$

where g is the gain due to stimulated emission, α_s is the optical loss in the laser cavity, for example scattering loss, and β is the phase constant of the optical wave.

Similarly the backward travelling wave amplitude is

$$E_b(z) = E_{b0} \exp(-j\beta(L - z) + \frac{1}{2}(g - \alpha_s)(L - z)). \tag{2.10}$$

E_f and E_b are related to each other by the reflection coefficients, r_1 and r_2, at the laser facets with $R_1 = r_1 r_1^* = |r_1|^2$, $R_2 = r_2 r_2^* = |r_2|^2$ according to

$$E_f(z = 0) = E_{f0} = r_1 E_b(z = 0);$$

$$E_b(z = L) = E_{b0} = r_2 E_f(z = L).$$

Multiplying equation (2.9) and equation (2.10) gives

$$E_{f0}E_{b0} = |r_1||r_2|E_{f0}E_{b0} \exp(-2j\beta L + (g - \alpha_s)L).$$

This yields the condition for stationary laser oscillation:

$$|r_1||r_2|\exp(-2j\beta L + (g - \alpha_s)L) = 1 \qquad (2.11)$$

or

$$|r_1||r_2|\exp(-2j\beta L)\exp((g - \alpha_s)L) = 1$$

r_1 and r_2 can also be expressed as , $r_1 = |r_1||e^{-j\pi}$, $r_2 = |r_2|e^{-j\pi}$. $-\pi$ in the exponent of the complex reflection coefficient accounts for the phase reversal at the laser diode facets. The absolute value of equation (2.11) gives a condition for the required gain, g , while the phase of equation (2.11) gives a condition for the phase constant, β . If r_1 and r_2 are real and the required gain, g , is denoted as g_{th} , then

$$g_{th} = \alpha_s + \frac{1}{2L}\ln(\frac{1}{R_1 R_2}) \qquad (2.12)$$

and

$$\exp(-2j\beta L) = 1.$$

This implies

$$\beta L = m\pi, \quad m = 0,1,2... \qquad (2.13)$$

The actual gain, g , will usually be slightly smaller than the threshold gain, g_{th} , in equation (2.12) as the contribution of spontaneous emission has not been considered. Let us introduce an effective refractive index, μ_e , for the lasing mode as,

$$\mu_e = c\frac{\beta}{\omega_0} = c\frac{\beta}{2\pi v_0} ,$$

where c is the velocity of light, v_0 is the optical frequency, $\omega_0 = 2\pi v_0$ is the angular frequency. The possible emission frequency can be written as

$$v_0 = \frac{mc}{2L\mu_e}. \qquad (2.14)$$

Effective group refractive index can be given as

$$\bar{\mu}_e = \mu_e + v_{th}\frac{d\mu_e}{dv_0}. \qquad (2.15)$$

The longitudinal mode spacing (spacing between adjacent emission frequencies) is expressed as

$$\delta v_0 = \frac{c}{2L\bar{\mu}_e}. \qquad (2.16)$$

The group velocity of the optical wave is

$$u_g = \frac{c}{\bar{\mu}_e}.$$

Spacing between adjacent emission frequencies corresponds to the inverse round tip delay

$$\tau_L = \frac{2L\bar{\mu}_e}{c} = \frac{1}{\delta v_0}. \tag{2.17}$$

Typically $\mu_e \approx 3.5$ and $\bar{\mu}_e \approx 3.5$ to 5. This yields $\tau_L \approx 10$ ps for $L = 300$ to 400 µm. Gain and refractive index depend on carrier density, n. Let us introduce n_{th} at the lasing threshold, given by

$$g(n_{th}) = g_{th}$$

The effective refractive index, μ_e, depends on the optical frequency and the carrier density. The resonance frequency, v_{th}, for $n = n_{th}$ according to equation (2.14) is

$$v_{th} = \frac{mc}{2L\mu_e(v_{th}, n_{th})} = \frac{mc}{2L\mu_{eo}} \tag{2.18}$$

where $\mu_{eo} = \mu_e(v_{th}, n_{th})$. If the carrier density deviates slightly from n_{th}, μ_e may be expanded in terms of v_{th} and n_{th} yielding

$$\mu_e = \mu_{eo} + \frac{\partial \mu_e}{\partial v_0}(v_0 - v_{th}) + \frac{\partial \mu_e}{\partial n}(n - n_{th}). \tag{2.19}$$

From equation (2.14),(2.18) and (2.19),

$$(v_0 - v_{th}) = -\frac{v_{th}}{\bar{\mu}_e}\frac{\partial \mu_e}{\partial n}(n - n_{th}) \tag{2.20}$$

Equation (2.20) implies that the lasing frequency is modulated by the laser diode's injection current.

2.4   Theory of self-mixing interferometry

The three mirror model and the analysis by the Lang and Kobayashi equations are two popular models to explain self-mixing interferometry. The first is simple to understand and work with whereas the later is more complete and accounts for most of the physical parameters (Bosch et al. 2001).

2.4.1 Three-mirror model

The self-mixing effect in a laser occurs when some part of light emitted by the laser re-enters the laser cavity. It can be modelled as two mirror for the Fabry-Perot structure of the laser and the external mirror for the object reflecting the laser back. The three-mirror model can be used to explain self-mixing in lasers other than diode lasers as well however in this thesis we will focus on diode lasers. The schematic diagram of the self-mixing effect in a semiconductor laser is presented in the Figure 10. The following section attempts to explain the three mirror model based on the work by Petermann (1991) and Koelink et al.(1992b).

As shown in Figure 10, the mirror facets, M_1 and M_2, are positioned at $z = 0$ and $z = L$ with an amplitude reflection coefficient, r_1, r_{2s}, respectively. The external target (M_{ext}) is positioned at $z = L + L_{ext}$ with an amplitude reflection coefficient, r_{2ext}.
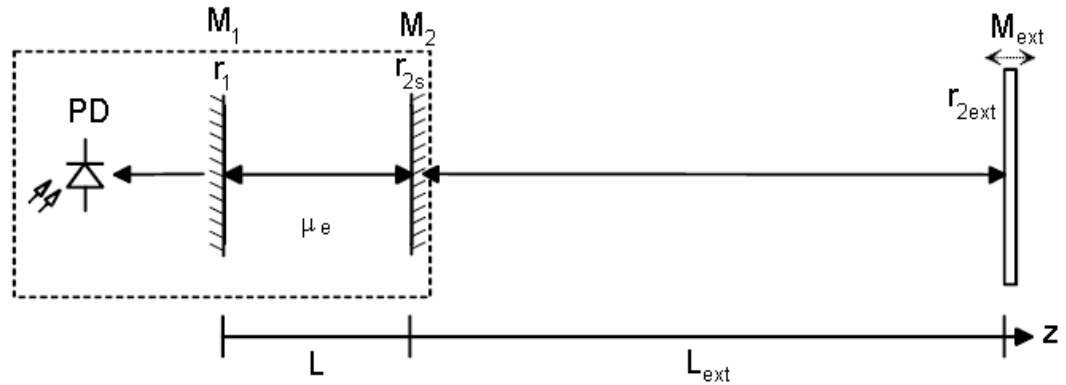
Figure 10 - Schematic of three mirror model for self-mixing effect in laser diode.

We replace the mirror at $z = L$ and the mirror at $z = L + L_{ext}$ by an effective mirror at $z = L$. The reflection coefficient, r_c, for the new compound cavity is given by

$$r_c(v) = |r_{2s}| + (1 - R_{2s}) r_{2ext} \exp(-i2\pi v_c \tau_{ext}) \tag{2.21}$$

where v_c is the optical frequency of the compound cavity, $\tau_{ext} = 2L_{ext}/c$ is the round trip delay time, and c is the speed of light.

The term $(1 - R_{2s})$ in equation (2.21) is the fraction of light that passes through the laser diode facet at $z = L$ and is consequently reflected by the external reflector with amplitude reflection coefficient of r_{2ext}. The exponential term adds

$2\pi v_c \tau_{ext}$ (i.e. $\omega_c \tau_{ext}$) of phase change for one round trip. For $|r_{2ext}| << |r_{2s}|$, the effects of multiple reflections are negligible. Substituting $R_{2s} = |r_{2s}|^2$ in equation (2.21) we get

$$r_c(v) = |r_{2s}| + \left(1 - |r_{2s}|^2\right) r_{2ext} \exp\left(-j2\pi v_c \tau_{ext}\right) . \tag{2.22}$$

$r_c(v)$ can be expressed in polar form as

$$r_c(v) = |r_c| \exp(-j\phi_r) \tag{2.23}$$

where ϕ_r and $|r_c|$ will be determined. To achieve successful operation of the laser, both the phase and amplitude conditions must be fulfilled. If we replace $|r_2|$ in equation (2.11) by the effective reflection coefficient of the compound cavity and threshold gain $g = g_c$,

$$|r_1||r_c| \exp j(-2\beta L - \phi_r) \exp((g_c - \alpha_s)L) = 1$$

The phase condition states that the round trip phase of the compound cavity must be an integer multiple of 2π.

$$2\beta L + \phi_r = 2\pi m . \tag{2.24}$$

By using μ_e, equation (2.24) can be re-written as:

$$4\pi \mu_e v_c L / c + \phi_r = 2\pi m . \tag{2.25}$$

Without feedback, $\phi_r = 0$, the required threshold gain for the compound cavity laser must satisfy the amplitude condition

$$|r_1||r_c| \exp\left[(g_c - \alpha_s)L\right] = 1 . \tag{2.26}$$

r_{2s}, r_{2ext} may be considered as real and positive. Therefore using relation $e^{-j\theta} = \cos\theta - j\sin\theta$ in equation (2.21) yields

$$r_c(v) = |r_{2s}| \left[(1 + \kappa_{ext} \cos(2\pi v_c \tau_{ext})) - j(\kappa_{ext} \sin(2\pi v_c \tau_{ext})) \right] \tag{2.27}$$

where

$$\kappa_{ext} = \frac{r_{2ext}}{r_{2s}}(1 - R_{2s}) = \frac{r_{2ext}}{r_{2s}}(1 - |r_{2s}|^2), \ (0 < \kappa_{ext} < 1) . \tag{2.28}$$

κ_{ext} indicates the amount of light coupled back into the laser diode.

From equation (2.27):

$$r_c = |r_{2s}| \sqrt{(1 + \kappa_{ext} \cos(2\pi v_c \tau_{ext}))^2 + (\kappa_{ext} \sin(2\pi v_c \tau_{ext}))^2}$$

or

$$r_c = |r_{2s}|[1 + 2\kappa_{ext}\cos 2\pi v_c \tau_{ext} + \kappa_{ext}^2]^{\frac{1}{2}}.$$ (2.29)

For the weak feedback, $\kappa_{ext} \ll 1$

$$r_c \approx |r_{2s}|(1 + \kappa_{ext}\cos 2\pi v_c \tau_{ext}).$$ (2.30)

Here we have used the approximation

$$(1 + 2x)^{1/2} \approx (1 + x) \quad \text{for } x \ll 1$$

We can write the phase of $r_c(v)$ as,

$$\phi_r = \tan^{-1}\frac{B}{A} = \tan^{-1}\left(\frac{\kappa_{ext}\sin(2\pi v_c \tau_{ext})}{1 + \kappa_{ext}\cos(2\pi v_c \tau_{ext})}\right) = \tan^{-1}\left(\frac{\sin(2\pi v_c \tau_{ext})}{\dfrac{1}{\kappa_{ext}} + \kappa_{ext}\cos(2\pi v_c \tau_{ext})}\right)$$ (2.31)

We are dealing with the weak optical feedback, $\kappa_{ext} \ll 1$. That makes the denominator of equation (2.31) large. Using approximation, $(\tan^{-1}(x) = x - \dfrac{x^3}{3} + \dfrac{x^5}{5}...)$ equation (2.31) can be expressed as,

$$\phi_r = \kappa_{ext}\sin(2\pi v_c \tau_{ext}).$$ (2.32)

Thus the terms ϕ_r and $|r_c|$ of the equation (2.23) are completely defined. In equation (2.26), the amplitude condition of the compound laser cavity is defined. Without feedback, equation (2.26) can be rewritten as,

$$|r_1||r_{2s}|\exp\left[(g_{th} - \alpha_s)L\right] = 1.$$ (2.33)

From equation (2.26),

$$\exp[(g_c - \alpha_s)L] = \left(\frac{1}{|r_1||r_c|}\right)$$

or

$$g_c = \alpha_s + \frac{1}{L}\ln\left(\frac{1}{|r_1||r_c|}\right) \; .$$

Similarly from equation (2.33),

$$g_{th} = \alpha_s + \frac{1}{L}\ln\left(\frac{1}{|r_1||r_{2s}|}\right)$$

$$\text{or, } g_c - g_{th} = \frac{1}{L}\ln\left(\frac{1}{|r_1||r_c|}\right) - \frac{1}{L}\ln\left(\frac{1}{|r_1||r_{2s}|}\right)$$

Substituting value of $|r_c|$ from equation (2.30),

$$g_c - g_{th} = \frac{1}{L} \ln \left(\frac{|r_1||r_{2s}|}{|r_1||r_{2s}|\left(1 + \kappa_{ext} \cos 2\pi \nu_c \tau_{ext}\right)} \right)$$

or

$$g_c - g_{th} = -\frac{1}{L} \ln \left(1 + \kappa_{ext} \cos 2\pi \nu_c \tau_{ext}\right)$$

Using Maclaurin series ($\ln(1 + x) = x - \frac{1}{2}x^2 + \frac{1}{3}x^3 - \frac{1}{4}x^4 + ...$ *for* $-1 < x \leq 1$),

For $\kappa_{ext} \ll 1$,

$$g_c - g_{th} = -\frac{\kappa_{ext}}{L} \cos 2\pi \nu_c \tau_{ext} \tag{2.34}$$

The required gain is either decreased or increased depending on the phase of the externally reflected light. The maximum threshold gain reduction occurs if ϕ_{ext} is an integer multiple of 2π (i.e. in-phase feedback). Without feedback ($\phi_r = 0$), emission frequency, $\nu_c = \nu_{th}$, is obtained. Due to feedback, the emission frequency may change as well as the threshold gain, and thus the refractive index yielding a change of

$$\Delta\left(\mu_e \nu_c\right) = \nu_{th}\Delta\mu_e + \mu_e \Delta \nu_c$$

or

$$\Delta\left(\mu_e \nu_c\right) = \nu_{th}\Delta\mu_e + \left(\nu_c - \nu_{th}\right)\mu_e .$$

Since, $\Delta\phi_L$ corresponds to a change in the round trip phase compared to $2\pi m$. From equation (2.25),

$$\Delta\phi_L = \Delta\left(\mu_e \nu_c\right) 4\pi \frac{L}{c} + \phi_r$$

or

$$\Delta\phi_L = \left(4\pi \frac{L}{c}\right)\left[\nu_{th}\Delta\mu_e + \mu_e\left(\nu_c - \nu_{th}\right)\right] + \phi_r . \tag{2.35}$$

Since the round trip phase must equal $2\pi m$ also for the compound cavity, the emission frequencies are obtained from equation (2.35) for $\Delta\phi_L = 0$ (or multiples of 2π). According to equation (2.19) the change in the effective index may be expressed as:

$$\Delta\mu_e = \frac{\partial\mu_e}{\partial n}\left(n - n_{th}\right) + \frac{\partial\mu_e}{\partial\nu_c}\left(\nu_c - \nu_{th}\right) \tag{2.36}$$

where the carrier density, n_{th}, corresponds to the threshold carrier density without feedback. Using equation (2.35) and equation (2.36) gives:

$$\Delta\phi_L = \frac{4\pi L}{c}\left[v_{th}\left\{\frac{\partial\mu_e}{\partial n}\left(n-n_{th}\right)+\frac{\partial\mu_e}{\partial v}\left(v_c-v_{th}\right)\right\}+\mu_e\left(v_c-v_{th}\right)\right]+\phi_r$$

or

$$\Delta\phi_L = \frac{4\pi L}{c}\left[v_{th}\frac{\partial\mu_e}{\partial n}\left(n-n_{th}\right)+\left(v_{th}\frac{\partial\mu_e}{\partial v_c}+\mu_e\right)\left(v_c-v_{th}\right)\right]+\phi_r$$

Using the effective group refractive index from equation (2.15) yields

$$\Delta\phi_L = \frac{4\pi L}{c}\left[v_{th}\frac{\partial\mu_e}{\partial n}\left(n-n_{th}\right)+\bar{\mu}_e\left(v_c-v_{th}\right)\right]+\phi_r \ . \tag{2.37}$$

The variation of the refractive index with varying carrier density is linked to gain variations via the linewidth enhancement factor, α .

$$\frac{\partial\mu_e}{\partial n} = \alpha\frac{\partial\mu_e''}{\partial n} = -\alpha\frac{\partial g}{\partial n}\frac{c}{4\pi v_{th}} \tag{2.38}$$

α has a typical value of 3 to 7. $\alpha = \dfrac{\partial\mu'}{\partial\mu''}$, where μ' stands for real part and μ'' stands for imaginary part of the complex refractive index, $\mu=\mu'+j\mu''$.

Substituting $\dfrac{\partial g}{\partial n} \approx \dfrac{\left(g-g_{th}\right)}{\left(n-n_{th}\right)}$ in equation (2.38),

$$\frac{\partial\mu_e}{\partial n}\left(n-n_{th}\right) = -\frac{\alpha c}{4\pi v_{th}}\left(g-g_{th}\right) \ . \tag{2.39}$$

Since g must satisfy the amplitude condition, with $g = g_c$ equation (2.37) becomes

$$\Delta\phi_L = -\alpha\left(g_c-g_{th}\right)L + \frac{4\pi\bar{\mu}_e L}{c}\left(v_c-v_{th}\right)+\phi_r \ . \tag{2.40}$$

Substituting equation (2.32) and equation (2.34) in equation (2.40) yields

$$\Delta\phi_L = \frac{4\pi\bar{\mu}_e L}{c}\left(v_c-v_{th}\right)+\kappa_{ext}\left[\sin\left(2\pi v_c\tau_{ext}\right)+\alpha\cos\left(2\pi v_c\tau_{ext}\right)\right] \ . \tag{2.41}$$

If we combine equation (2.17) with equation (2.41) we get

$$\Delta\phi_L = 2\pi\tau_L\left(v_c-v_{th}\right)+\kappa_{ext}\left(\sqrt{1+\alpha^2}\right)\left[\frac{\sin\left(2\pi v_c\tau_{ext}\right)}{\sqrt{1+\alpha^2}}+\frac{\alpha}{\sqrt{1+\alpha^2}}\cos\left(2\pi v_c\tau_{ext}\right)\right] . \tag{2.42}$$

Substituting

$$\cos(\tan^{-1}\alpha) = \frac{1}{\sqrt{\alpha^2+1}}, \tag{2.43}$$

$$\sin(\tan^{-1}\alpha) = \frac{\alpha}{\sqrt{\alpha^2+1}} \tag{2.44}$$

leads to

$$\Delta\phi_L = 2\pi\tau_L\left(v_c - v_{th}\right) + \kappa_{ext}\left(\sqrt{1+\alpha^2}\right)\left[\sin\left(2\pi v_c\tau_{ext}\right)\cos(\tan^{-1}\alpha) + \cos\left(2\pi v_c\tau_{ext}\right)\sin(\tan^{-1}\alpha)\right].$$

This can be simplified as:

$$\Delta\phi_L = 2\pi\tau_L\left(v_c - v_{th}\right) + \kappa_{ext}\left(\sqrt{1+\alpha^2}\right)\sin\left(2\pi v_c\tau_{ext} + \tan^{-1}\alpha\right). \qquad (2.45)$$

In Figure 11, $\Delta\phi_L = 0$ characterises the point where the phase condition is satisfied. Without feedback $\Delta\phi_L$ varies linearly with v_c, yielding its zero at $v_c = v_{th}$. As the optical feedback in the laser diode cavity starts increasing, relationship between $\Delta\phi_L$ and v_c starts to become non-linear. For higher feedback level, the $\Delta\phi_L$ versus v_c characteristic may undergo strong oscillations yielding multiple zeroes for $\Delta\phi_L$. In that case several external cavity modes around the emission frequency, v_{th}, of the solitary laser may eventually oscillate. Based on these behaviours, feedback parameter, C, can be defined as (Acket et al. 1984):

$$C = \frac{\kappa\tau_{ext}\sqrt{1+\alpha^2}}{\tau_L} \qquad (2.46)$$

where κ is the feedback parameter which is given, for a Fabry-Perot laser, by $\kappa = \varepsilon\kappa_{ext}$ and ε is the coupling efficiency which takes into account the mode mismatch and the finite coherence length.
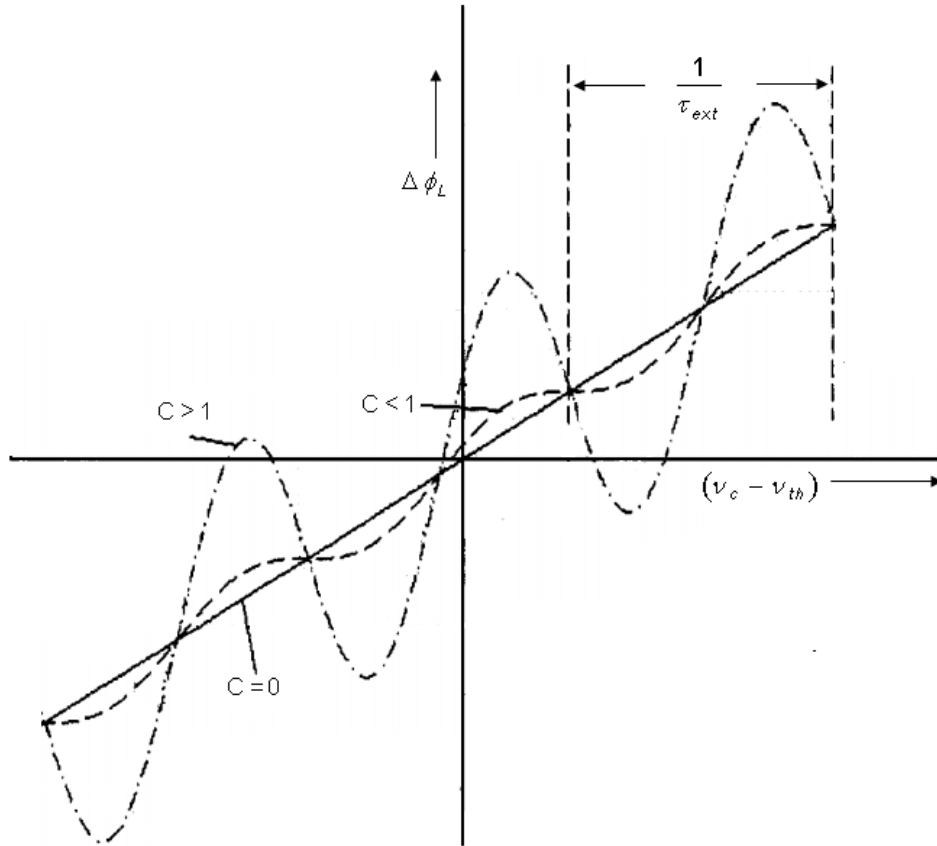
Figure 11 - Plot of round trip phase change vs optical frequency for different values of the feedback parameter (C) (Petermann 1991).

2.4.2 Analysis by the Lang and Kobayashi equations

The following section explains the analysis of laser diodes with optical feedback using Lang and Kobayashi equations (Donati et al. 1995; Donati 2004). Let us again consider Figure 10, where the laser diode is modelled by mirrors M_1 and M_2. A fraction of the optical beam from the laser diode is backscattered into the laser diode cavity by the external target. The photodiode at the rear facet of the laser diode monitors the power, P, of the laser diode by means of photogenerated current, $I = \sigma P$, where σ =spectral responsivity.

According to the Lang and Kobayashi's equations (Lang and Kobayashi 1980), the dynamics of a laser diode in the presence of feedback can be written as:

$$\frac{d}{dt}E_0(t) = \frac{1}{2}\left[G_N(N(t)-N_0) - \frac{1}{\tau_P}\right]E_0(t) + \frac{\kappa}{\tau_L}E_0(t-\tau)\cos\left[\omega_0\tau + \phi(t) - \phi(t-\tau)\right] \quad (2.47)$$

$$\frac{d}{dt}\phi(t) = \frac{1}{2}\alpha G_N[N(t) - N_T] - \frac{\kappa}{\tau_L}\frac{E_0(t-\tau)}{E_0(t)}\sin[\omega_0\tau + \phi(t) - \phi(t-\tau)]$$ (2.48)

$$\frac{d}{dt}N(t) = R_P - \frac{N(t)}{\tau_s} - G_N[N(t) - N_0]E_0^2(t)$$ (2.49)

where,

$E(t)$ laser electric field, expressed as $E(t) = E_0(t)\exp\left[j\left(\omega_0 t + \phi(t)\right)\right]$ with $E_0(t)$ normalized so that $E_0^2(t)$ is the photon density in the laser cavity

G_N modal gain coefficient (typical value $G_N = 8.10^{-13}\,\mathrm{m^3 s^{-1}}$)

$N(t)$ average carrier (electron-hole pairs) density in the active layer

N_0 carrier density at transparency (typical value $N_0 = 1.4\times 10^{24}\,\mathrm{m^{-3}}$)

N_T carrier density at threshold for the unperturbed laser (typical value $N_T = 2.3\times 10^{24}\,\mathrm{m^{-3}}$)

τ_P photon lifetime (typical value $\tau_P = 1.6$ ps) and $1/\tau_P = G_N(N_T - N_0)$

τ_L diode cavity round trip time (for e.g.. $\tau_L = 8.3$ ps for the mode spacing 120.41 GHz)

τ_S carrier lifetime (typical value $\tau_S = 2$ ns)

R_P electric pumping term, which is given by $R_P = \frac{J\eta}{ed}$, with J injected current density, η conversion efficiency, e electron charge, d active layer thickness

Stationary solutions of the equations (2.47) to (2.49) can be found by substituting

$$E_0(t) = E_0(t - \tau_{ext}) = E_F = \text{constant}$$

$$N(t) = N_F = \text{constant}\ \left(\text{for the stationary solutions}\right).$$

The instantaneous optical frequency is given by

$$\omega(t) = \omega_0 + \left[\frac{d\phi(t)}{dt}\right].$$

The contribution $\dfrac{d\phi(t)}{dt}$ represents a frequency deviation, and we can thus take $\phi(t) = (\omega_c - \omega_0)t$ where $\omega_c = \omega_c(\tau_{ext})$ is the angular frequency of the laser with external feedback. Substituting the above assumptions, from equation (2.47),

$$0 = \frac{1}{2}\left[G_N(N_F - N_0) - \frac{1}{\tau_P}\right]E_F + \frac{\kappa}{\tau_L}E_F\cos(\omega_c\tau_{ext})$$

where,

$$\omega_0\tau_{ext} + \phi(t) - \phi(t - \tau_{ext})$$
$$= \omega_0\tau_{ext} + (\omega_c - \omega_0)t - (\omega_c - \omega_0)(t - \tau_{ext})$$
$$= \omega_0\tau_{ext} + \omega_c t - \omega_0 t - \omega_c t + \omega_0 t + \omega_c\tau_{ext} - \omega_0\tau_{ext}$$
$$= \omega_c\tau_{ext}.$$

$$0 = \left[\frac{1}{2}(N_F - N_T)G_N + \frac{\kappa}{\tau_L}\cos(\omega_c\tau_{ext})\right]E_F$$

or

$$\frac{1}{2}G_N(N_F - N_T) = -\frac{\kappa}{\tau_L}\cos(\omega_c\tau_{ext}). \tag{2.50}$$

We have,

$$\omega(t) - \omega_0 = \frac{d\phi(t)}{dt}$$

$$\omega(t) - \omega_0 = \frac{d(\omega_c - \omega_0)t}{dt}$$

$$\omega(t) - \omega_0 = \omega_c - \omega_0. \tag{2.51}$$

From equation (2.48) and (2.51),

$$\omega_c - \omega_0 = \frac{1}{2}\alpha G_N(N_F - N_T) - \frac{\kappa}{\tau_L}\sin(\omega_c\tau_{ext}). \tag{2.52}$$

From equation (2.49),

$$0 = R_P - \frac{N_F}{\tau_S} - G_N[N_F - N_0]E_F^2. \tag{2.53}$$

Substituting equation (2.50) in equation (2.52),

$$\omega_c - \omega_0 = \frac{-\alpha\kappa}{\tau_L}\cos(\omega_c\tau_{ext}) - \frac{\kappa}{\tau_L}\sin(\omega_c\tau_{ext}) \tag{2.54}$$

$$\omega_0 = \omega_c + \frac{\kappa}{\tau_L}(\alpha\cos\omega_c\tau_{ext} + \sin\omega_c\tau_{ext}). \tag{2.55}$$

This corresponds to the well known round trip phase change condition $\Delta\phi = 0$. For weak and moderate feedback, allowed oscillation frequencies ω_c are solutions of equation (2.55). Re-writing equation (2.46):

$$C = \frac{\kappa\tau_{ext}\sqrt{1 + \alpha^2}}{\tau_L}.$$

From equation (2.55) and (2.46),

$$\omega_0 \tau_{ext} = \omega_c \tau_{ext} + \frac{C}{\sqrt{1+\alpha^2}} \left(\alpha \cos \omega_c \tau_{ext} + \sin \omega_c \tau_{ext} \right) \tag{2.56}$$

or

$$\omega_0 \tau_{ext} = \omega_c \tau_{ext} + C \sin \left(\omega_c \tau_{ext} + \arctan \alpha \right). \tag{2.57}$$

Equation (2.57) has just one solution for ω_c when $C<1$ and multiple solutions when $C>1$. Thus we can take $C=1$ as the boundary between the weak and moderate feedback regime.

From equation (2.50),

$$N_F = N_T - \frac{2\kappa}{G_N \tau_L} \cos \left(\omega_c \tau_{ext} \right). \tag{2.58}$$

Using equation (2.58) in equation (2.53)

$$E_F^2 = \frac{R_P - \left[\dfrac{N_F}{\tau_S} \right]}{G_N (N_F - N_0)}$$

$$= \frac{R_P \tau_S - N_T + \dfrac{2\kappa}{G_N \tau_L} \cos \omega_c \tau_{ext}}{1 - \dfrac{2\kappa \tau_P}{\tau_L} \cos \omega_c \tau_{ext}} \left(\frac{\tau_P}{\tau_S} \right). \tag{2.59}$$

For practical case we can approximate $\kappa < 0.01$. Approximating equation (2.59), we get

$$E_F^2 = \frac{\tau_P}{\tau_S} \left(R_P \tau_S - N_T + \frac{2\kappa}{G_N \tau_L} \cos \omega_c \tau_{ext} \right) \left(1 + \frac{2\kappa \tau_P}{\tau_L} \cos \omega_c \tau_{ext} \right). \tag{2.60}$$

Let E_{NF} be the stationary electric field. In case of no feedback

$$E_{NF}^2 = \tau_P (R_P - (N_T / \tau_S)). \tag{2.61}$$

Neglecting second order contributions from equation (2.60), the output power variation ΔP due to feedback with respect to the unperturbed laser is given by

$$\Delta P \propto E_F^2 - E_{NF}^2 = \tau_P (R_P - (N_0 / \tau_S)) \frac{2\kappa \tau_P}{\tau_L} \cos \omega_c \tau_{ext}. \tag{2.62}$$

Assuming κ does not depend on the external cavity

$$\Delta P = \Delta P_{max} \cos \omega_c \tau_{ext}. \tag{2.63}$$

2.4.3 C parameter

As earlier stated in equation (2.46) feedback parameter, C, can be defined as

$$C = \frac{\kappa \tau_{ext} \sqrt{1+\alpha^2}}{\tau_L}.$$

Since $\tau_{ext} = \frac{2L_{ext}}{c}$, and $\tau_L = 2\bar{\mu}_e \frac{L}{c}$,

$$C = \frac{\kappa L_{ext} \sqrt{1+\alpha^2}}{\bar{\mu}_e L}. \tag{2.64}$$

The C parameter depends on both the amount of feedback and on the target distance, L_{ext}. Feedback regimes can be divided into 4-categories (Giuliani et al. 2002).

- C<<1 (very weak feedback regime): Self-mixing signal takes cosine shape.
- 0.1<C<1 (weak feedback regime): Self-mixing signal gets slightly distorted.
- 1<C<4.6 (Moderate feedback regime): Self-mixing signal becomes sawtooth like and exhibits hysteresis.
- C>4.6 (Strong feedback regime): Laser diode enters in the mode-hopping regime and interferometric measurements are no longer possible.
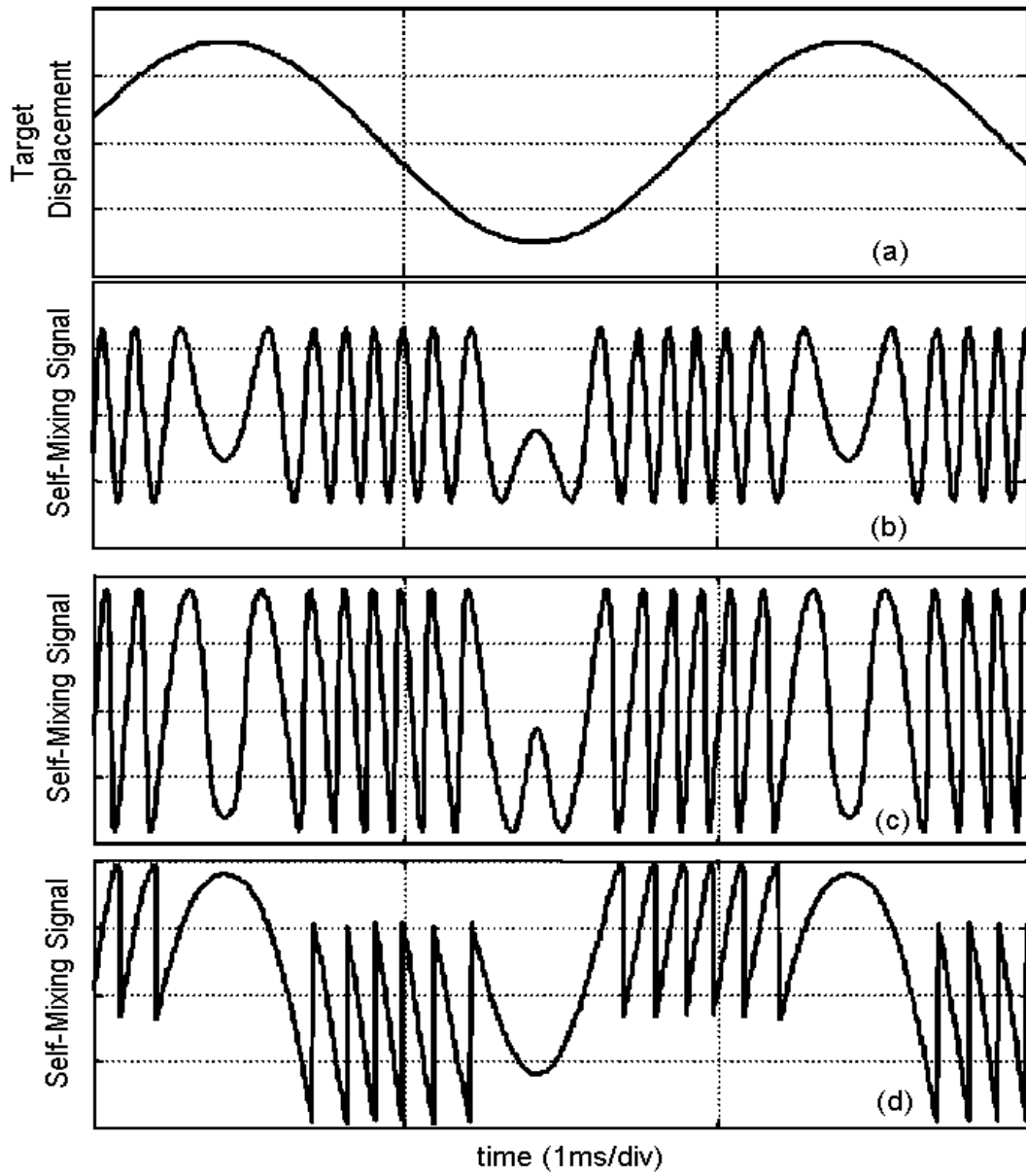
Figure 12 - (a) Signal driving the target; (b) Self-mixing output for C=0.01; (c) Self-mixing output for C=0.7; (d) Self-mixing output for C=3.3 (Donati 2004).

Chapter 3

Experimental Setup: Velocimetry and Vibrometry

This chapter begins with the block diagram of the experimental setup. Then the vibration measurements using the self-mixing setup are presented and the results are compared with the conventional Michelson interferometer. It is then followed by the velocity measurement setup.

3.1   Experimental Setup
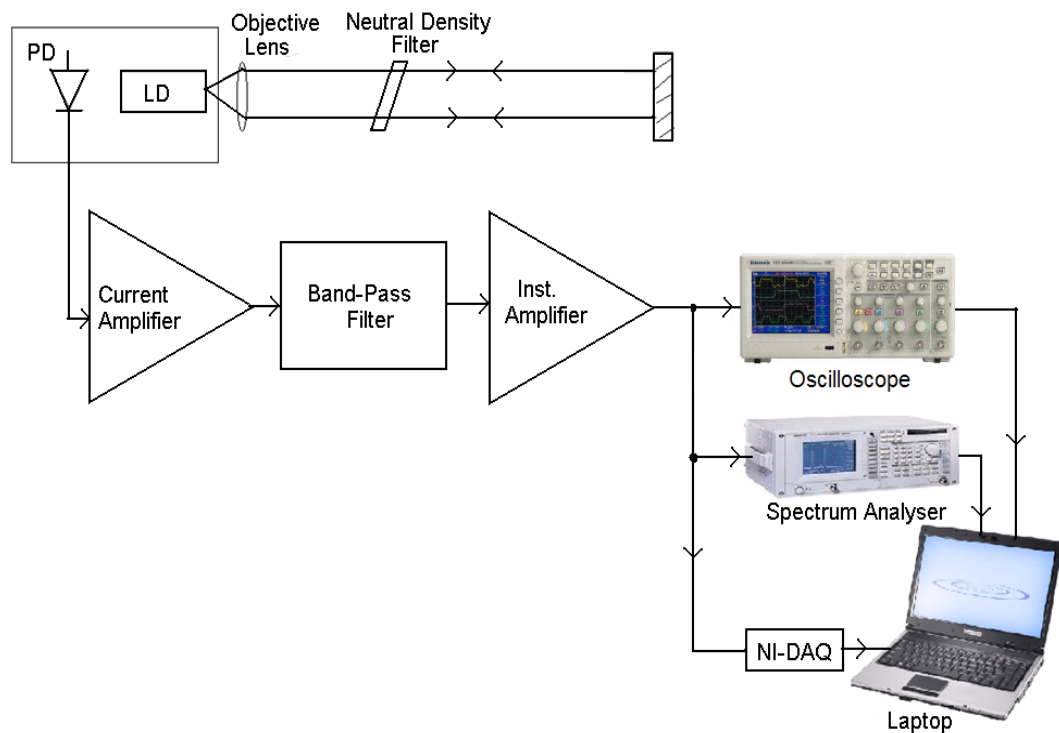
Figure 13 - Block diagram of the self-mixing setup.

The block diagram of the experimental setup is shown in the Figure 13. A single longitudinal mode laser diode (HL6724MG, Hitachi, Japan) is used in the setup of the self-mixing velocimeter. The laser is a 5 mW AlGaInP multi-quantum well (MQW) device with built in monitor photodiode. It emits visible light output of 670 nm. The visible beam is chosen because it is easy to align and focus the light on the target. Apart from HL6724MG, the laser diodes listed in Table 1 (all of

them are single longitudinal mode and have built in monitor photodiode) are also used.

Laser Diode	Typical Wavelength	Optical Power
HL6314MG	635 nm	3 mW
HL6722G	670 nm	5 mW
DL3149-057	670 nm	7 mW
L780P010	670 nm	10 mW
ML976H11F (DFB laser)	1550 nm	6 mW

Table 1 - Different types of laser diodes used

A collimator lens (C110TM-B, Thorlabs, USA) is used to collimate the beam of the laser diode. This is a glass aspheric lens with an anti-reflection coating at 600 to 1050 nm wavelength, focal length of 6.24 mm and numerical aperture of 0.4.

Laser diode and collimator lens are mounted on a temperature-controlled laser diode mount (TCLDM9, Thorlabs, USA). The mount is used in conjunction with a thermoelectric temperature controller (TEC2000, Thorlabs, USA) which allows a laser diode to operate at a precise temperature for wavelength stability. The thermoelectric temperature controller has the setting accuracy of $\pm 0.2\%$. At times smaller laser diode mount (LDM21, Thorlabs, USA) was also used to mount the laser diode. LDM21 is physically small compared to TCLDM9. The former has the cooling capacity of 5 W whereas the later has that of 20 W.

The laser diode is driven by a constant current generated by the laser diode driver (LD1255R, Thorlabs, USA). When the small fraction of frequency shifted laser light backscattered from the moving target is coupled back and coherently mixed with the source light into the laser cavity, it produces a beat frequency intensity modulation. The Doppler frequency detected is proportional to the velocity of the moving target (de Groot et al. 1988). In our setup, the optical power (containing the vibration or velocity information) is detected by the monitor photodiode housed inside the laser diode package.

The photodiode is operated in photovoltaic (zero bias) mode to monitor the self-mixing signal. Photovoltaic mode is chosen as we would like to keep the electrical noise as small as possible and the circuit simple.
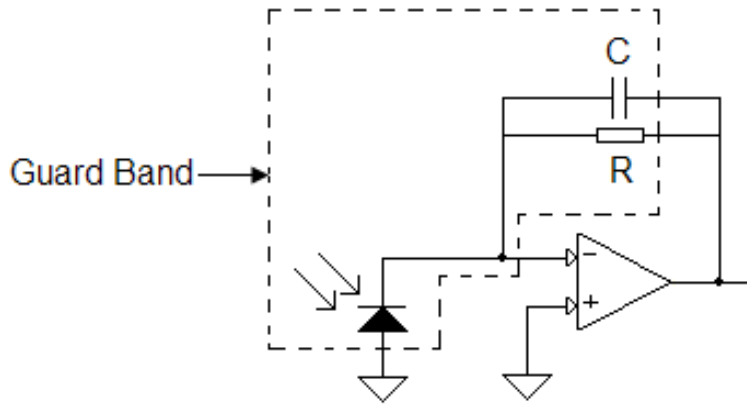
Figure 14 - Schematic of current amplifier.

After some experimentation with a couple of operational amplifiers AD820 (Analog Devices, USA) was chosen for the current amplifier. AD820 has a gain bandwidth product (GBP) of 1.8 MHz and input noise of 13 nV/$\sqrt{Hz}$, 0.8 fA/$\sqrt{Hz}$. However, the experiment works equally well with other low noise operational amplifiers. Figure 14 shows the schematic of the current amplifier. A guard band was employed to reduce parasitic leakage current by isolating the amplifier's input from the large voltage gradients across the PCB. Current amplifier was also successfully designed and implemented on the self-mixing system using OPA847 (Texas Instruments, USA) with GBP of 3.9 GHz and input noise 0.85 nV/$\sqrt{Hz}$, 2.5 pA/$\sqrt{Hz}$. The other operational amplifiers used were OPA301 (Texas Instruments, USA) with GBP of 150 MHz and input noise 3 nV/$\sqrt{Hz}$, 1.5 fA/$\sqrt{Hz}$ and LM358 (National Instruments, USA) with GBP of 1 MHz. With higher GBP, higher gain can be achieved for the same bandwidth.

The signal from the current amplifier is then filtered and amplified. The filter used is just the RC high pass filter to block DC. Then a voltage amplifier (AD820) is used to amplify the signal. Alternately an instrumentation amplifier (INA115, Texas Instruments, USA) was also used to amplify the self-mixing signal.

An oscilloscope (TDS2004B, Tektronix, USA) was used to visualise and record the output signal. A screen shot of signal can be saved directly on USB flash drive or to the computer using a USB cable, VISA and suitable program. In this setup, a LabVIEW VI was used to interface the TDS2004B with the computer.

A dynamic signal analyser (3561A, Hewlett-Packard, USA) was also used to visualise the output signal. Virtually all of the measurement functions of the

3561A are remotely programmable via the Hewlett-Packard Interface Bus (HP-IB). This property was used in conjunction with LAN/GPIB gateway (E5810, Agilent, USA) to record the data. The 3561A was connected to E5810 via GPIB which was then connected to the LAN. The measurement of 3561A is accessed via laptop connected in the LAN using Agilent VISA. A program written in C by Scott (2002) was used to transfer data from 3561A to the computer.

Alternately, a data acquisition card (NI USB-6210, National Instruments, USA) was also used in conjunction with the laptop to record experimental data. The signal is then sampled and digitised by data acquisition card and analysed using suitable software (LabVIEW and MATLAB) and computer.

3.3   Vibration Measurement
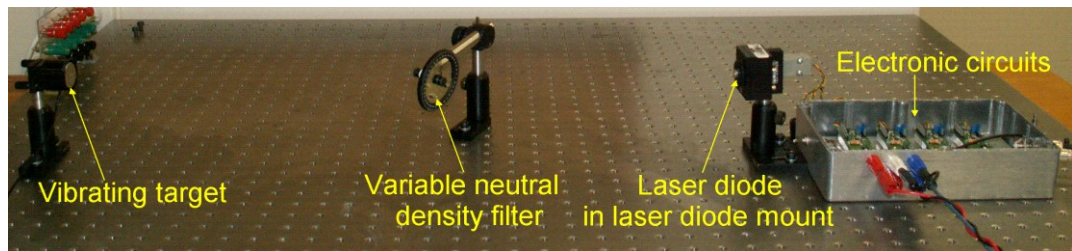
Figure 15 - Experimental setup for vibration measurement using self-mixing interferometer.

The block diagram of the experimental arrangement is shown in Figure 13 and the experimental setup is shown in Figure 15. The target used here is a front surface mirror mounted on a piezo-electric actuator. The distance between the laser diode and the target (mirror) is set to be 0.6 m. However the maximum distance (between laser diode and the target) up to which self-mixing effect is observed using HL6724MG is 1.65 ± 0.005 m. The variable neutral density filter (or alternatively de-focusing of the laser) is used to limit the back reflection to range of C=1 to 4.6.

Figure 16 shows the self-mixing signal (upper trace) and the signal driving the piezo-electric mirror (lower trace). In this case, the target was driven by a 31.5 Hz sinusoidal wave. Since the moderate feedback is allowed back to the laser, the self-mixing signal has a slightly distorted shape.
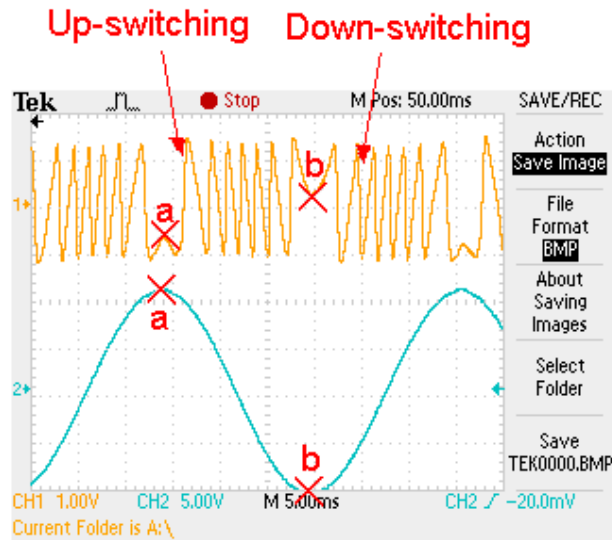
Figure 16 - Upper trace: Self-mixing signal with moderate feedback; Lower trace: Driving signal.

In Figure 16, the moving target is generating a periodic saw-tooth like optical power fluctuation. The full swing of power corresponds to a half-wavelength displacement ($\lambda / 2 \approx 335 \text{ nm}$). The distortion in the shape (switching) can be used to discriminate the direction of movement of the target. The 'up-switching' shows the target is approaching towards the laser and the 'down-switching' shows the target is moving away from the laser (Bosch et al. 2001).
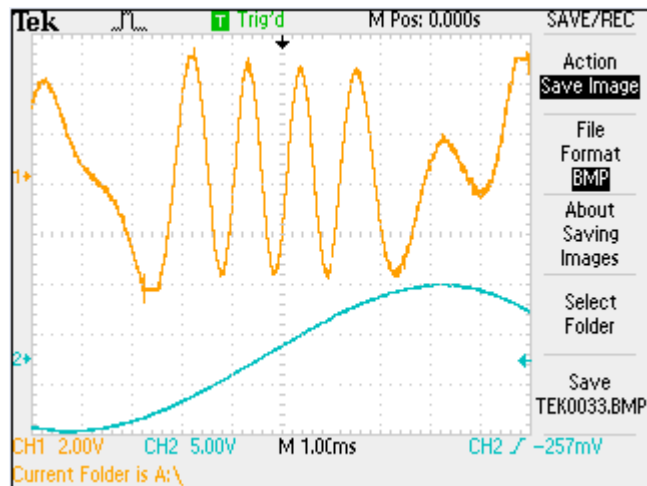
Figure 17 - Upper trace: Self-mixing signal with low level of feedback; Lower trace: Driving signal.
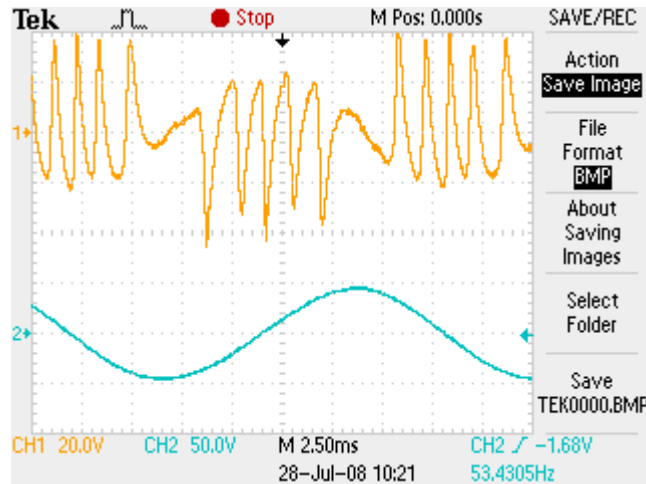
Figure 18 - Upper trace: Self-mixing signal with high level of feedback; Lower trace: Driving signal.

Figure 17 depicts the self-mixing signal generated by the low level of feedback in upper trace and driving signal in the lower trace. Similarly Figure 18 shows the self-mixing signal generated with the high level of feedback with the driving signal. The results are in good agreement with the analytical results as stated in chapter 2. The measurement of vibration of the target is then verified using a Michelson interferometer.

The experimental setup is shown in Figure 19. The laser used in the Michelson interferometer is 1 mW diode laser with wavelength of 633 nm. The same target (front surface mirror mounted on the piezo-electric actuator) is excited using sinusoidal wave of same voltage and frequency. The target is excited using 8 V, 12 V, 16 V and 20 V of 40 Hz, 50 Hz, 60 Hz, 70 Hz, 80 Hz, 90 Hz and 100 Hz sine waves. The measurement was repeated ten times for each setting.

For both interferometers (self-mixing and Michelson), the velocity of the target is calculated by counting the fringes and multiplying it by $\lambda / 2$. For e.g., in Figure 16, there are 7 full swing of power between points a and b. Thus the amplitude of vibration is 2.345 µm in 0.0158 s. Hence the velocity of the target is $1.47*10^{-4}$ m/s. The data from the Michelson interferometer setup is used as a reference data to compare with the measured data from the self-mixing setup.
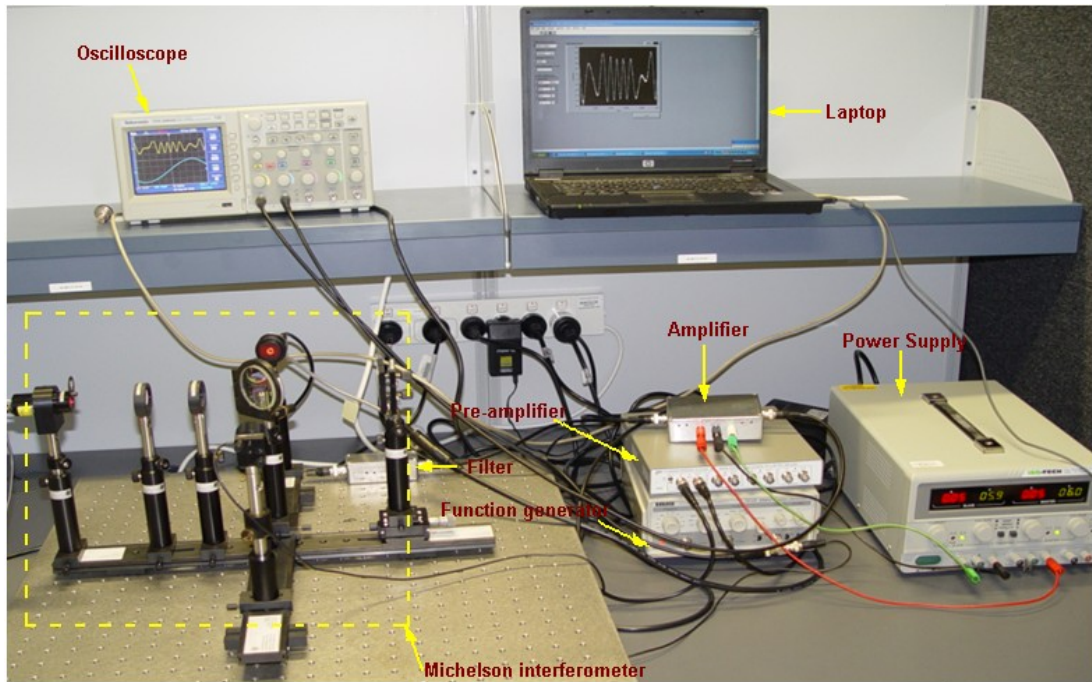
Figure 19 - Experimental setup for vibration measurement using Michelson interferometer.

Figure 20 - Measured velocity vs reference velocity.

Figure 21 - Residuals of measured velocity (y-axis) vs reference velocity(x-axis).

The standard deviation (σ) of the measured data is calculated as:

$$\sigma = \sqrt{\frac{1}{i-1}\sum\left(u_j - u_{jfit}\right)^2} \qquad (3.1)$$

where,

i is the no. of measurements, u_j is the jth measured velocity and u_{jfit} is the jth point of the fit. In Figure 20, blue circles represent the data points, vertical error bars represents 2σ, the dashed black line represents the line with x=y and the red solid line is a linear fit of data points ($y = 1.0585 * x - 1.7291^{-20}$).

Ideally the measured data should overlap with the line x=y. However in Figure 20, there is a constant deviation between them. The wavelength of the laser diode used in the Michelson interferometer is 633 nm and that of the self-mixing interferometer is 670 nm. The resolution of the measurement is only half of wavelength. I.e. for the half wavelength movement of our target, Michelson interferometer is going to read 316.5 nm and self-mixing interferometer is going to read 335 nm. i.e. 335 nm/316.5 nm = 1.058 which is the slope of the line fitted through the data points. Therefore this results in a constant error of 5.85 % between measured and reference data. Figure 21 shows the residuals of measured velocity versus reference velocity.

3.4   Velocity Measurement

Block-diagram for the measurement of velocity using Doppler effect is shown in Figure 23 and the experimental setup is shown in Figure 22. Distance between the laser and motor (L) is set to be 200 ± 0.5 mm. Radius of the motor (R) is 8.07 ± 0.05 mm and the distance between the laser beam axis and the horizontal axis passing through the centre of the motor (d) is 6.4 ± 0.05 mm, measured using vernier calliper. The angle (θ) between the laser beam axis and velocity v can be determined as,

$$\cos\theta = \frac{d}{R}.$$ (3.2)

Velocity of the motor was then calculated by using the Doppler beat frequency Δv. Δv changes with the rotating speed and/or detection angle θ. In our case, θ is kept constant to determine the velocity of the rotating target. From equation (2.8)

$$\Delta v = \frac{2u\cos\theta}{\lambda} = \frac{2ud}{\lambda R}.$$ (3.3)
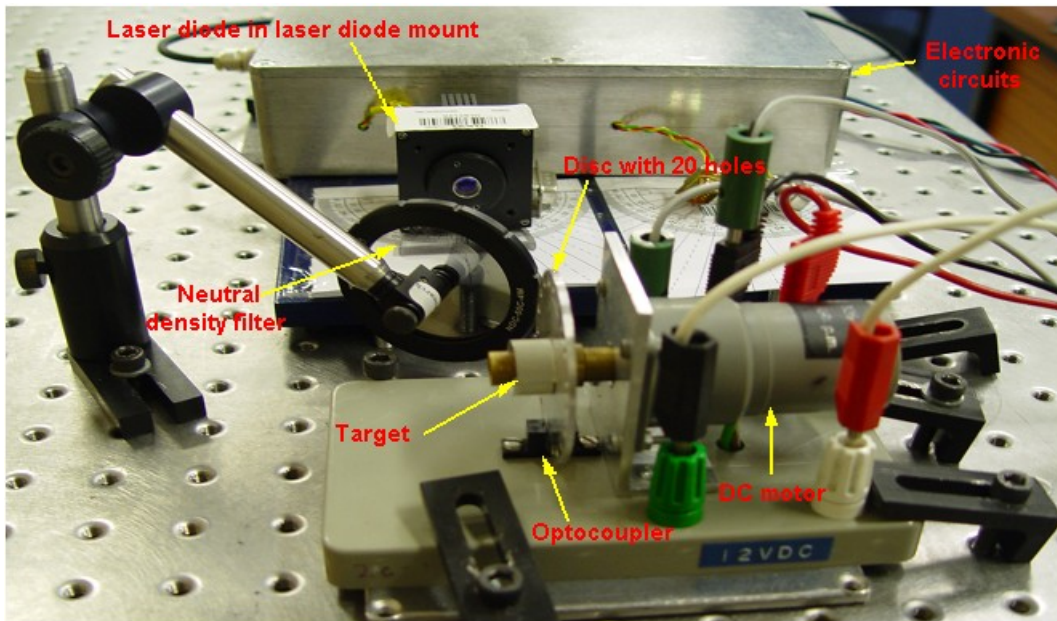
Figure 22 - Experimental setup of self-mixing interferometer for measuring velocity using Doppler effect.
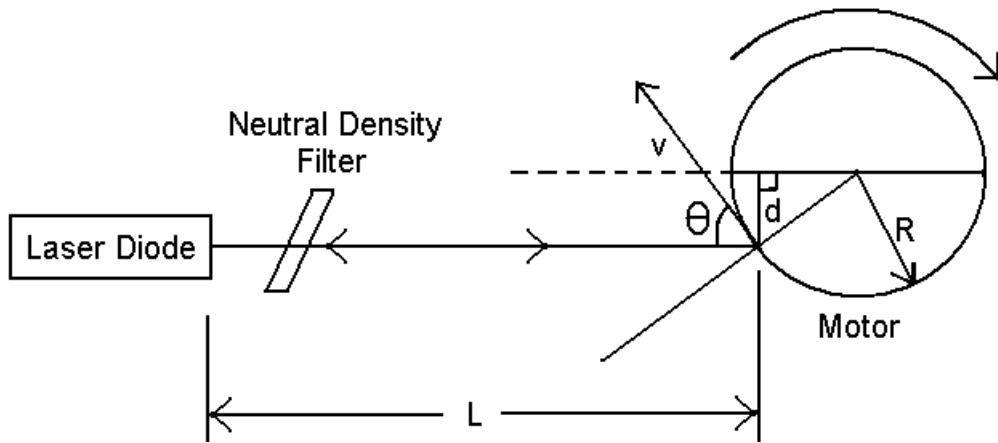
Figure 23 - Block-diagram of experimental arrangement for the measurement of velocity.

Since d, R and λ are known, we can easily calculate the velocity of the target using equation (3.3). This gives us the reference velocity. The speed of the motor was also measured using the disc mounted on the motor with 20 equally spaced holes along its circumference and a fixed opto-coupler switch. Hence, if the motor is rotating at 1 rotation per second, the oscilloscope probe connected across the opto-coupler reads 20 Hz. This gives the reference velocity.
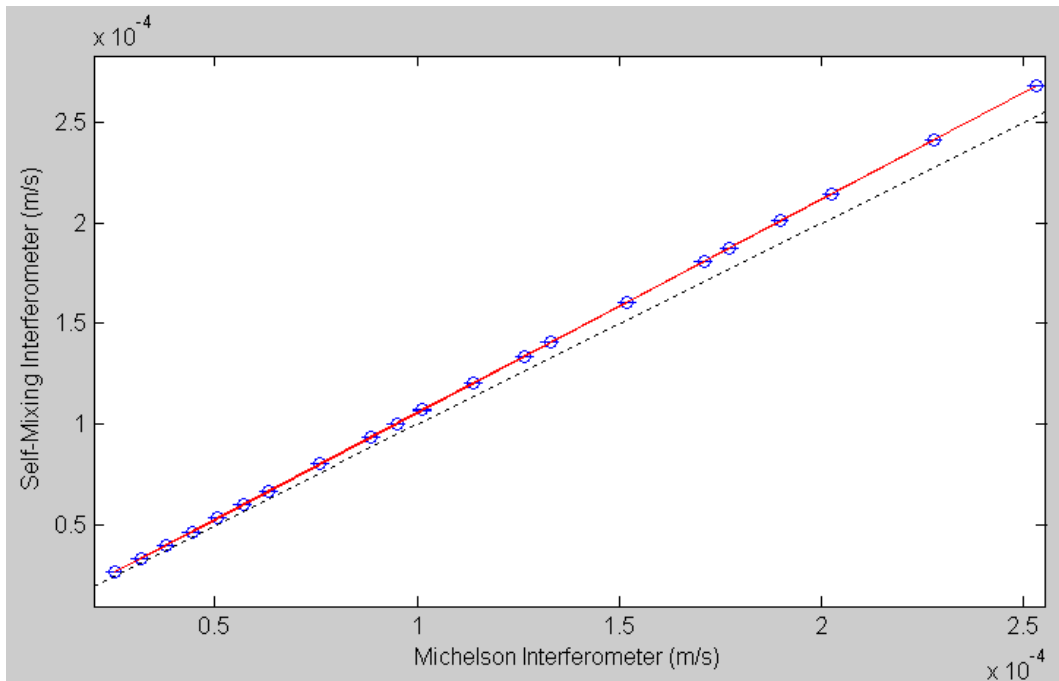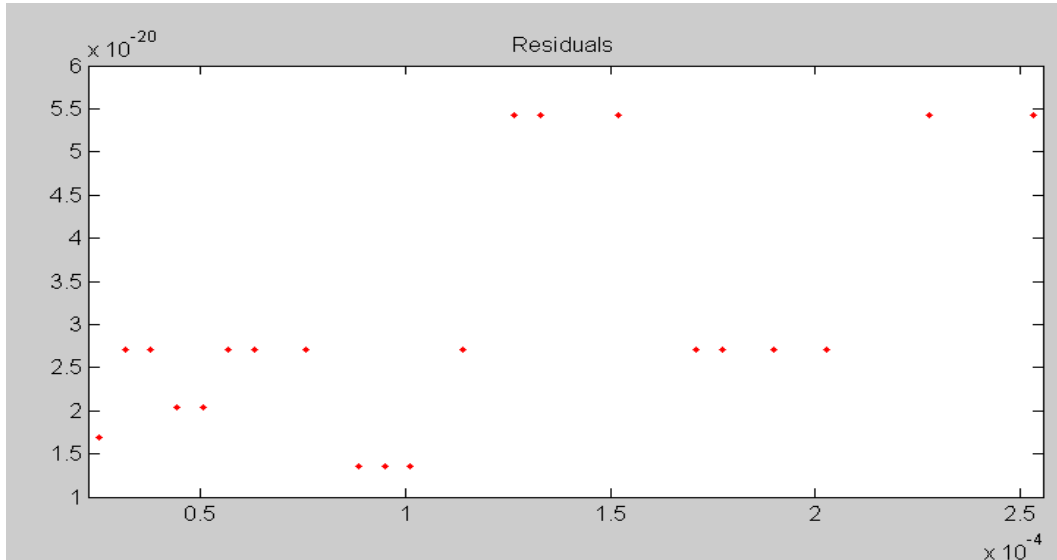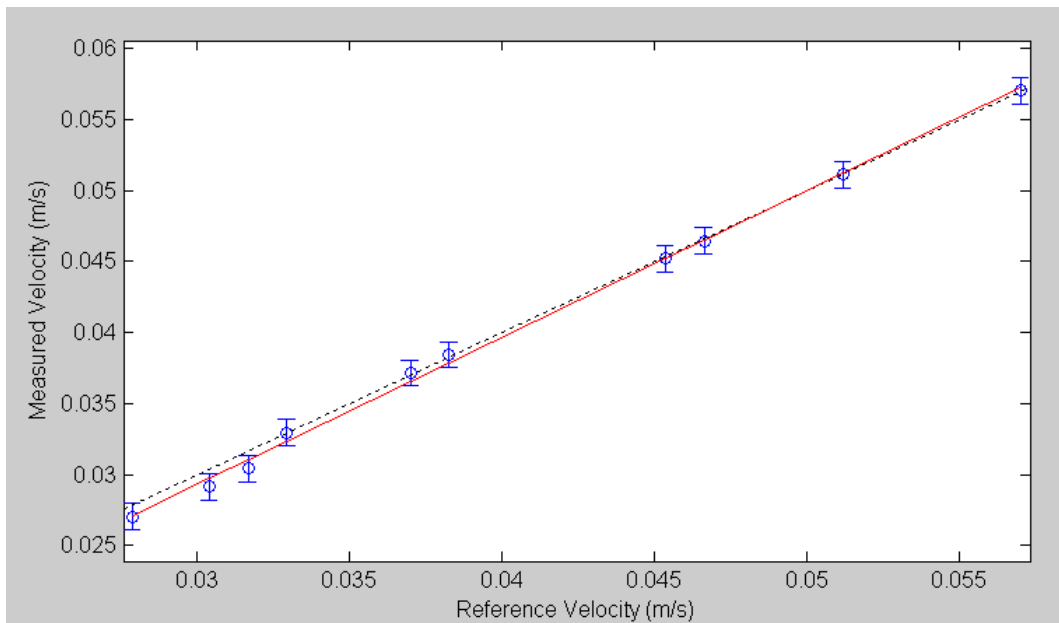

Figure 24 - Measured velocity vs reference velocity.
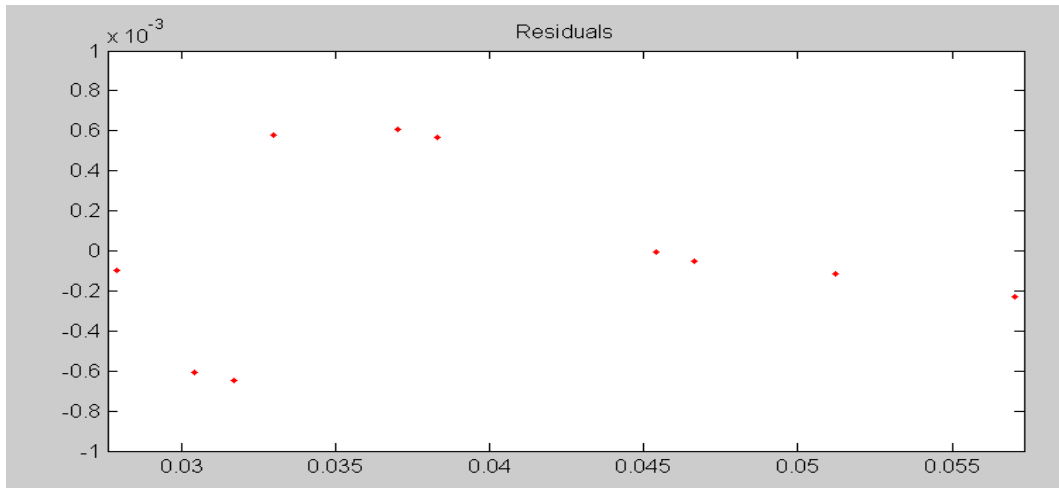
Figure 25 - Residuals of measured velocity (y-axis) vs reference velocity(x-axis).

In Figure 24, blue circles represent the data points, vertical error bars represents 2σ, the dashed black line represents the line with x=y and the red solid line is a linear fit of data points ($y = 1.033 * x - 0.0016757$).

Chapter 4

Reconstruction of the Displacement Signal

When a fraction of the laser output, after being scattered from a moving target, is fed back into the laser cavity, it generates a periodic saw-tooth like optical power fluctuation. The full swing of the power corresponds to a half-wavelength displacement ($\frac{\lambda}{2} \approx 335nm$) along the laser beam axis (Bosch et al. 2001)

$$\left| \Delta(2\pi\nu_c\tau_{ext}) \right| = 2\pi = \left| \Delta L_{ext} \right| = \frac{c}{2\nu_0} = \frac{\lambda_0}{2} . \tag{4.1}$$

With a proper sign in front of $\frac{\lambda_0}{2}$, we can reconstruct the motion of the target by adding all the half wavelength displacements.

Three different techniques for the reconstruction of the displacement of the target are presented in this chapter. In all three techniques, the self-mixing signals are obtained by using experimental setup presented in Figure 15.

4.1   Method I

4.1.1 Background

Work on the reconstruction of displacement has been published by Merlo and Donati (1997) using complex relationships between the optical power variations and displacements.

The optical output power with feedback, P_c, can be expressed as a function of the optical power without feedback, P (Bosch et al. 2001)

$$P_c = P[1 + m\cos(2\pi\nu_c\tau_{ext})] \tag{4.2}$$

where m = $\exp(-\pi\,d\nu_c\tau_{ext})$ is the modulation parameter. From equation (4.2), the normalised optical power (F) is determined (equation (2.63)):

$$F = \frac{\Delta P}{\Delta P_{max}} = \cos(\omega_c\tau_{ext}) . \tag{4.3}$$

Rewriting equation (2.56) we have

$$\omega_0 \tau_{ext} = \omega_c \tau_{ext} + \frac{C}{\sqrt{1+\alpha^2}} \left(\alpha \cos \omega_c \tau_{ext} + \sin \omega_c \tau_{ext} \right). \tag{4.4}$$

From equation (4.3) and equation (4.4)

$$\omega_0 \tau_{ext} = \arccos\left(\frac{\Delta P}{\Delta P_{max}}\right) + \frac{C}{\sqrt{1+\alpha^2}} \left[\alpha\left(\frac{\Delta P}{\Delta P_{max}}\right) + \sqrt{1 - \left(\frac{\Delta P}{\Delta P_{max}}\right)^2} \right] + m2\pi \tag{4.5}$$

$$\text{for } 0 < \omega_c \tau_{ext} < \pi$$

$$\omega_0 \tau_{ext} = -\arccos\left(\frac{\Delta P}{\Delta P_{max}}\right) + \frac{C}{\sqrt{1+\alpha^2}} \left[\alpha\left(\frac{\Delta P}{\Delta P_{max}}\right) - \sqrt{1 - \left(\frac{\Delta P}{\Delta P_{max}}\right)^2} \right] + (m+1)2\pi \tag{4.6}$$

$$\text{for } -\pi < \omega_c \tau_{ext} < 0, \text{ m=0,1,2...}$$

From the variation $\Delta P(t)$ in the output power we can determine the function $F(t) = \dfrac{\Delta P(t)}{\Delta P_{max}}$ and use equation (4.5) and (4.6) to construct $L_{ext}(t)$ as follows:

$$L_{ext}(t) = \left(\frac{1}{2k}\right) \left\{ \arccos(F(t)) + \frac{C}{\sqrt{1+\alpha^2}} \left[\alpha F(t) + \sqrt{1-F^2(t)} \right] + m2\pi \right\} \tag{4.7}$$

$$\text{for } \left(\frac{dF}{dt}\right)\left(\frac{dL_{ext}}{dt}\right) > 0$$

$$L_{ext}(t) = \left(\frac{1}{2k}\right) \left\{ -\arccos(F(t)) + \frac{C}{\sqrt{1+\alpha^2}} \left[\alpha F(t) - \sqrt{1-F^2(t)} \right] + (m+1)2\pi \right\} \tag{4.8}$$

$$\text{for } \left(\frac{dF}{dt}\right)\left(\frac{dL_{ext}}{dt}\right) > 0, m = 0,1,2...$$

Here, m is increased or decreased by 1 if $\left(\dfrac{dL_{ext}}{dt}\right) > 0$ or $\left(\dfrac{dL_{ext}}{dt}\right) < 0$,

respectively and $k = \dfrac{2\pi}{\lambda_0}$ is the wave number.

The function $F(t)$ has a distorted cosinusoid shape; however it preserves the normal periodicity of $2kL_{ext}$. When $L_{ext}(t)$ is superimposed on L_{ext0}, $F(t)$ can be applied in the following equation to compute $L_{ext}(t)$.

$$L_{ext}(t) = \left(\frac{1}{2k}\right) \left\{ -\phi_0 + \arccos(F(t)) + \frac{C}{\sqrt{1+\alpha^2}} \left[\alpha F(t) + \sqrt{1-F^2(t)} \right] + m2\pi \right\} \tag{4.9}$$

$$\text{for } \left(\frac{dF}{dt}\right)\left(\frac{dL_{ext}}{dt}\right) > 0$$

$$L_{ext}(t) = \left(\frac{1}{2k}\right)\left\{-\phi_0 - \arccos(F(t)) + \frac{C}{\sqrt{1+\alpha^2}}\left[\alpha F(t) - \sqrt{1-F^2(t)}\right] + (m+1)2\pi\right\}$$
(4.10)

$$\text{for } \left(\frac{dF}{dt}\right)\left(\frac{dL_{ext}}{dt}\right) > 0, m = 0, 1, 2...$$

ϕ_0 is the initial phase $2kL_{ext0}$, and $L_{ext}(t) = 0$ at $t = 0$. Based on equation (4.9) and, (4.10) Merlo and Donati (1997) have reconstructed the displacement waveforms of a laser diode feedback interferometer. This signal processing is quite accurate; however, it is restricted to the case of C<1 and requires a previous calibration to determine values of C accurately. This method is well adapted to be used with mirrors but not with non-cooperative targets (Servagent et al. 1998).

4.1.2 Algorithm and Experimental Result

The algorithm used for this method can be summarised as follows:

- Get the signal.
- Compute the first derivative of the signal. This gives us the switching pattern of the signal.
- Find out the stationary points of the driving signal (by identifying the consecutive transitions from positive to negative switching or vice-versa).
- Use equations (4.9) and (4.10) for the reconstruction of the original signal.

The algorithm was implemented using MATLAB and applied to several data sets yielding satisfactory results. Figure 26 will take us through the major steps of the algorithm.
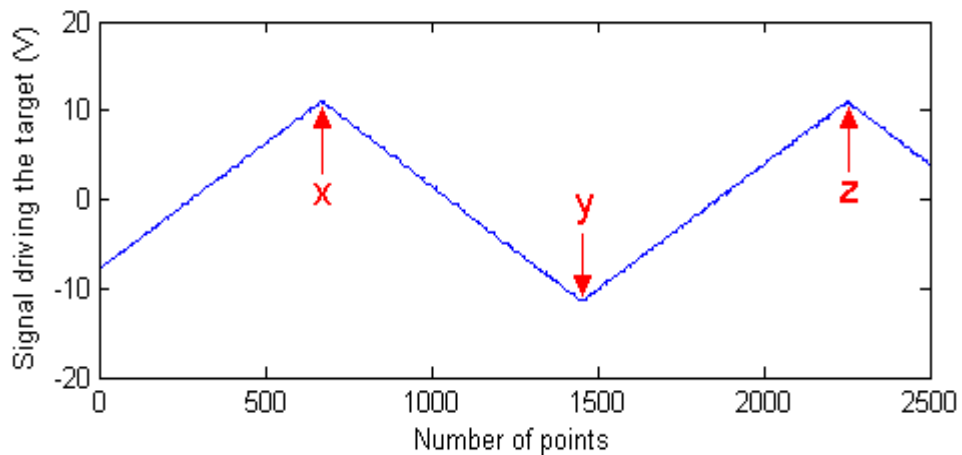
(a)
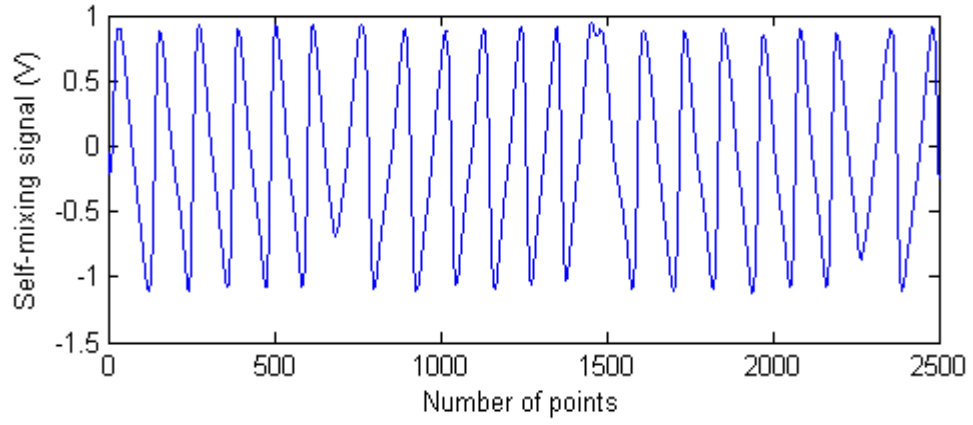
(b)
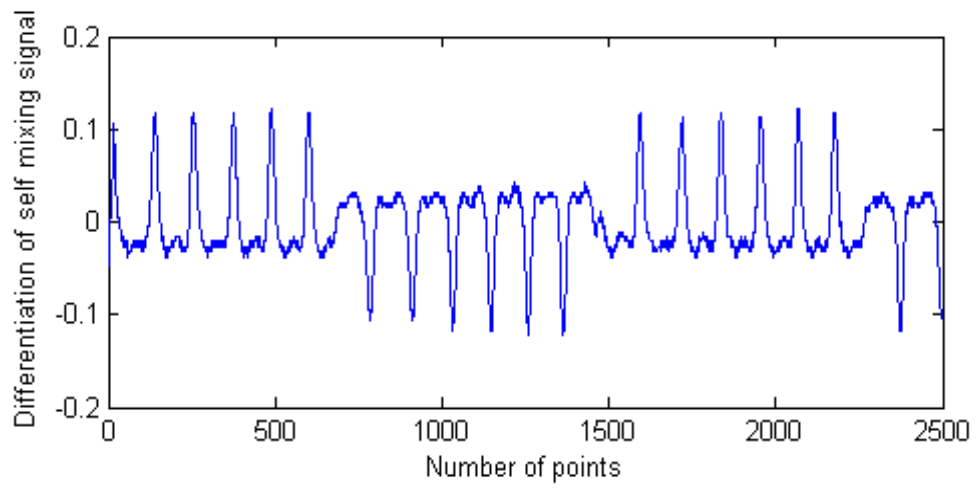
(c)
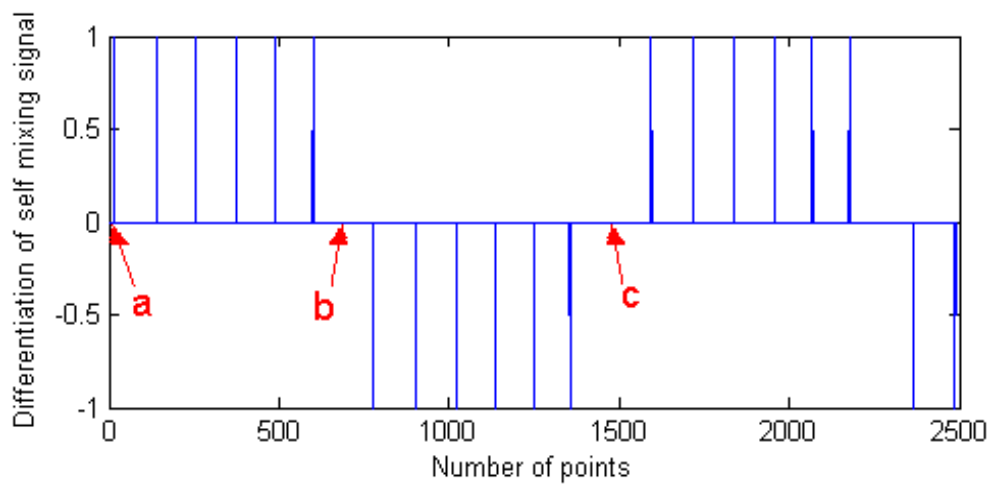
(d)
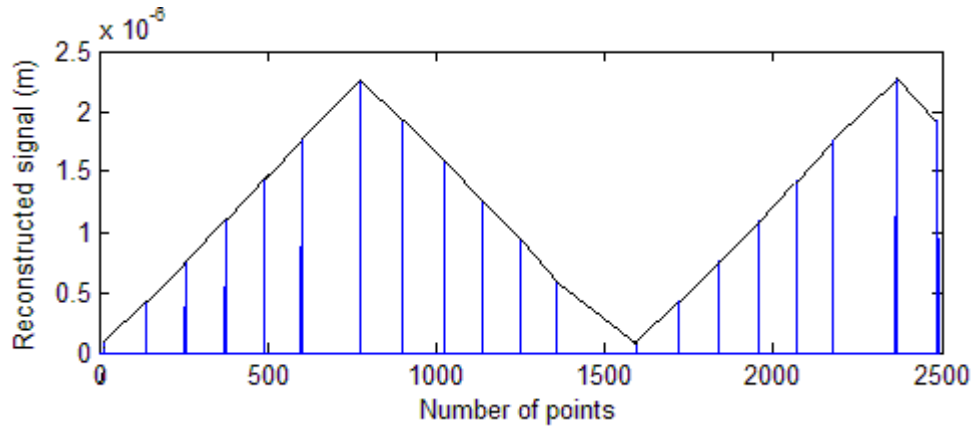
(e)

Figure 26 - (a) Signal driving piezo-electric transducer; (b) Measured self mixing signal; (c) Derivative of self-mixing signal; (d) Derivative of self-mixing signal after some processing; (e) Reconstructed signal.

Figure 26(a) shows the signal generated by the function generator used to drive the target. The target is yellow coloured insulation tape stuck on the piezoelectric oscillator. It is driven by a 31.6 Hz triangular wave. In Figure 26, 2500 points correspond to 0.05 s. At time = 0.01344 s (corresponding to the point 672 i.e., point x in Figure 26(a)), the driving signal reaches at the peak and changes direction. Similarly, it reaches a minimum at time = 0.02908 s (corresponding to the point 1454 i.e., point y in Figure 26(a)) and changes the direction. This effect can also be observed in the self mixing signal in Figure 26(b). Figure 26(a) and 28(b) are measured using oscilloscope and stored in the flash drive. These data points are then used in the MATLAB program to reconstruct the signal. Figure 26(c) illustrates the first derivative of the self-mixing signal. In Figure 26(c) we can clearly see the switching pattern of the signal which gives us the idea of whether the target is approaching towards or moving away from the laser. Figure 26(d) is obtained by setting all the points between the half of maximum point and half of minimum point of Figure 26(c) to zero and those greater than half of the maximum to +1 and smaller than half of minimum to -1. This leaves us with +1 for each upswitching and -1 for each downswitching.

As proposed in Donati et al. (1995), the vibration amplitudes can be obtained simply by adding $+\lambda_0 / 2$ from point a to b in Figure 26(d), i.e. six times, to obtain the positive amplitude and by adding $-\lambda_0 / 2$ from point b to c, which is also six times, to get the negative amplitude. Hence the vibration peak comes out to be 2.01 µm and 0 corresponding to point x and y of Figure 26(a).

Following Merlo and Donati (1997), equation (4.9) and equation (4.10) are applied to reconstruct the displacement signal. The reconstructed signal is presented in Figure 26(e). In the reconstructed signal (Figure 26(e)), the first peak and valley and the second peak are at points 776, 1495 and 2364 respectively. The corresponding vibration amplitudes ranges are 2.2 µm, 0 and 2.2 µm respectively.

4.2 Method II

4.2.1 Background

The self-mixing signal does not always have high signal to noise ratio (SNR). In spite of the realisation of the electronic circuitry in the best possible way, the signal can significantly deteriorate when used with an uncooperative target. The target's surface can be very rough compared to the wavelength of the laser diode. Speckle-pattern effects can also contribute to signal fading.

For this kind of noisy signal, it is very difficult to extract the displacement information simply by counting up-down switching. In fringe counting methods, the signal is processed using analog circuitry such as passing through high pass filter to discriminate the polarity and count the up-down switching to compute the distance. This method was proposed by Donati et al.(1995) and exploited for developing in prototype (Donati et al. 1996). However for a very noisy signal, the number of fringes could be lost and many false counts could appear. In such case, we can use a new method proposed by Norgia and Svelto (2008).

This method allows the calculation of the correct target movement at extremely low SNRs and in the presence of disturbances. In comparison with traditional fringe-counting methods, this new algorithm is not sensitive to local disturbances, such as spikes, or local loss of signal. It employs the information from several data points from the measurement to determine the instantaneous frequency. This method combines the advantages of frequency measurements with the simplicity of time-based algorithms, allowing the realisation of novel and effective

instruments (Norgia and Svelto 2008). The flowchart used by the authors is reproduced in Figure 27.
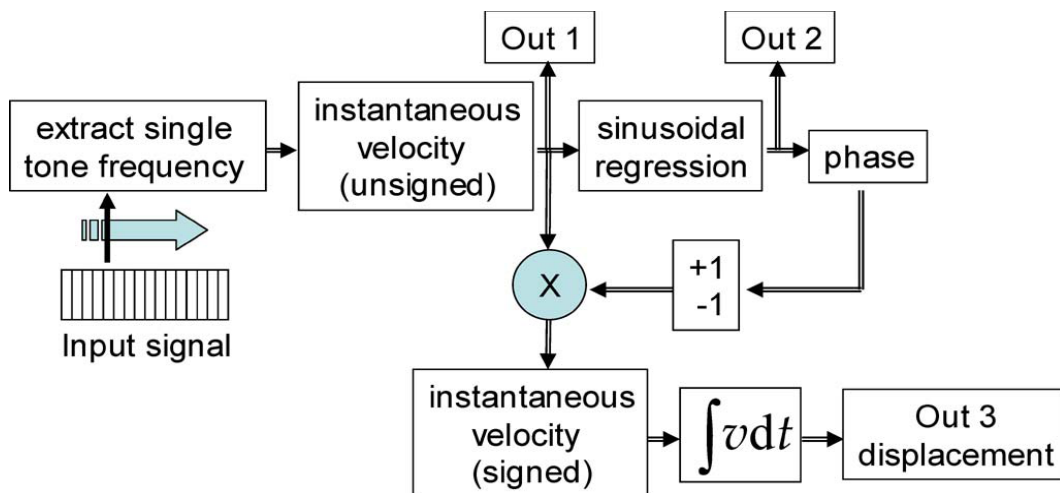
Figure 27 - Block diagram for recovering signal (Norgia and Svelto 2008).

4.2.2 Algorithm and flowchart

The algorithm used in this method can be summarised as follows:

1. Extract the single tone frequency of the signal using sliding n point window.

2. Construct an instantaneous velocity vector using the single tone frequency in step 1.

3. Compute the direction information.

4. Integrate the velocity vector to get the displacement.
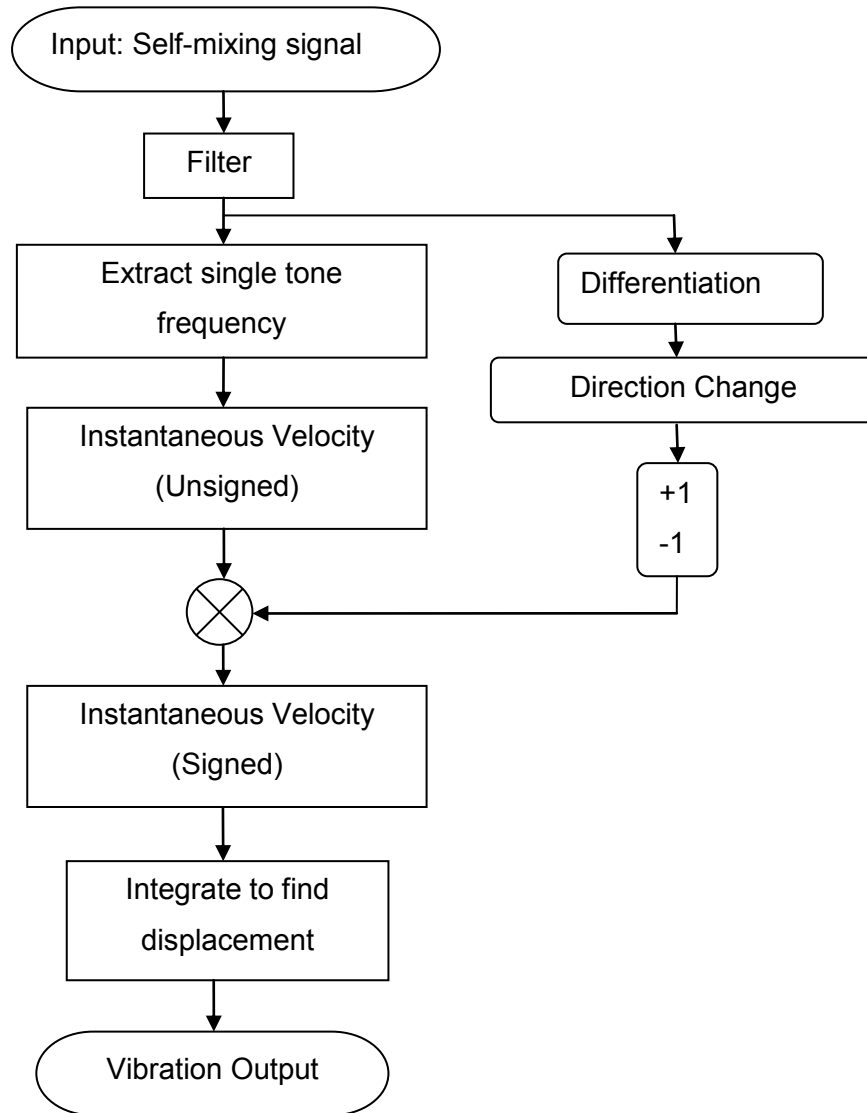
Figure 28 - Flowchart for the reconstruction of the displacement signal using method II.

Figure 28 shows the steps in more detail. In section 4.2.3, we will describe the major blocks of the flowchart.

4.2.3 Flowchart implementation

4.2.3.1 Filtering of the signal

Let the self-mixing signal, $a(t)$, be sampled at the rate, f_s (i.e. $\dfrac{1}{T}$ samples per second). If $t = nT$, a discrete sequence of $a(n) = a(nT)$ is obtained. The discrete Fourier transform (DFT) is given by (Peled and Liu 1976)

$$A\left(\frac{k}{NT}\right) = \frac{1}{N}\sum_{n=0}^{N-1} a(n)e^{\frac{-j2\pi kn}{N}} \qquad k = 0,1,2,...,N-1. \qquad (4.11)$$

The inverse DFT is given by (Peled and Liu 1976)

$$a(n) = \sum_{n=0}^{N-1} A\left(\frac{k}{NT}\right)e^{\frac{j2\pi kn}{N}} \qquad n = 0,1,2,....,N-1 \qquad (4.12)$$

where N is the length of the DFT. The DFT and inverse DFT are computed in MATLAB using a fast Fourier transform algorithm. More points are used in DFT for higher frequency resolution.

In the first step, the DFT of the signal is computed to determine the bandwidth of the signal. The signal is then passed through the band-pass filter to attenuate the noise outside the signal bandwidth. In our case, a band-pass, Butterworth filter of 9th order was used. Then the inverse FFT is taken to obtain the time domain signal.

4.2.3.2 Extracting single-tone frequency

A window of 100 points is slid through the filtered data points (for example 2500 points). The time dependent Fourier transform which is computed using a sliding window is also known as short-time Fourier transform (STFT). Window size is chosen roughly to fit one period of oscillation. It can be carefully adjusted to reject noise. The algorithm then finds the dominant frequency in the window using a FFT. The frequency component with maximum power in the window is then considered to be the single tone frequency for that set of data. To pick up the maximum power frequency bin more precisely, we use quadratic interpolation, which will be discussed in the section 4.2.3.3.

When spikes are present in the time domain signal, it can pollute the whole frequency spectrum. Since we are using only a small section of the signal at a time (a technique called windowing) for FFT, the effect of the spike will be limited in the local area. Also, the windowed signal is multiplied by the hamming window to avoid a sharp transition of the signal in the selected window.

One of the problems of the STFT can be described by the time-frequency uncertainty principle of a signal. This principle states that one cannot know the exact time-frequency representation of a signal, i.e., one cannot know what

spectral components exist at what instance of time. What one can know is the time intervals in which a certain band of frequencies exist, which is a resolution problem. In spite of this problem, we are trying to achieve our target of approximating a single-tone frequency scale in time by using the sliding window.

So the window size should at least cover one period of the signal. If the window size is too small, one may not be able to compute the necessary frequency component, i.e. frequency of the interference fringes. Whereas, computation with the bigger window size may result in loss of some of the vibrations as the window may be dominated by another strong frequency component which does not need to be included in that window. The Fourier transform gives the information of whether a certain frequency component exists or not, independent of where in time this component appears. Since we are trying to calculate a single tone frequency component in time as accurately as possible, making the window size bigger may actually result in introducing some error.

4.2.3.3 Quadratic interpolation for precise measurement of maximum amplitude frequency

For each window, the DFT gives one frequency component (x_1) with the highest power $f(x_1)$. Then other two points can be simply found as $(x_1 - 1)$ and $(x_1 + 1)$. If three points are available, a quadratic (second-order) polynomial can be expressed as (Chapra and Canale 2002)

$$f(x) = b_0 + b_1(x - x_0) + b_2(x - x_0)(x - x_1).$$

(4.13)

Equation (4.13) can be represented in more general form as

$$f(x) = a_0 + a_1 x + a_2 x^2$$

(4.14)

where

$$a_0 = b_0 - b_1 x_0 + b_2 x_0 x_1$$
$$a_1 = b_1 - b_2 x_0 - b_2 x_1$$
$$a_2 = b_2.$$

We have

$$f(x_0) = y_0, \ f(x_1) = y_1, \ f(x_2) = y_2.$$

where, b_0, b_1 and b_2 can be computed as shown below.

For our application, we can assume one unit difference between x_0, x_1, x_2. From equation (4.13), with $x = x_0$,
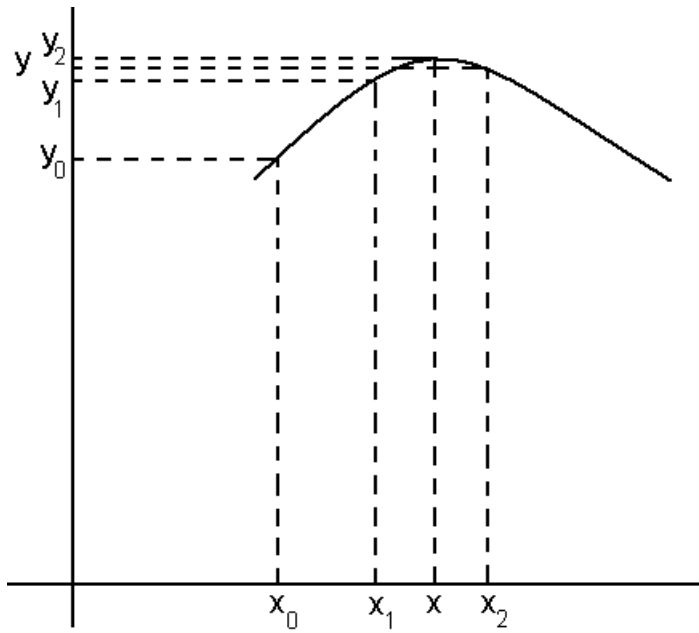
Figure 29 - Quadratic interpolation.

$$b_0 = f(x_0) = y_0 .$$
(4.15)

Equation (4.15) can be substituted into equation (4.13), which can be evaluated at $x = x_1$ for

$$b_1 = \frac{y_1 - y_0}{x_1 - x_0} = y_1 - y_0 .$$
(4.16)

Equation (4.15) and (4.16) can be substituted in equation (4.13) which can be evaluated at $x = x_2$ for

$$b_2 = \frac{\dfrac{y_2 - y_1}{x_2 - x_1} - \dfrac{y_1 - y_0}{x_1 - x_0}}{x_2 - x_0} = \frac{(y_2 - y_1) - (y_1 - y_0)}{2} = \frac{y_2 - 2y_1 + y_0}{2} .$$
(4.17)

Substituting the values of b_0, b_1 and b_2 in equation (4.13)

$$f(x) = y_0 + (y_1 - y_0)(x - x_0) + \left(\frac{y_2 - 2y_1 + y_0}{2} \right)(x - x_0)(x - x_1)$$

or

$$f(x) = y_0 + (y_1 - y_0)x + \left(\frac{y_2 - 2y_1 + y_0}{2} \right)(x^2 - x) .$$
(4.18)

Maximum point of the curve is the point where $f'(x) = 0$. i.e.

$$(y_1 - y_0) + x(y_2 - 2y_1 + y_0) - \left(\frac{y_2 - 2y_1 + y_0}{2} \right) = 0$$

or

$$x = \frac{3y_0 - 4y_1 + y_2}{2(y_2 - 2y_1 + y_0)} .$$

(4.19)

So x is closer to the maximum magnitude frequency. Here, the sinc function could have been used for even better result, however the quadratic gives a good enough value with less computation.

4.2.3.4 Calculation of instantaneous velocity

Once the instantaneous single-tone frequency is computed, the instantaneous velocity is calculated using the relation $u = f * \frac{\lambda}{2}$ resulting the unsigned velocity vector of 2401 points (for the data set of 2500 points and window size of 100 points). In the case of harmonic or nearly harmonic vibration, the velocity vector appears to be pulse shape (when plotted as unsigned velocity in y-axis and time in x-axis). Irrespective to the direction of the vibrating target, velocity will increase as the frequency of the self-mixing signal increases and decrease as the frequency decreases as shown in Figure 30.
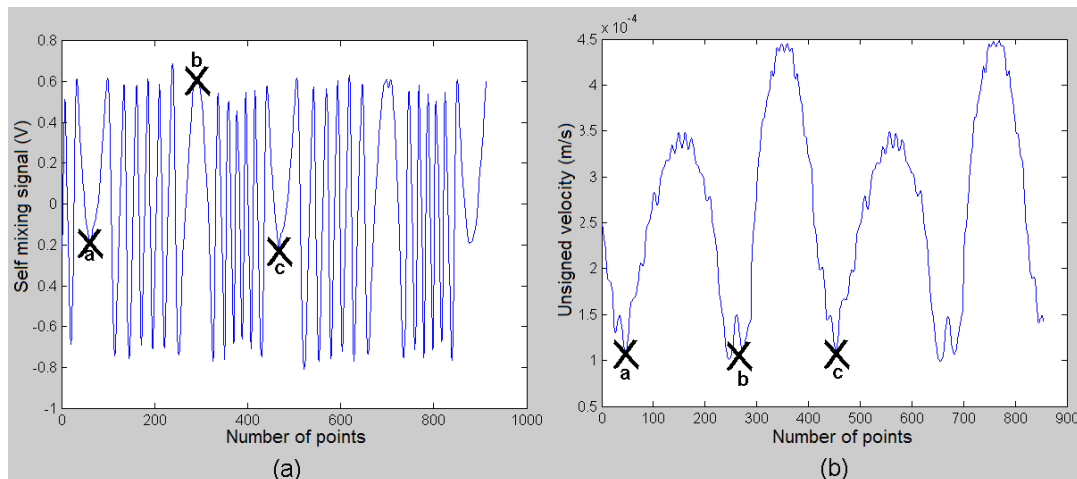
Figure 30 - (a) Self-mixing signal; (b) Corresponding instantaneous velocity.

4.2.3.5 Direction discrimination

The direction of vibration can be found by computing the first derivative of the self-mixing signal. For the self-mixing signal in the moderate feedback regime, the first derivative of the signal gives the switching pattern of the signal. As

shown in Figure 31, up and down switching shows whether the target approaches towards or moves away from the laser (Bosch et al. 2001).

However, moderate feedback from the target to the laser diode is essential to ensure a slightly distorted shape of the self-mixing signal and hence to guarantee the direction of vibration. In the case of harmonic vibration or predictable vibration of the target, the algorithm can be adjusted to avoid the necessity of moderate feedback. But in the case of a non-cooperative target and an unknown nature of the vibrating signal, finding direction becomes the limitation of this method.
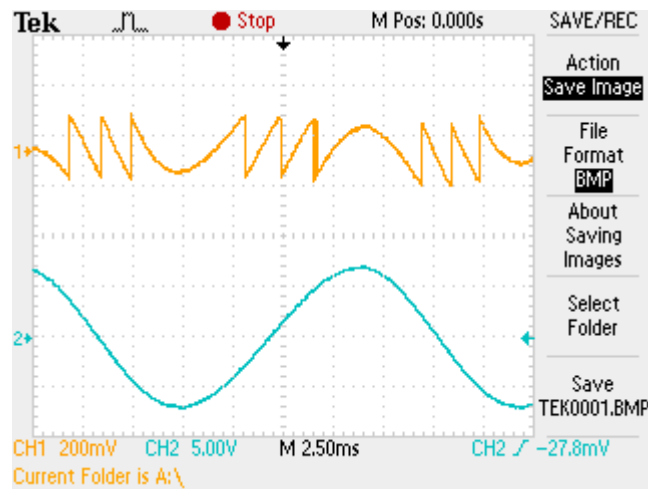
Figure 31 - Upper trace: Self-mixing signal; Lower trace: Signal driving the target.

4.2.3.6 Calculation of distance

The velocity vector is then integrated (from point a to point b) in Figure 30 which yields the distance. Point a and b are minima which can be simply calculated as follows:

- Let $f(x)$ be the function represented by blue solid line in Figure 32.
- $f'(x)$ is represented by dashed red line. In Figure 32, amplitude of $f'(x)$ is zoomed in 50 times for distinct presentation.
- $f''(x)$ is represented by dotted black line. In Figure 32, amplitude of $f''(x)$ is zoomed in 1000 times for distinct presentation.
- The program finds where $f'(x) = 0$. And if $f''(x) > 0$, at the same point, that is minima of $f(x)$ as shown in Figure 32 by magenta straight lines.
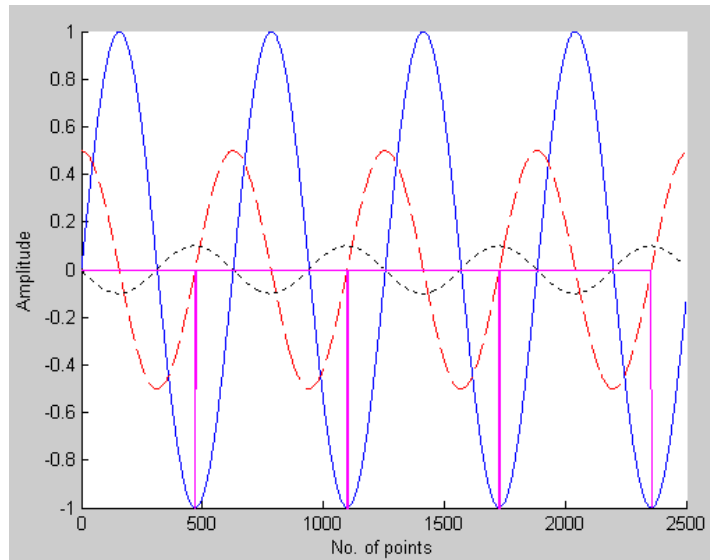
Figure 32 - Finding minima.

4.2.3.7 Experimental result and discussion

This algorithm was successfully implemented on various data sets using MATLAB. One example is presented below. Figure 33 illustrates the major steps in this algorithm.

(a)
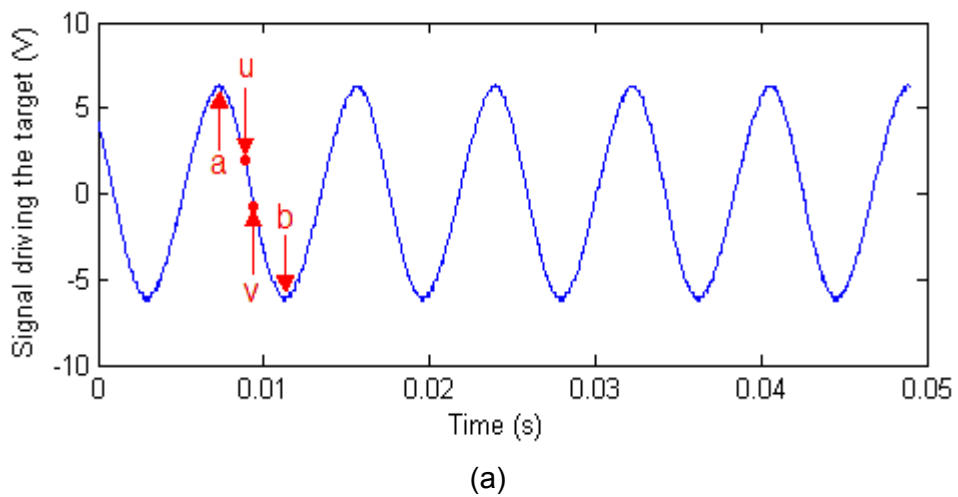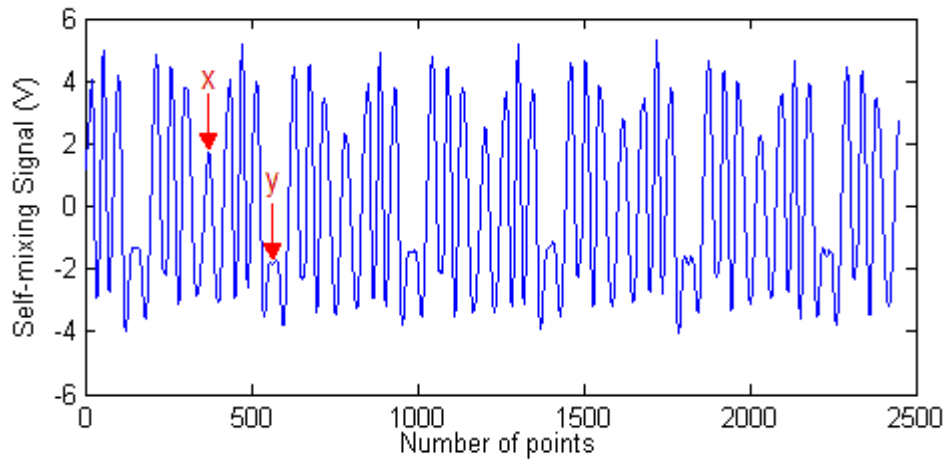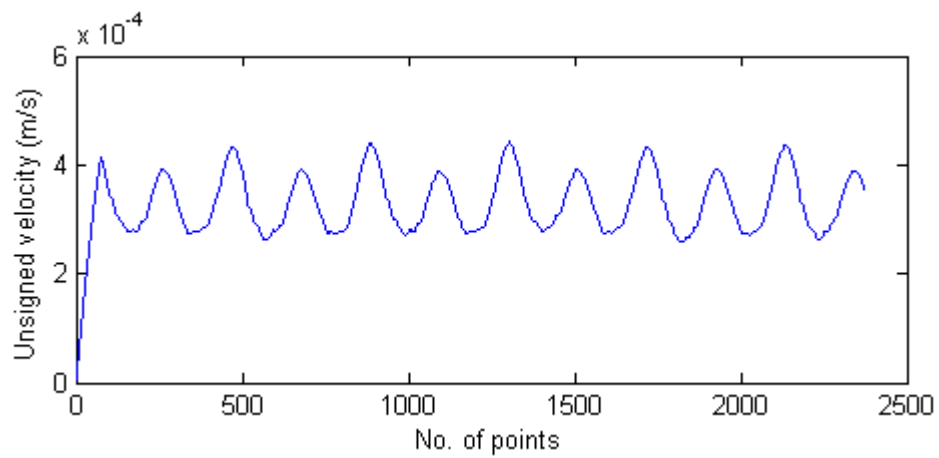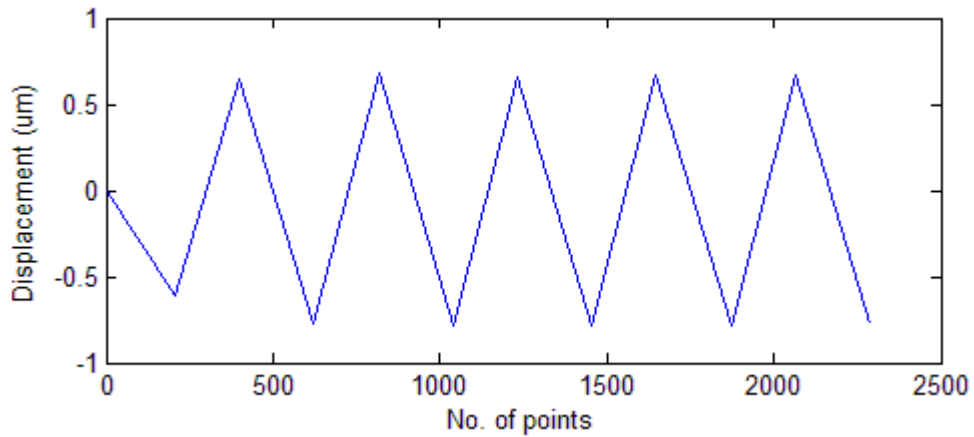
Figure 33 - (a) Signal driving the target; (b) Self-mixing signal; (c) Unsigned velocity; (d) Reconstructed displacement.

The target, yellow insulation tape stuck on the piezoelectric oscillator, is driven by a 120 Hz sine wave. In Figure 33, 2500 points correspond to 0.05 s. In Figure 33(a), at time = 7.6 x10^{-03} s (corresponding to point 380 i.e., point a), driving

signal reaches one of the peaks and changes the direction. Similarly, it reaches one of the valleys at time = 0.01184 s (corresponding to point 592 i.e., point b) and changes the direction. This effect can also be observed in self mixing signal shown in Figure 33(b) at point x and point y. Figure 33(a) and Figure 33(b) are measured using oscilloscope and stored in the usb flash drive. These data points are then used in the MATLAB program to reconstruct the signal. Figure 33(c) shows the unsigned velocity vector. Each pulse in the unsigned velocity vector slowly increases until the driving signal changes the direction. At point (for e.g.: 380 or 592), where the driving signal changes the direction, velocity is minimum. It can be observed that as the frequency of self mixing signal increases, the unsigned velocity increases and vice-versa. Once the direction of the signal is computed as discussed in section 4.2.3.5, it gives the interval of integration to convert the velocity into distance. The reconstructed displacement signal is shown in Figure 33(d). The reconstructed signal only has the amplitude of vibration (and not the points in between). In Figure 33(a) amplitudes at points u and v can be computed by integrating velocity from a to u, and a to v. This gives us the additional amplitude points in between a and b to reconstruct the signal smoothly. However, in this thesis only peak points (for e.g. points a and b in Figure 33(a)) are computed. Hence the reconstructed signal in Figure 33(d) looks triangular rather than sinusoidal.

4.3   Method III

This method is improved form of method II for a more precise reconstruction of the displacement signal with a very low SNR. In classical interferometry, target movement can be recovered using two channels. Usually signals are obtained in quadrature, i.e., $\cos(2ks(t))$ and $\sin(2ks(t))$ (Merlo and Donati 1997). However, the ambiguity of direction in self-mixing signal is suppressed by the information in direction of transition which indicates whether the driving signal is increasing or decreasing. As already mentioned in section 4.2.3.5, when used with a non-cooperative target, the self-mixing signal can lose the direction information or at least it can be very difficult to retrieve it. Sign ambiguity can also be resolved by heterodyning of the reference beam and the frequency shifted beam returning from the target. In this technique, the beam returning from the target is frequency shifted by the Doppler effect and further frequency shifted by means of an acoustic-optic modulator (Giuliani et al. 2003).

In method II, one needs to keep on adjusting the bandwidth of the bandpass filter from one signal to another signal. Also the window for STFT from one type of signal to another type of signal needs to be adjusted to get the optimum result. In method III, one does not need to keep on adjusting the bandwidth of the bandpass filter. This problem has been eliminated by using the signal de-noising technique of the wavelet transform. Still the user will have to adjust the window size from one type of signal to another type of signal, but practically the window size has better tolerance than in method II. In the following sections we will discuss the background theory of the wavelet transform followed by the flowchart and experimental results.

4.3.1 Wavelet transformation

In 1982, Jean Morlet, a French geophysical engineer, discovered the idea of the wavelet transform (Debnath 2002). The wavelet transform is the mapping of a time signal to the time-scale joint representation that is similar to the STFT. Since STFT employs a fixed window, it has a constant resolution throughout the signal. Whereas wavelet transform provides multiresolution analysis (MRA) with varying windows (Poularikas 1996).

Fourier analysis consists of breaking up a signal into sine waves of various frequencies extending from minus infinity to plus infinity. So Fourier transforms have only one set of basis functions, sine, and cosine functions, whereas wavelet analysis is the breaking up of a signal into shifted and scaled versions of the original (mother) wavelet. Mother wavelets have effectively limited duration and average value of zero. So the wavelet transform has an infinite set of possible basis functions.

The concept of the wavelet transform is easy to understand when compared with the Fourier transform and Short-Time Fourier transform (STFT). The following example is based on the work by Robertson et al. (1996).
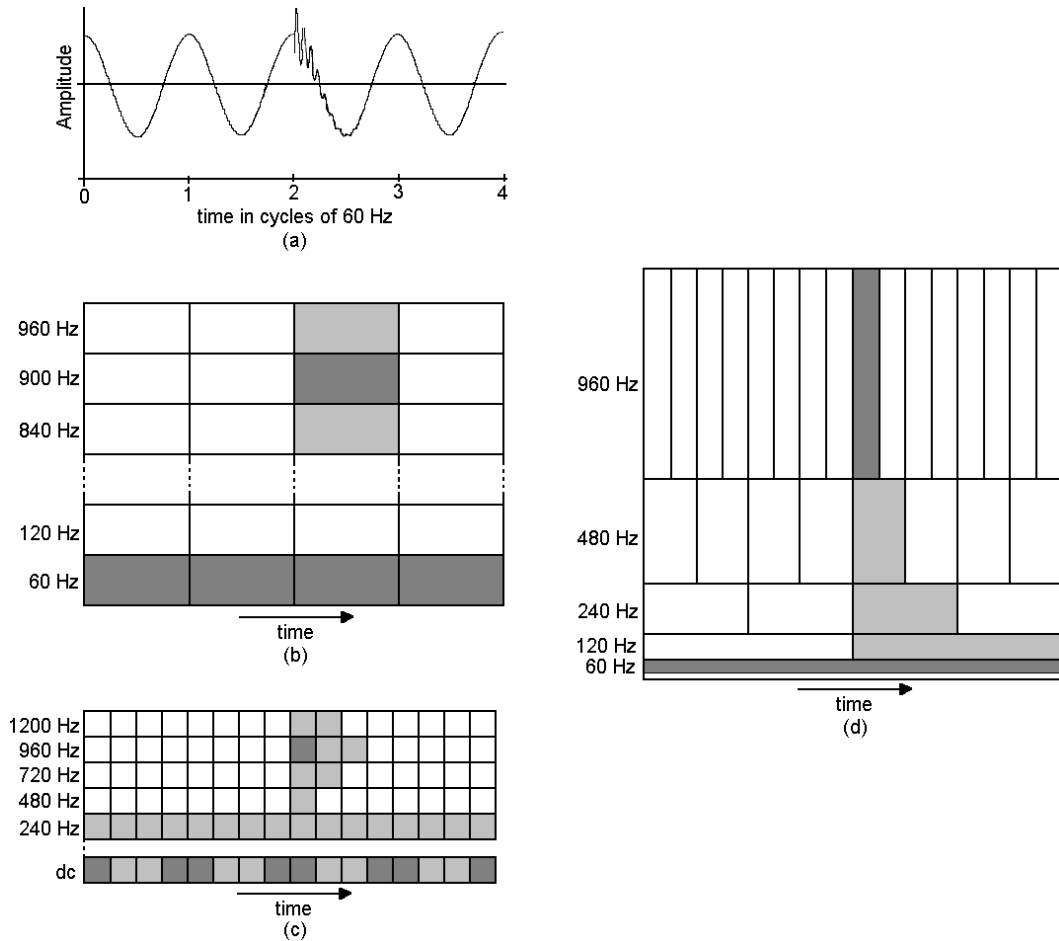
Figure 34 - (a) Input signal; (b) WDFT with the window size of 60 Hz; (c) WDFT with the window size of 240 Hz; (d) DWT (Robertson et al. 1996).

Let us consider the signal of Figure 34(a) containing transient impulse with a ring of 900 Hz superimposed on a 60 Hz fundamental. The DFT of such kind of signal will produce a sequence of discrete frequencies in the frequency domain irrespective of the time of occurrence. The non-periodic signal like transient impulse cannot be accurately represented by the summation of sines and cosines, therefore DFT does not accurately represent the signal. The windowed DFT (WDFT) is one solution to the problem of better representing the non-periodic signal.

The WDFT is the digital implementation of STFT. The WDFT of a signal can be represented in a two dimensional grid as shown in Figure 34(b) and Figure 34(c) where the divisions in the horizontal direction represent the time extent of each window; the divisions in the vertical direction represent the frequencies; and the shade of each rectangle is proportional to the corresponding magnitude (darker the shade, higher the magnitude and vice versa).

The time period of each window of Figure 34(b) time=16.67 ms fixes the frequency resolution Δf at 60 Hz. This however locates the start time of the transient only to within one 60 Hz cycle. Shortening the window period by four as in Figure 34(c) locates the start of the transient but makes Δf four times larger. As a result of the lower frequency resolution of 240 Hz, the energy of the 60 Hz fundamental appears in the dc and 240 Hz components.

This example clearly demonstrates the need of fine time resolution for short duration or high frequency signals, and fine frequency resolution for long duration or lower frequency signals. The Discrete Wavelet transform (DWT) output can be represented in a two dimensional grid in a similar manner as STFT but with very different divisions in time and frequency as shown in Figure 34(d). The rectangles in Figure 34(d) have a constant time-bandwidth product such that they narrow at the lower scales (higher frequencies), widen at the higher scales (lower frequencies), and are shaded proportionally to the magnitude of the DWT output.

When compared with the WDFT, the DWT isolates the transient component in the top frequency band at precisely the quarter-cycle of its occurrence while the 60 Hz component is represented as a continuous magnitude.

4.3.1.1 Continuous wavelet transform

Let $\vec{L}$ denote the vector space of measurable, square-integrable functions. The continuous wavelet transform (CWT) of a function $f(t) \in \vec{L}$ is given by (Poularikas 1996)

$$W_f(s,\tau) = \int f(t) h_{s,\tau}^*(t) dt \tag{4.20}$$

where, * denotes complex conjugates. The wavelets are generated from a single basic wavelet (mother wavelet), $h(t)$, by scaling and translation

$$h_{s,\tau}(t) = \frac{1}{\sqrt{s}} h\left(\frac{t-\tau}{s}\right) \tag{4.21}$$

where, s is the scale factor, and τ is the translation factor. The wavelet transform of a one-dimensional signal is a two dimensional time-scale joint representation. The mother wavelet must satisfy the admissibility condition (Poularikas 1996)

$$\int h(t) dt = 0 . \tag{4.22}$$

The inverse wavelet transform is given by

$$f(t) = \frac{1}{c_h} \int \int W_f(s,\tau) \frac{1}{\sqrt{s}} h\left(\frac{t-\tau}{s}\right) d\tau \frac{ds}{s^2} \tag{4.23}$$

where,

$$c_h = \int \frac{|H(\omega)|^2}{|\omega|} d\omega < \infty \tag{4.24}$$

where $H(\omega)$ is the Fourier transform of mother wavelet, $h(t)$. Figure 35 shows examples of some common wavelets:
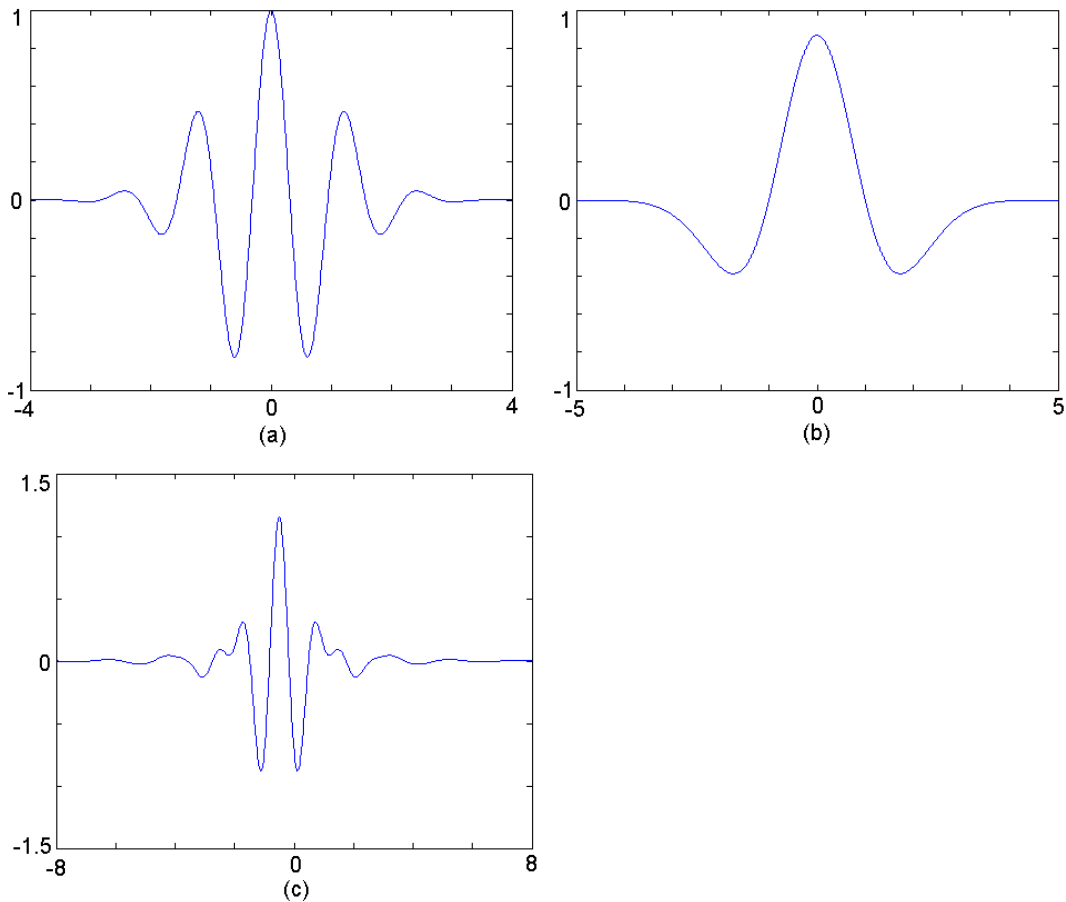
Figure 35 - (a) Morlet wavelet function; (b) Mexican hat wavelet function; (c) Meyer wavelet function.

4.3.1.2 Discrete wavelet transform

Calculating the wavelet coefficient at every possible scale requires a significant amount of computation time and resources. The Discrete wavelet transform (DWT) provides sufficient information both for analysis and synthesis of the original signal, with significant reduction in the computation time. The DWT is

derived from CWT by setting scale factor, s, to be a power of 2, and translation parameter, τ, to be an integer multiple of the scale factors. For integer i and k, (τ, a) is discrete and given as (Daubechies 1992)

$$s = s_0^i, \qquad \tau = k\tau_0 s_0^i. \tag{4.25}$$

The DWT is given by,

$$W_f(i,k) = \int f(t)h_{i,k}^*(t)dt. \tag{4.26}$$

The reconstruction of the signal $f(t)$ is given by the Inverse Discrete Wavelet (IDWT) (Poularikas 1996)

$$f(t) = \sum_i \sum_k W_f(i,k)h_{i,k}(t). \tag{4.27}$$

4.3.1.3 Multiresolution analysis

Orthonormal bases of wavelets and wavelet packets constitute useful tools for the decomposition of complicated functions into a small number of elementary waveforms that are localised both in time and frequency. Numerically these decompositions are based on the iterative application of digital filter banks (Chui et al. 1994). In 1986, Mallat and Meyer first formulated the idea of MRA (Mallat 1989).
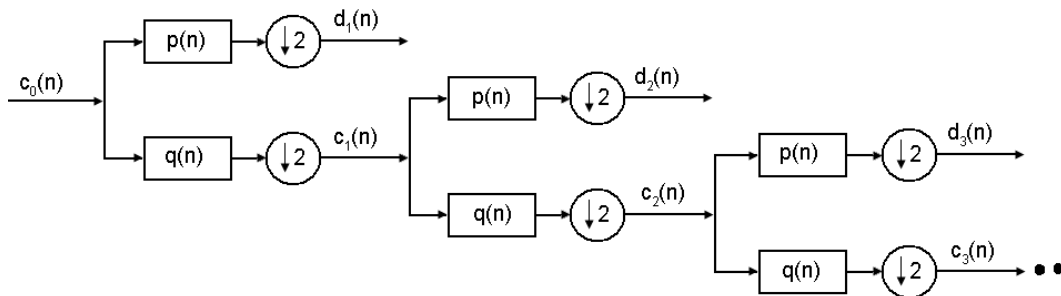
Figure 36 - Multi-stage filter bank DWT implementation (Poularikas 1996).

In Figure 36 p(n) corresponds to discrete low pass filter and q(n) corresponds to discrete high pass filter. The successive discrete approximation sequences $c_i(n)$ are lower and lower resolution version of $c_0(n)$. They are down-sampled each time they pass through the digital filter. The successive wavelet coefficient sequences $d_i(n)$ contain the difference in information between the two approximations at resolution levels (i) and (i-1).
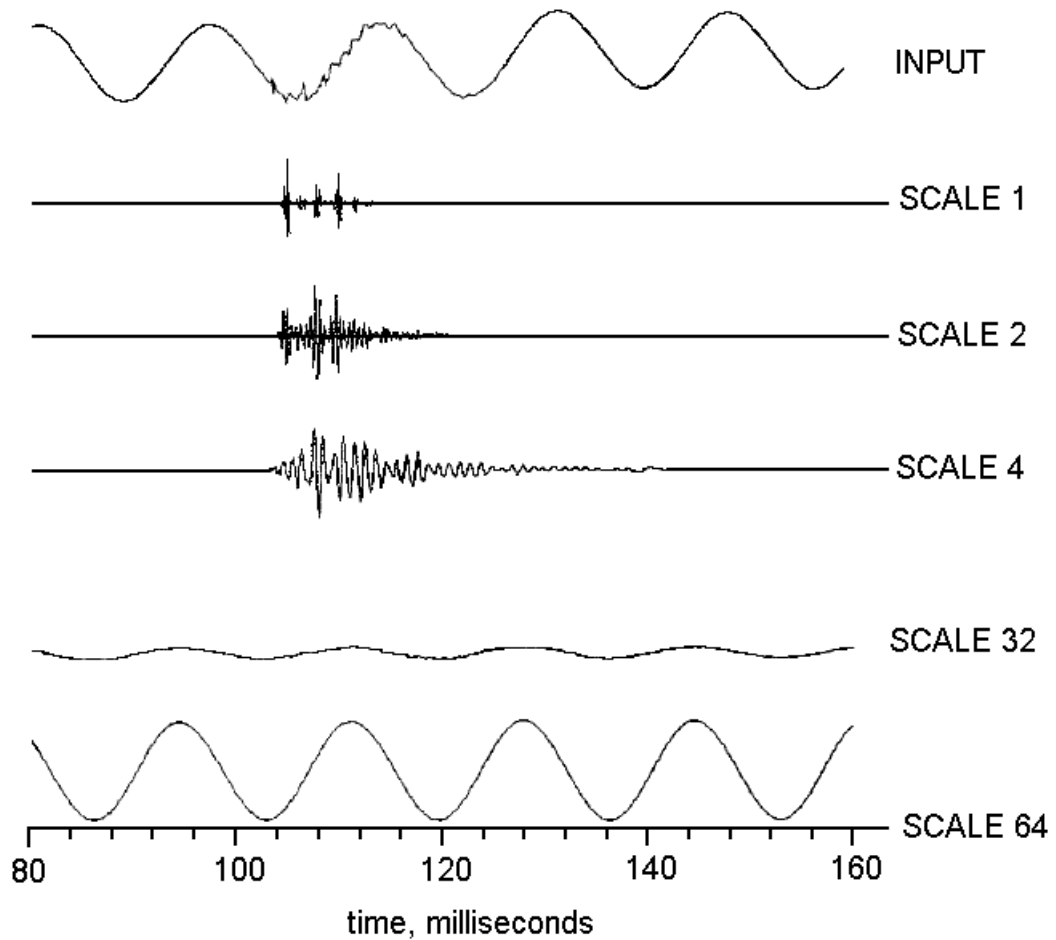
Figure 37 - MRA of the input signal (Robertson et al. 1996).

Figure 37 shows the output of an implementation of Figure 36, which is a typical wavelet MRA for an input signal. The input signal is one phase voltage of a 3-phase transmission line capacitor switching transient. The signal is decomposed with different resolutions corresponding to different scales of the wavelets. In successive scales, the relative amount of energy in each frequency band is shown.

4.3.1.4 Signal de-noising

The wavelet transform can be applied to de-noise data. Signal de-noising was proposed by (Donoho 1993). His procedure can be summarised as follows:

When data is decomposed using wavelet, the filters are used to produce coefficients which correspond to average and details. If the details are too small, they can be omitted without substantially affecting the main features of a data set.

Then hard or soft thresholding is applied. The idea of thresholding is to set to zero all coefficients that are less than a particular threshold. Hard thresholding is the simplest to apply whereas soft thresholding has nice mathematical properties and has corresponding theoretical results (Donoho 1995). Then the inverse wavelet transform is performed to reconstruct the de-noised signal. The noise in the reconstructed signal is almost entirely suppressed. Figure 38 shows the noisy signal and the de-noised signal.
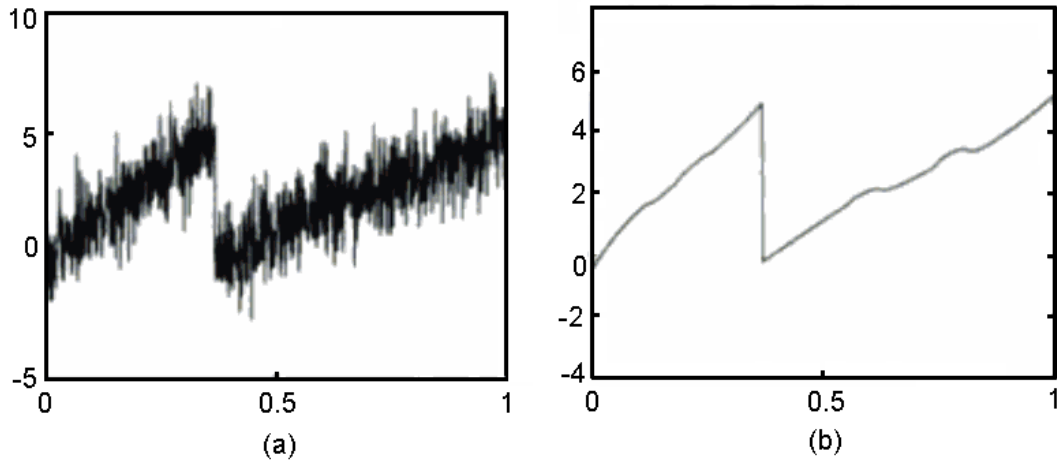
Figure 38 - (a) Noisy ramp signal; (b)- De-noised ramp signal (Chui et al. 1994).

4.3.2 Flowchart and Experimental Result

Figure 39 shows the flowchart for the reconstruction of the displacement signal. As already mentioned, Method III has been derived simply from Method II. So the similar blocks of the flowchart of Method III are not discussed in this section. Method III was successfully implemented on various data sets using MATLAB. Major steps of this method from one of the data sets are presented in Figure 40.
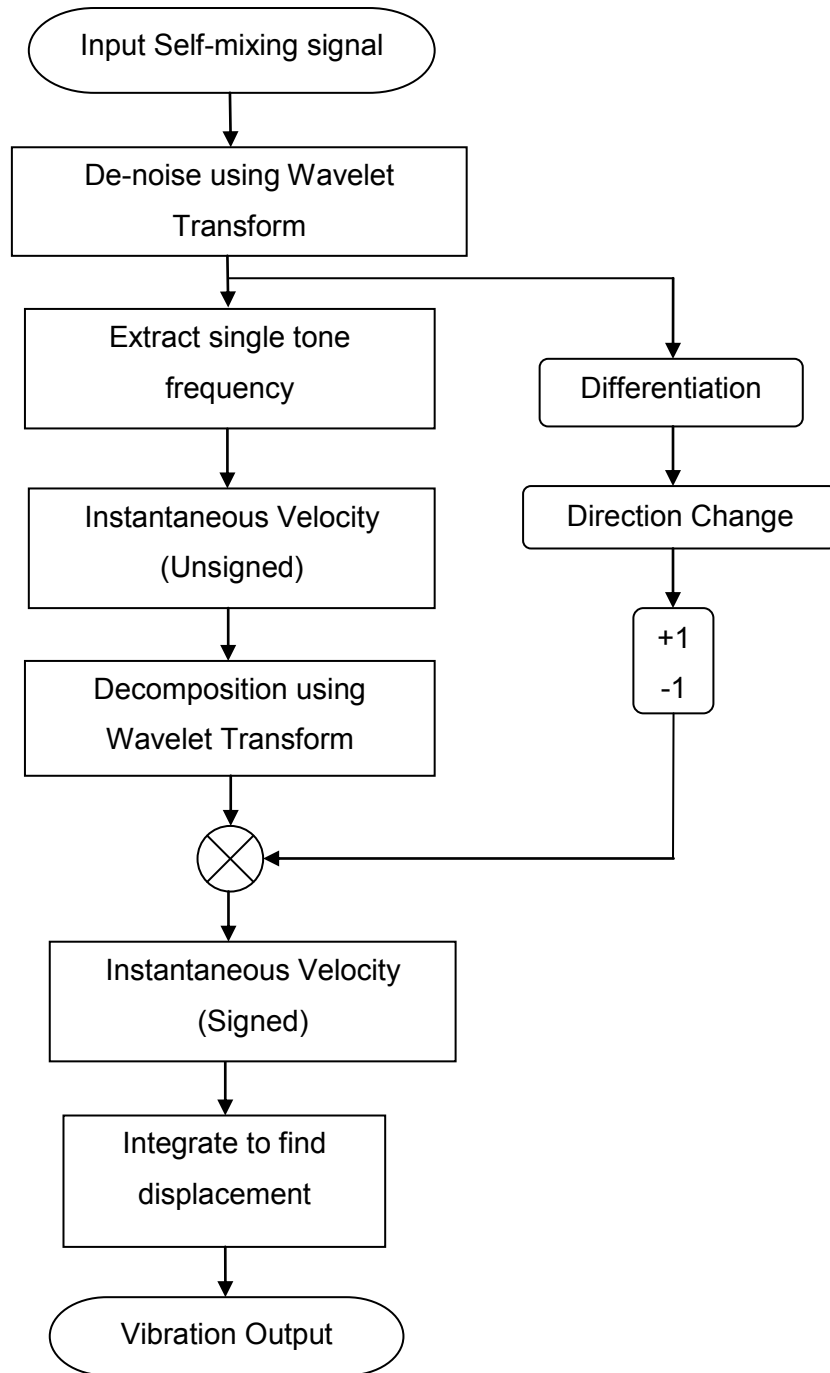
Figure 39 - Flowchart for the reconstruction of the displacement signal using method III.
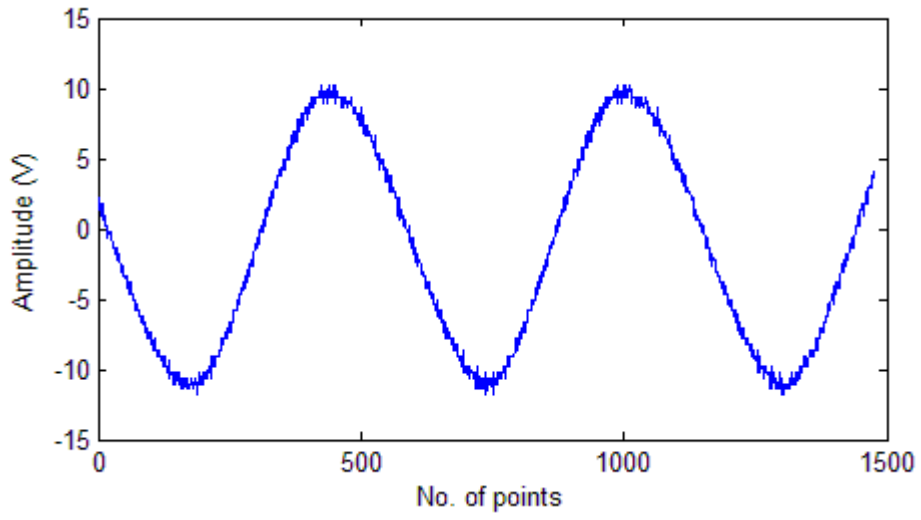
(a)
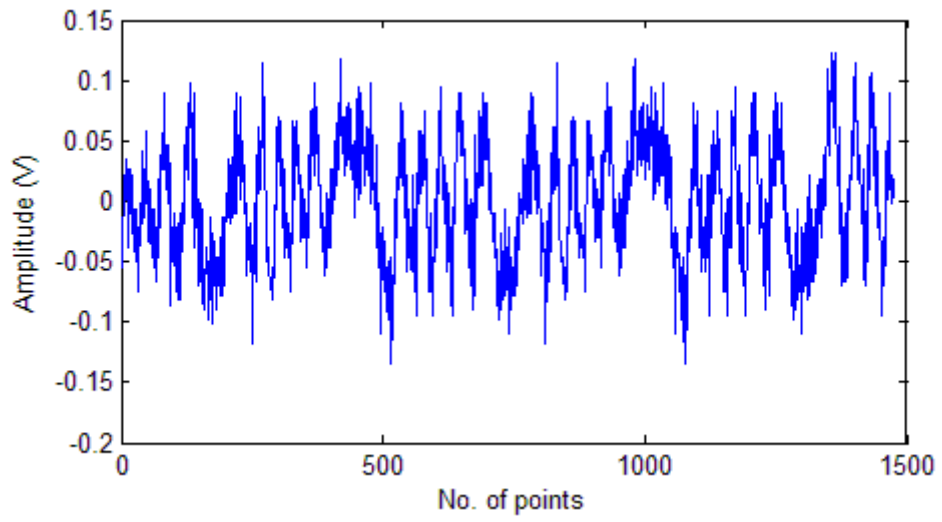
(b)
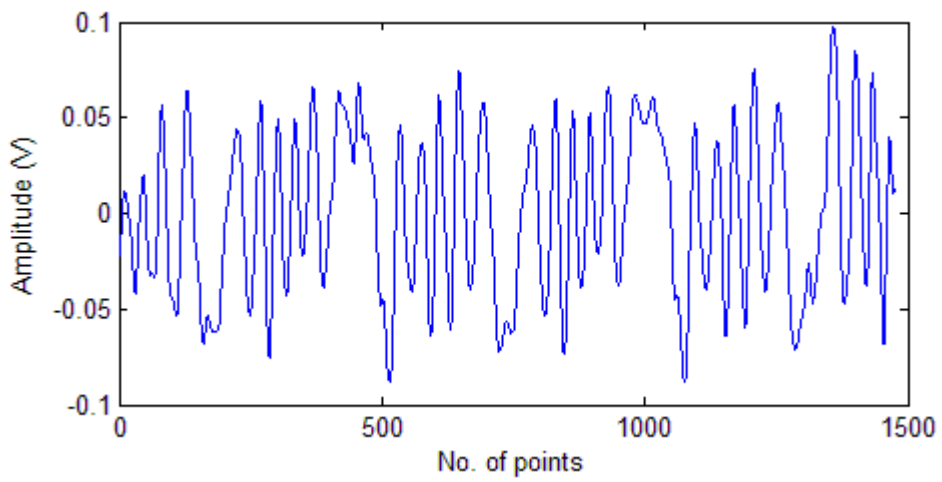
(c)
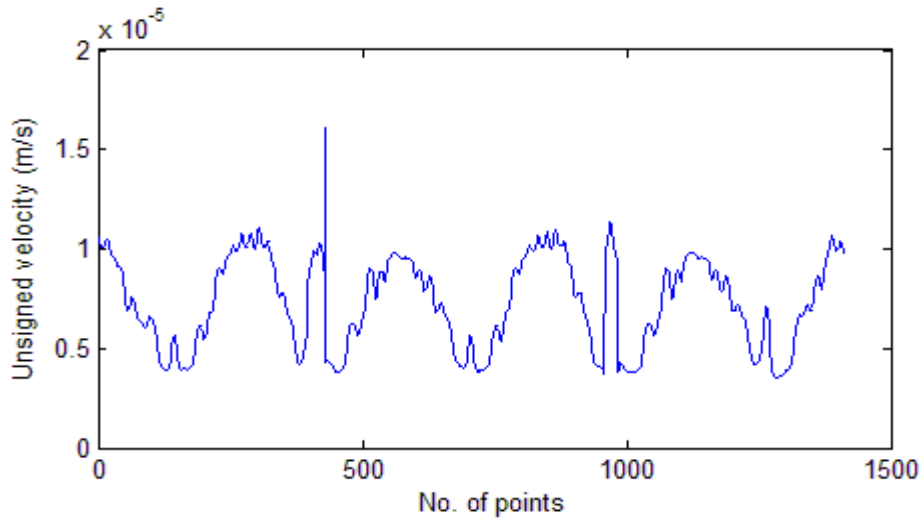
(d)
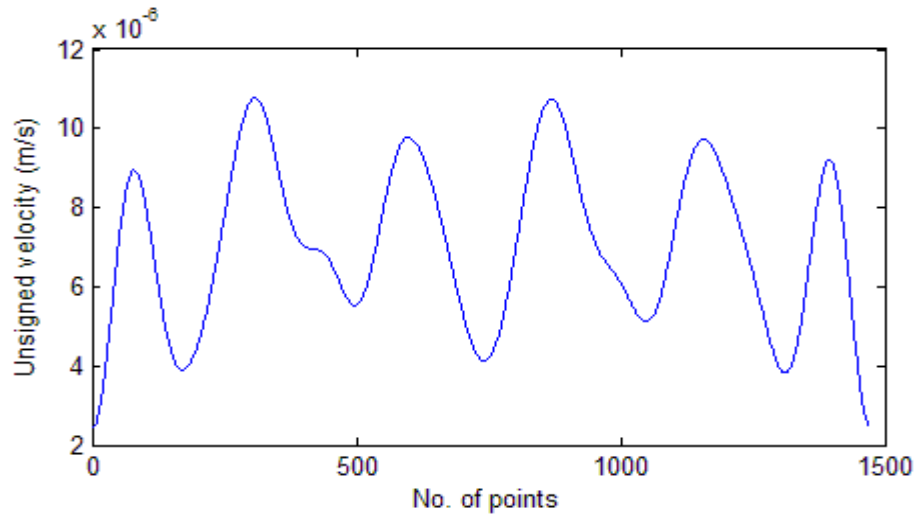
(e)
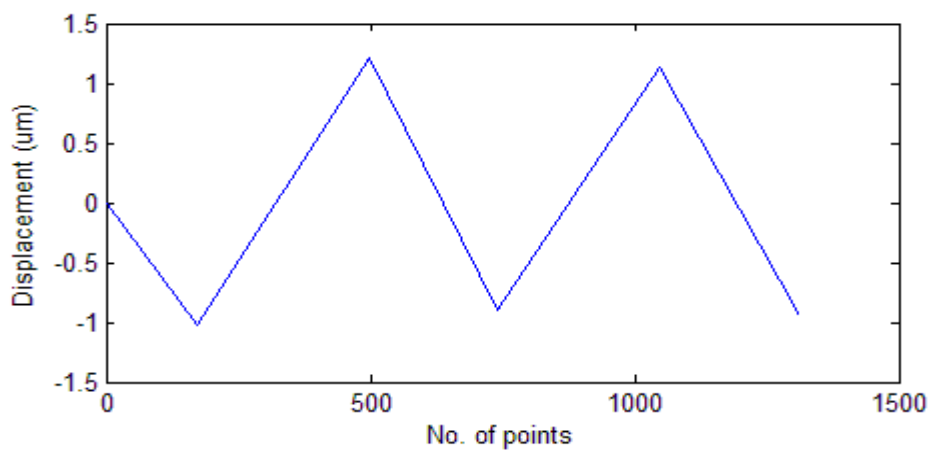
(f)

Figure 40 - (a) Signal driving the target; (b) Noisy self-mixing signal; (c) De-noised self-mixing signal; (d) Unsigned velocity; (e) Unsigned velocity after applying MRA; (f) Reconstructed displacement.

The target, a rough piece of wood stuck on the piezoelectric oscillator, is driven by a 1.74 Hz sine wave. In Figure 40(a), 1475 data points correspond to 1.475 s. In Figure 40(a), at time = 0.438 s (corresponding to point 438), driving signal reaches the first peak. The first valley is at time = 0.169 s (corresponding to point 169). In Figure 40(b), the fringes and changes in direction are visible however the signal has a lot of noise as well. Figure 40(a) and 42(b) are measured using oscilloscope and stored in the flash drive. These data points are then used in the MATLAB program to reconstruct the signal.

De-noising was performed using "wpdencmp" function of the "Wavelet Toolbox" in MATLAB. This function performs a de-noising using wavelet packet. Soft thresholding with symlet wavelet (sym8) was employed for this purpose. The result is presented in Figure 40(c). Figure 40(d) shows the unsigned velocity vector computed.

The unsigned velocity vector contains some unwanted high frequency information. So symlet wavelet ("sym8", level 6) was employed to perform multilevel stationary wavelet decomposition. The result is presented in Figure 40(e).

The direction information is then used to convert unsigned velocity into signed velocity. Hence the direction information yields the interval for the integration. However in the example illustrated in Figure 40, the direction information cannot simply be obtained by differentiating the signal. Here we have made the assumption that the vibration is harmonic. i.e., the unsigned velocity is converted into the signed velocity simply by inverting every alternating pulse of unsigned velocity. For example in Figure 30(b), the velocity datapoints from point b to point c is multiplied by -1. The integration is then performed from point a to point c.

Integration of the velocity results in the displacement as presented in Figure 40(f). As already mentioned in Section 4.2.3.7, the reconstructed signal only has the amplitude of vibration (and not the points in between). In this thesis only peak points are computed. Hence the reconstructed signal in Figure 40(f) looks triangular rather than sinusoidal.

Chapter 5

Phase-locked Self-mixing Vibrometer and Its Application

5.1 Introduction

The principle of phase-locked self-mixing vibrometer is based on the idea of locking the interferometer phase to half fringe. The idea of the phase locked self-mixing vibrometer presented in this thesis is based on the active phase-nulling technique by Giuliani et al (2003).

The self-mixing interferometric phase of the laser diode depends upon the target distance. I.e.

$$\phi = 2kL_{ext}$$

or

$$\phi = 2 \cdot \frac{2\pi}{\lambda_c} L_{ext} \, . \tag{5.1}$$

Differentiating equation (5.1) with respect to L_{ext} and λ_0,

$$\Delta\phi = 2\frac{2\pi}{\lambda_c}\Delta L_{ext} - 2\frac{2\pi}{\lambda_c^2}L_{ext0}\Delta\lambda_0. \tag{5.2}$$

For the phase locked vibrometer, the output is then fed back to keep the phase of the interferometer at a constant value. This implies,

$$\Delta\phi = 0 \, . \tag{5.3}$$

According to equation (5.2), change in target displacement results change in $\Delta\phi$. However this can be compensated by the change in $\Delta\lambda_0$. $\Delta\lambda_0$ required to nullify $\Delta\phi$ can be found from the equation (5.2) as,

$$2\frac{2\pi}{\lambda_c}\Delta L_{ext} - 2\frac{2\pi}{\lambda_c^2}L_{ext0}\Delta\lambda_0 = 0$$

or

$$\Delta\lambda_0 = \frac{\lambda_c}{L_{ext0}}\Delta L_{ext} \, . \tag{5.4}$$

In chapter 2, equation (2.14) shows that the frequency of the laser is inversely proportional to the length of the cavity and the effective refractive index. If we

maintain the temperature of the laser diode constant, the length of the laser diode cavity will remain constant. The refractive index depends on the carrier density (Petermann 1991). Equation (2.20) shows the dependency of laser frequency on the carrier density. This indicates that the laser frequency can be modulated by the injection current. If the closed loop gain and phase of the feedback signal is of the right value, the output phase of the self-mixing interferometer can be maintained at a constant value.

As seen from the equation (5.1), a change in the position of the target changes the interferometric phase. By substituting $\phi = \omega_c \tau_{ext}$ in equation (2.63), we can see the phase variation is proportional to the power variation.
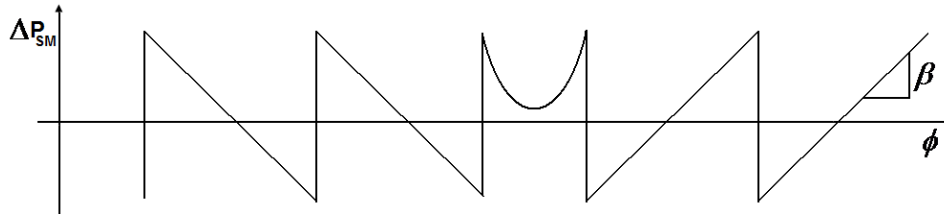
Figure 41 - Approximated self-mixing signal.

The power variation due to the self-mixing effect can be written as

$$\Delta P_{SM} = \beta \Delta \phi \qquad (5.5)$$

where β [W rad^{-1}] is the slope coefficient. The optical power variation is detected and converted into the electrical signal by the built in monitor photodiode. This current signal is then converted into the voltage signal by the transimpedance amplifier:

$$\Delta V = \sigma Z \Delta P_{SM} \qquad (5.6)$$

where ΔV is the voltage signal output from the transimpedance amplifier, σ [AW^{-1}] is the photodiode responsivity and Z [Ω] is the impedance.

The voltage signal coming out from the transimpedance amplifier is then passed through the voltage amplifier with gain A. This is then fed back to the laser diode driver through a voltage controlled current source with admittance of Y[Ω^{-1}].

$$\text{i.e., } \Delta \lambda_0 = \chi \Delta I \qquad (5.7)$$

where χ [nm mA^{-1}] is the modulation efficiency. The signal fed back to the laser diode driver has to be 180^0 out of phase.

5.2   Experimental setup

The experimental setup for the phase locked vibrometer is similar to Figure 15, however the electronic circuit has been modified to achieve phase lock. A single longitudinal mode laser diode (L780P010, Thorlabs, USA) was used for this setup. The wavelength drift and power change versus injection current for the laser diode as illustrated in Figure 43 and Figure 44 was recorded using a wave meter (WA-1150, Burleigh Instruments, Inc., NY, USA). The laser diode was operated at constant temperature of 25^0C ($\pm$ 0.2%) using the TEC2000 thermoelectric temperature controller and the TCLDM9 laser diode mount.
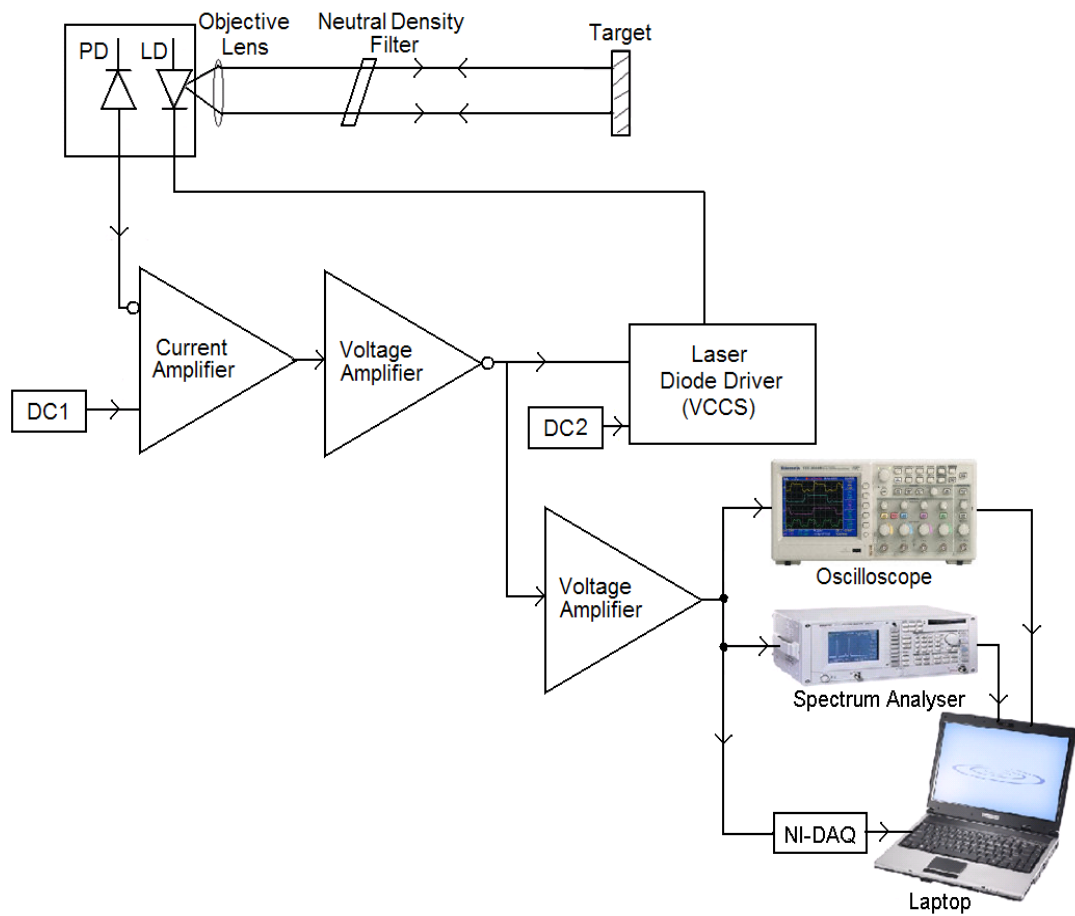
Figure 42 - Block diagram of the phase locked self-mixing vibrometer.
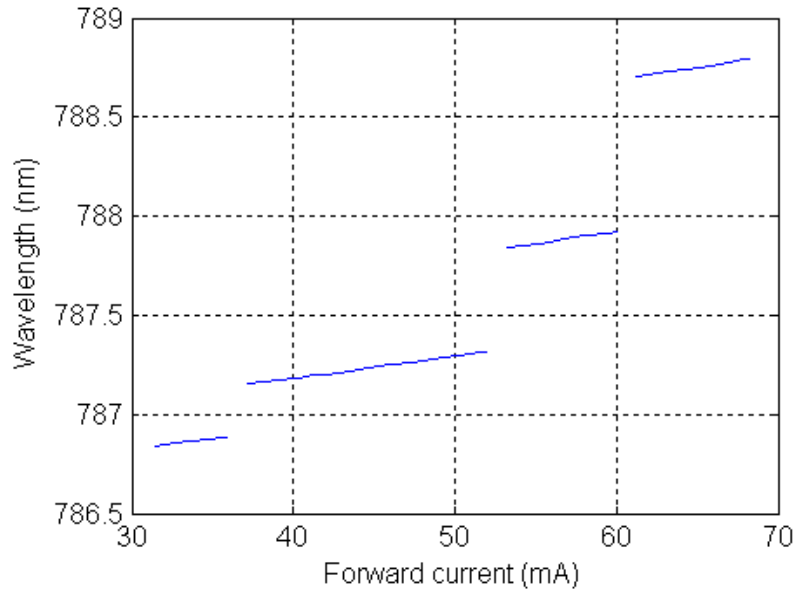
Figure 43 - Wavelength drift versus injection current of L780P010 laser diode.
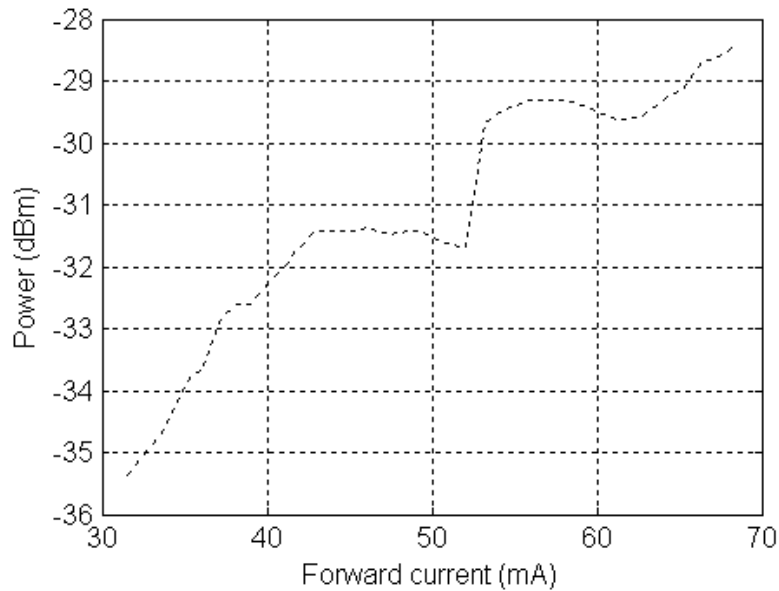
Figure 44 - Output power change versus injection current of L780P010 laser diode.

Except for the electronic circuitry part, the experimental setup for the phase locked vibrometer is exactly same as the setup presented in section 3.1. The electronic circuit used in the setup is briefly described in the following paragraph.

The signal from a photodiode is amplified by the current amplifier. The dc part of the signal is then subtracted using differential amplifier using DC1, which is the dc voltage set equal to the dc part of the signal. The signal from the differential amplifier is then branched into two parts, one to monitor the output and another for the feedback. The signal for monitoring the output is simply passed through

the voltage amplifier to the oscilloscope, spectrum analyser or to the laptop via a NI-DAQ card. The signal used for the feedback is fed to the laser diode driver (LD1255R, Thorlabs, USA). The laser diode driver is the voltage controlled current source. Apart from the signal from the differential amplifier, it has DC2 controlling the output current. DC2 is the dc voltage for generating the operating current of the laser diode (45 mA for this setup). The current generated by the laser diode driver then controls the laser diode.

5.3   Experimental results

The experimental result using the setup presented in Figure 42 is shown in the Figure 45(a-e).
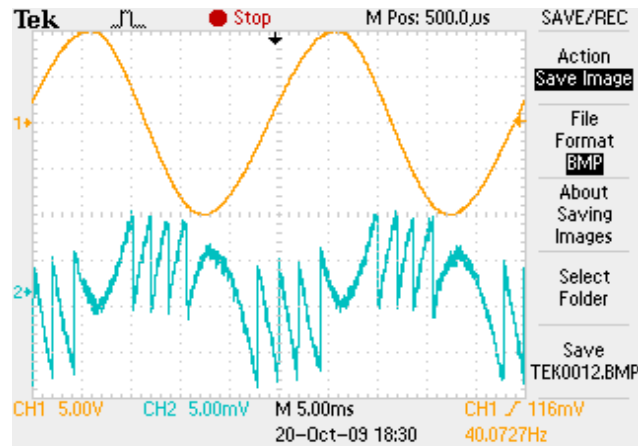
(a)
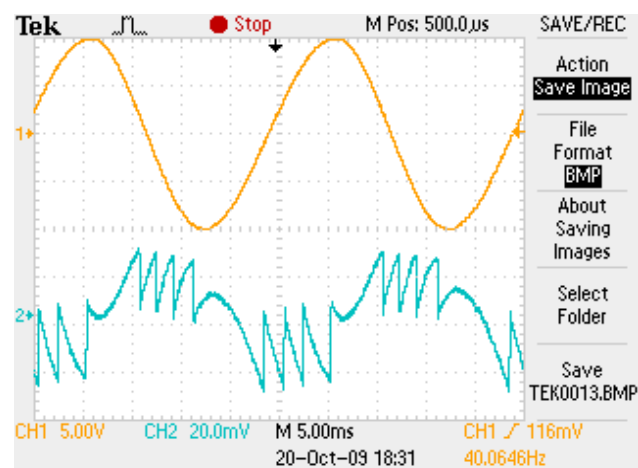
(b)
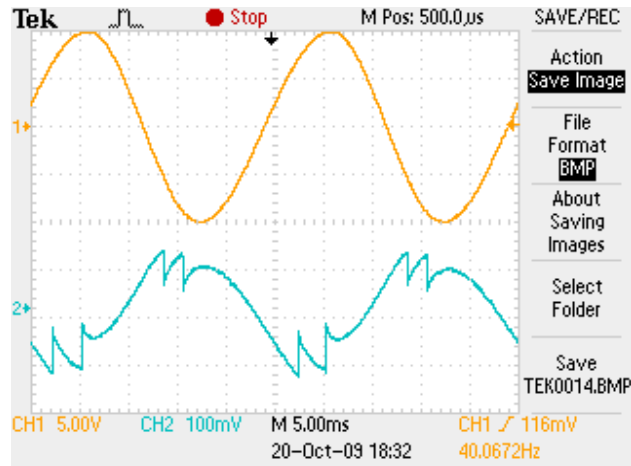
(c)
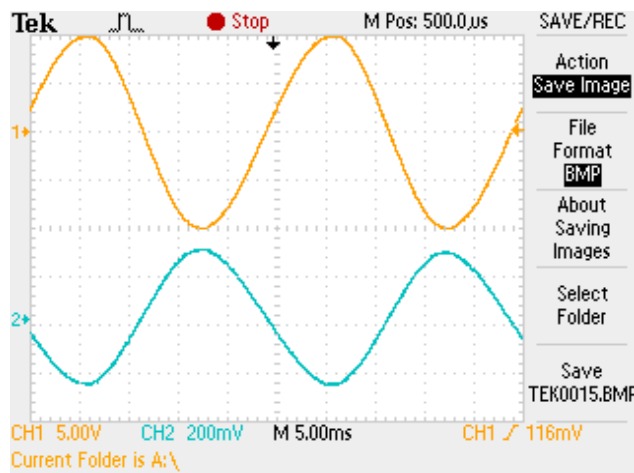
(d)
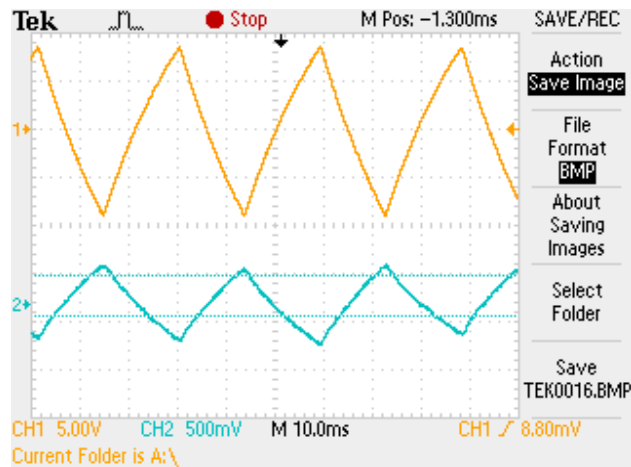
(e)

Figure 45 - (a-e) Upper trace: Signal driving the target; Lower trace: output from self-mixing interferometer.

The target used is a yellow insulation tape stuck on the piezoelectric oscillator driven by the sine wave at 40 Hz. Figure 45(a-e) show the signal driving the target (upper trace) and the self-mixing output signal (lower trace). In Figure

45(a) the vertical scale of the self-mixing signal is 5 mV/division. Slowly the closed loop gain of the circuit is increased. As the gain is increased, the self-mixing signal starts unfolding. The vertical scale of Figure 45(b) of the self-mixing signal is 20 mV/division, that of Figure 45(c) is 100 mV/division and of Figure 45(d) is 200 mV/division. Figure 45(d) shows the phase locked self-mixing signal. Figure 45(e) shows the phase locked self-mixing signal for a triangular driving signal. The final signals (Figure 45(d) and 47(e)) are out of phase to the driving signal which can be simply corrected by using the inverting voltage amplifier.

The vibrometer setup was then calibrated by using the setup without feedback and counting the number of fringes (and multiplying them by $\lambda_0 / 2$) for the set of driving signal voltages. Assuming the piezoelectric oscillator's amplitude was changing linearly with the driving voltage, the target displacement was obtained to be 1 μm for 0.747 V. The maximum and minimum vibrations observed using phase locked vibrometer were 1.574 μm and 1 nm respectively.
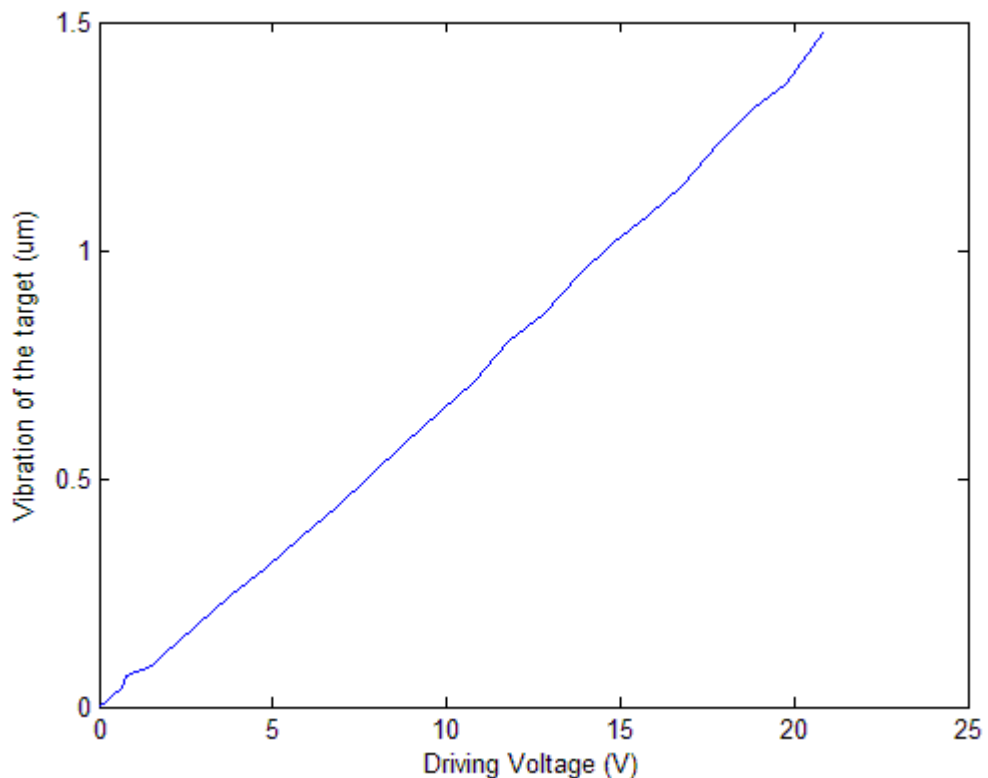
Figure 46 - Input voltage vs measured displacement.

The vibrometer was then tested to measure acoustic vibration. The target used is a yellow insulation tape stuck on the small piece of transparency sheet. Setup for the experiment is shown in Figure 47.
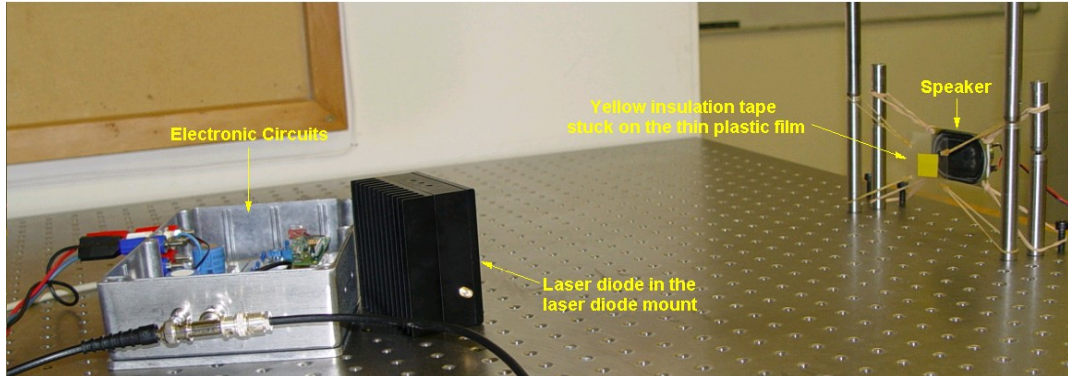
Figure 47 - Experimental setup for the acoustic vibration measurement.

The target is held stretched using rubber strings and is excited by a speaker playing music. The speaker is located right behind the target. The speaker is held in place without touching the target. Rubber strings are used to hold the speaker to prevent the vibration to reach to the target or vibrometer via the optical table. When music is played, the acoustic waves vibrate the target and the vibration is picked up by the laser diode. The self-mixing setup is driven in the phase locked mode so the output is the exact replica of electrical signal of the music. Figure 48 shows the screen shot of the oscilloscope. The upper trace is the speaker signal and the lower trace is the vibrometer output signal. The input signal and output signals are 180^0 out of phase.
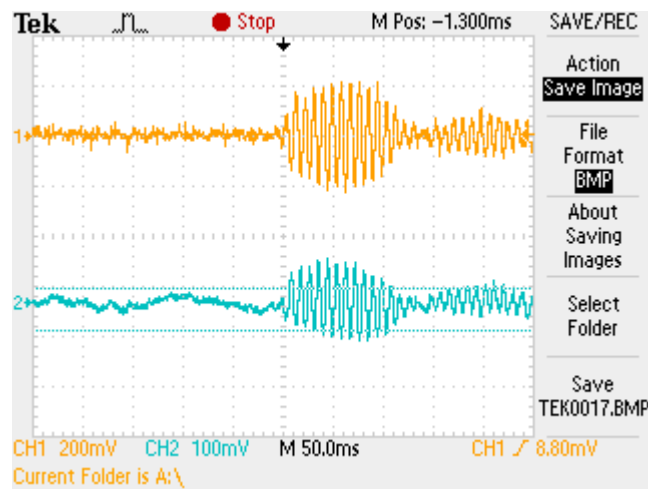
(a)
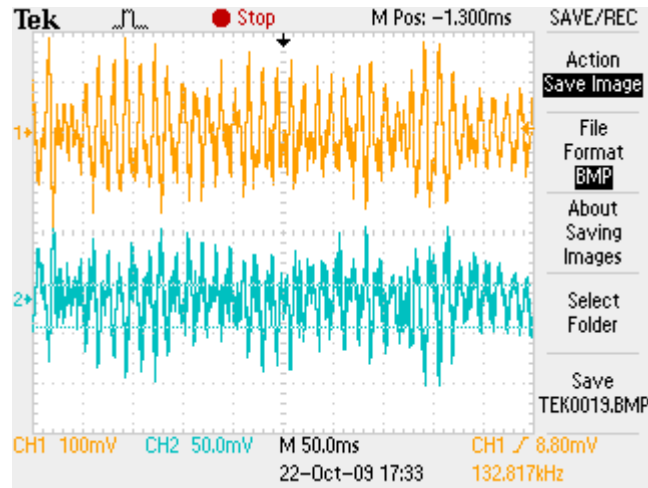
(b)

Figure 48 - (a-b) Upper trace: Speaker signal; Lower trace: vibrometer output signal.

The vibrometer output is then fed to the custom made audio amplifier and to the loudspeaker to listen to the reconstructed music. The music with voice and instruments could be clearly understood.

5.4 Application of the vibrometer for the eggshell crack detection

In this section an application of the phase-locked self-mixing vibrometer for the eggshell crack detection is presented. We propose a novel method for eggshell crack detection. This section begins with a literature review of the eggshell crack detection followed by the experimental setup, results and discussion.

5.4.1 Background

New Zealand's estimated production of eggs in 2008 was 968 million eggs (Egg Producers Federation of New Zealand 2009). In the study of commercial hatcheries, Bell et al. (2002) estimated about 4% of eggs are cracked prior to processing. Cracked eggs are prone to harmful bacteria like *Salmonella* and can risk the health of the consumer. Also leaky eggs contaminate other eggs and mechanical parts of the egg packing and sorting plant.

Egg quality in the egg sorting and packing industry is controlled using a process called candling. Candling is a process in which the eggs are examined against a bright light by human. Candling is a slow process and the inspection is subjective. Therefore, the operation is a bottleneck in the commercial egg-grading machines (De Ketelaere et al. 2000). So an automated sensor capable of differentiating between cracked and intact egg is desirable to improve quality control and increase profitability of the egg producer. The sensor for the eggshell crack detection should have following features:

- The sensor should be non destructive and fast.
- To prevent cross contamination from an infected egg the sensor should be non-contact.
- To ensure high quality it is should have a high crack detection rate.
- To keep the cost of production low, it should have low false rejection rate.

Automation of the candling operation is approached by researchers mainly in two different techniques:

- Mechanical technique; and
- Machine vision technique.

Mechanical Technique:

In this technique, the mechanical behaviour of the eggshell is checked by exciting the eggshell using a small mechanical impactor. In this type of device, the local integrity of the eggshell is examined by measuring the amplitude or the number of rebounds of an impactor on the eggshell. Several elastic rebounds indicate an intact eggshell. The rebounds of the impactor are damped near the crack of the eggshell as the elasticity of the eggshell is highly impaired near this location. Measuring rebounds from several places of the egg, a crack on the eggshell can be detected (De Ketelaere et al. 2000).

Instead of measuring rebounds of the impactor, Coucke (1998) proposed to measure the frequency response of the egg itself. When impacted with a light mechanical impactor around the equator, the frequency response of an intact egg, measured acoustically, around the eggshell equator are identical on different locations. The frequency response of the eggshell at different places of the eggshell equator is non-repetitive for a cracked egg. To detect the crack on

the eggshell, four different measurements taken from the egg around the equator are correlated with each other. Pearson correlation coefficient of value close to 1 is obtained for the intact egg whereas value close to 0 is obtained for the case of a cracked egg (De Ketelaere et al. 2000). Egg vibration after the impact is reported to last only for 10 ms. The authors claim that this technique is fast. Using this technique, the authors report the cracked egg detection to be up to 90% and false reject remaining below 1%.

Coucke et al (2003) excited a chicken egg with a light mechanical impact hammer at 42 different excitation nodes on the eggshell and measured the dynamic mechanical behaviour using a laser vibrometer. The result is illustrated in Figure 49.
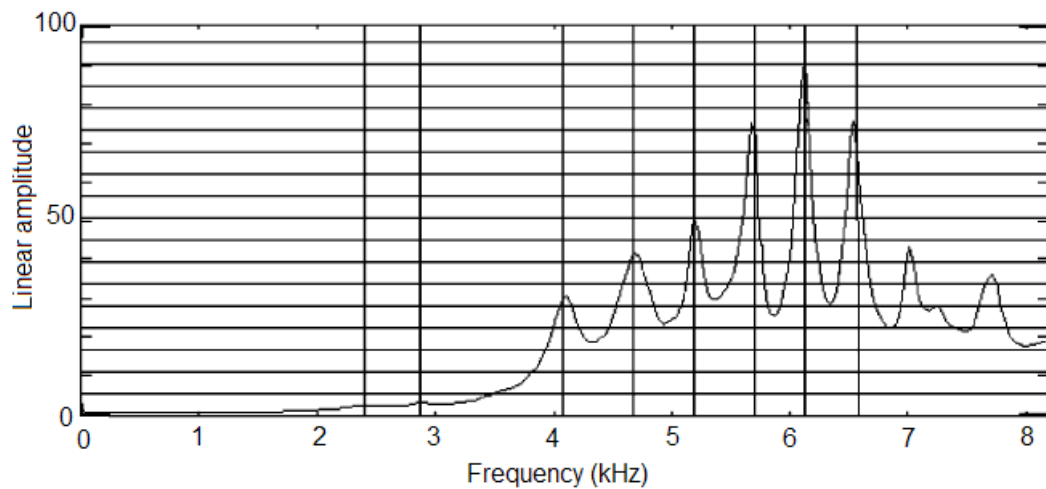
Figure 49 - Frequency response of an intact egg excited by impact hammer (Coucke et al. 2003).

Eggshell crack was detected using acoustic technique by Wang and Jiang (2005) as well. Sinha et al. (1992) conducted the acoustical vibration studies on chicken egg using two piezo electric transducers. This study demonstrated the detection of *Salmonella* bacteria in an egg in a non-invasive way. One piezo electric transducer was used to excite the egg by sweeping the frequency in a range of 400 to 2000 Hz and another transducer was used to record the frequency response. One or two resonance peak below 1250 Hz was reported in a normal egg whereas in the case of an egg infected with *Salmonella* bacteria, at least one resonance peak at a frequency higher than 1250 Hz was reported.

Machine Vision Technique:

Elster and Goodrum proposed machine vision technique to detect open cracks and hairline cracks in stationary egg in 1991. A success rate of 96% is achieved. However, the average time required to classify each egg using this method is 25.3 s (Patel et al. 1998). Later Goodrum and Elster (1992) extended their work to inspect continuously rotating eggs. The authors place an egg on a roller driven at a constant speed of 1.5 rpm. An incandescent lamp is placed below the egg and three images at the interval of 120^0 interval are taken. Then the images are processed to classify the egg as cracked or intact. With this method 94% success rate is achieved in determining the cracks. However, the developed software requires calibration. Using colour computer vision combined with artificial neural networks, Patel et al. (1998) claim the average crack detection of 87.8% (84.4% on eggs with crack and 91.1% on eggs without cracks).

One of the drawbacks of the machine vision technique is the processing time of the computers. With increasing processing speed of modern computers, this technique is looking promising for detection of dirt on the eggshells, broken shells and odd shapes. However undamaged eggs with scratches or calcium deposits are often rejected (De Ketelaere et al. 2000).

Apart from these two techniques spectroscopic techniques are employed for the detection of blood and meat spot in an egg (De Ketelaere et al. 2004).

5.4.2 Experimental setup

If the eggshell is excited at its resonance frequency, a large amplitude vibration of the eggshell can be detected. As mentioned earlier, the elasticity of the eggshell is highly impaired near the crack so the resonance frequency of the eggshell near or on the crack will be different compared to the resonance frequency on the intact part of the egg. In this thesis, instead of exciting an egg with a mechanical impactor, we excite the egg with an acoustic wave. The frequency response of the eggshell is examined using the phase locked vibrometer making the eggshell crack detection process completely non contact.
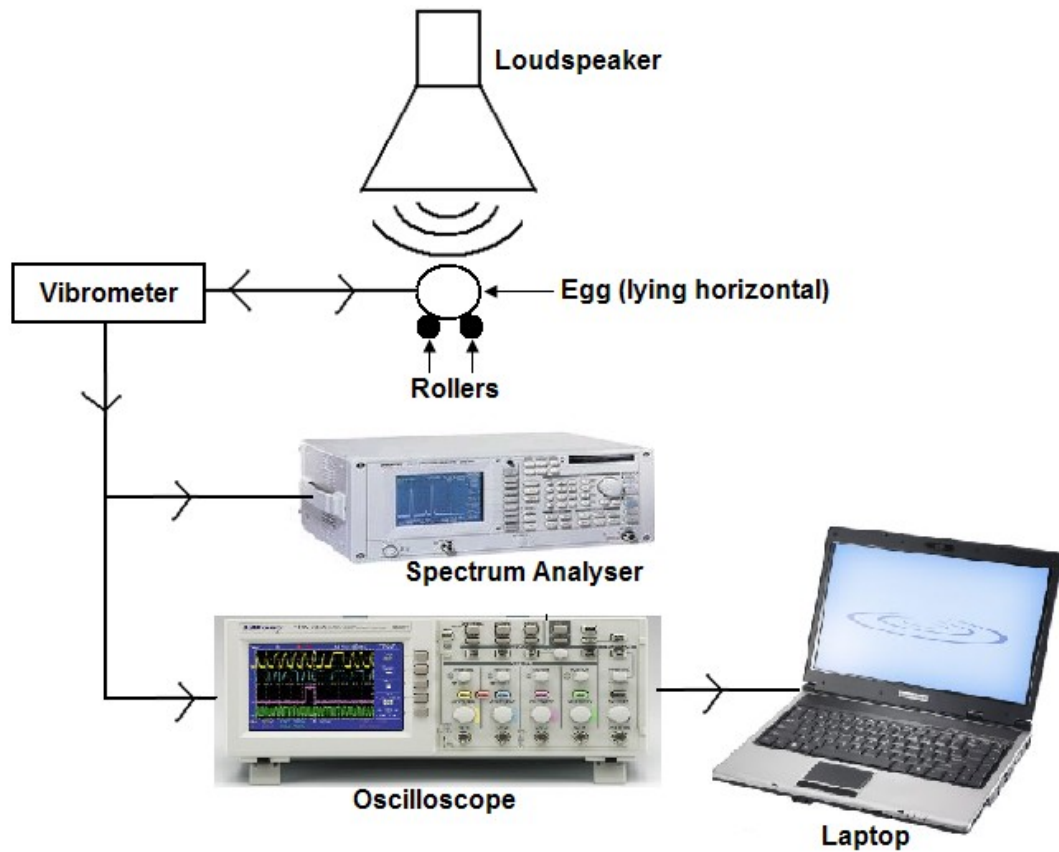
Figure 50 - Block diagram of the experimental setup for the eggshell crack detection using vibrometer.

Figure 50 shows the block diagram and Figure 51 shows a snapshot of the experimental setup for the eggshell crack detection. The phase locked vibrometer described in section 5.2 is used to measure vibration in this setup. A function/arbitrary waveform generator (33220A, Agilent Technologies Inc., USA) is used to generate a sine wave. This sine wave is then amplified using custom made audio amplifier and fed to the loudspeaker. Eggs are supported on the rollers. The rollers are soft compared to the intact eggshell so that influence of the support on the eggshell can be minimised. As shown in Figure 51, egg, roller and vibrometer are placed on the optical table. The loudspeaker is placed on a separate table to minimise transmission of the acoustic wave to an egg via the table.
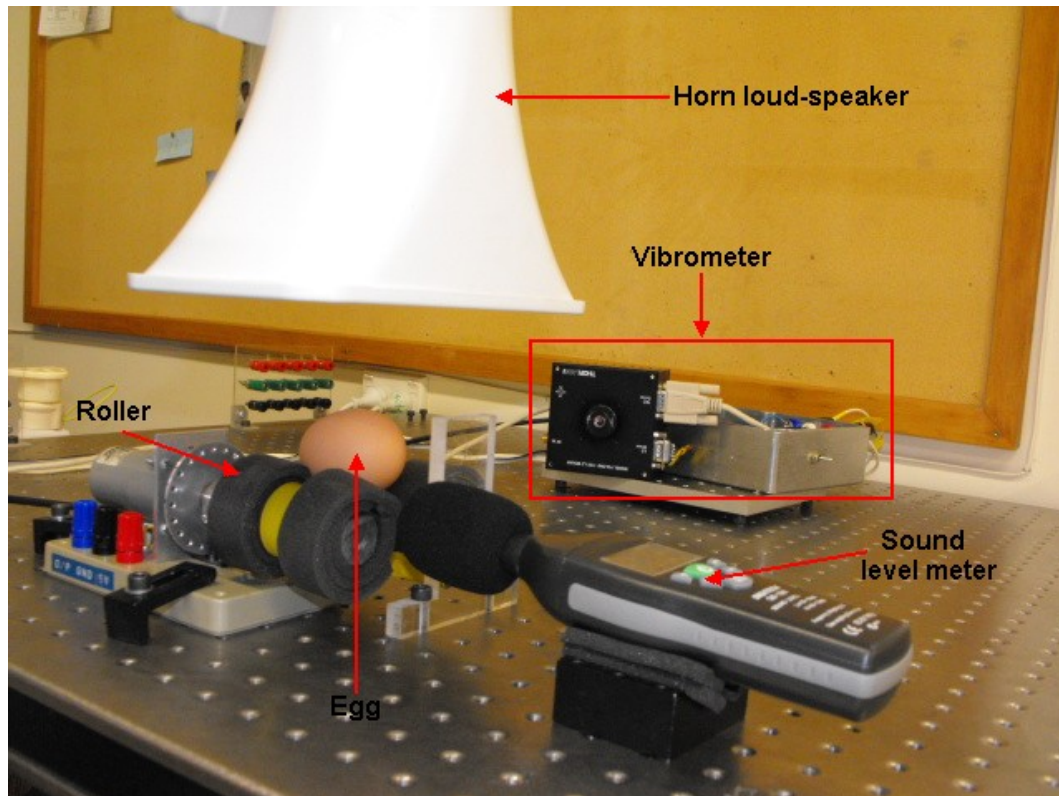
Figure 51 - Snapshot of the experimental setup for the eggshell crack detection using vibrometer.

5.4.3 Results and Discussion

Exciting egg with the white noise excitation signal:

Fresh size 6 eggs with brown shell colour from the local supermarket were used in the experiment. Cracks (from hairline (almost invisible) to few mm) were inflicted on the eggshell in the laboratory for the experiment. The cracks were inflicted on or near the equator and the measurements were also taken from the equator of an egg. The eggs were excited using white noise via a loudspeaker.

Figure 52 (a) shows the frequency response of the intact egg measured using oscilloscope. Figure 52(b) shows the frequency response of the cracked egg with the crack of 0.27 mm width and 28.76 mm length on the equator running from one end to the other end. The measurement is taken with the cracked side facing towards the vibrometer. The result is repeatable with other cracked eggs. It can be clearly observed that the cracked side of the egg exhibits multiple peaks in the frequency spectrum. However, the measurement taken by intact side of the

cracked egg facing towards the vibrometer resembles to Figure 52(a). As mentioned by De Ketelaere et al.(2000), the frequency response of the intact egg is very similar around the different points of the equator.
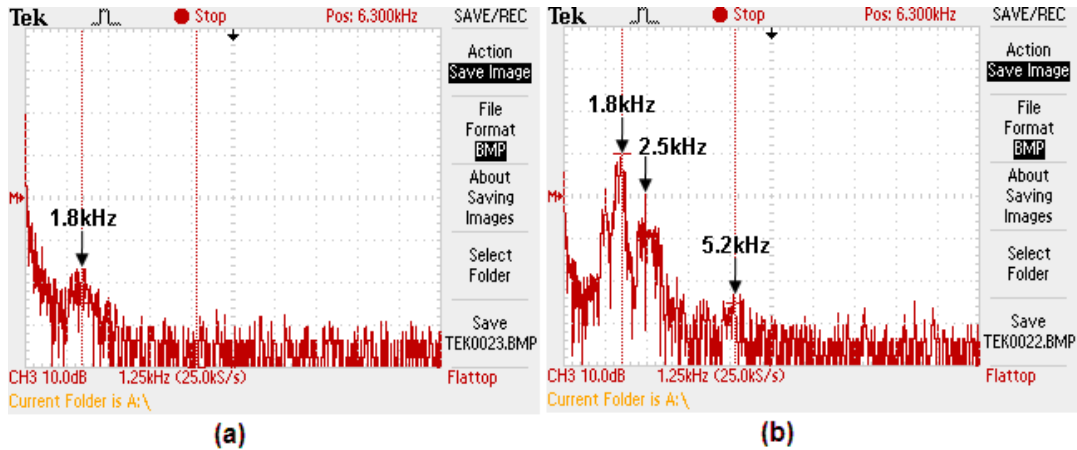
Figure 52 - (a): Frequency response of an intact egg, (b): Frequency response of a cracked egg.

Exciting the egg using different single tone frequencies:

The intact egg was excited using a single tone frequency of 400 Hz to 17 kHz. In the interval of 400 Hz to 13 kHz it was excited in 100 Hz step and for the remaining frequency band it was excited in the step of 500 Hz. The amplitude of vibration was recorded using a spectrum analyser. Each data point is the average of 10 measurements. The sound level was measured using a sound level meter (QM-1589, Digitech, China). The data was then normalised to 100 dBA of sound level. Similarly, cracked egg with cracked part of the egg facing towards vibrometer was excited using the single tone frequency of 400 Hz to 11 kHz in the step of 100 Hz. The cracked egg was only excited up to 11 kHz compared to the 17 kHz of intact egg, as no significant change above 11 kHz was observed. The measurements are illustrated in Figure 53 and Figure 54.
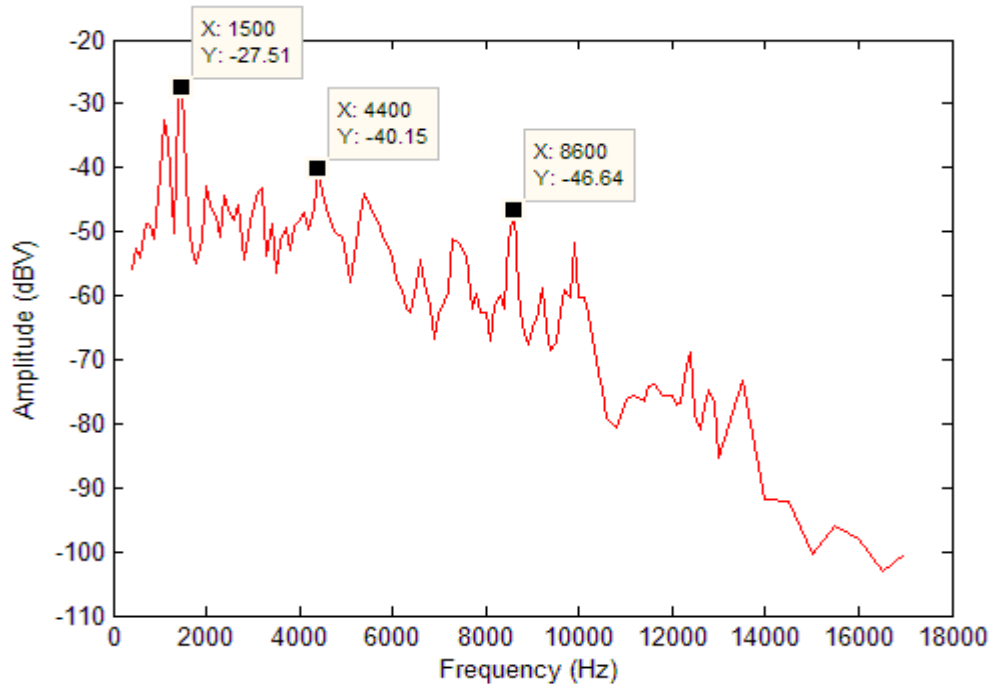
Figure 53 - Exciting the egg using different single tone acoustic waves.
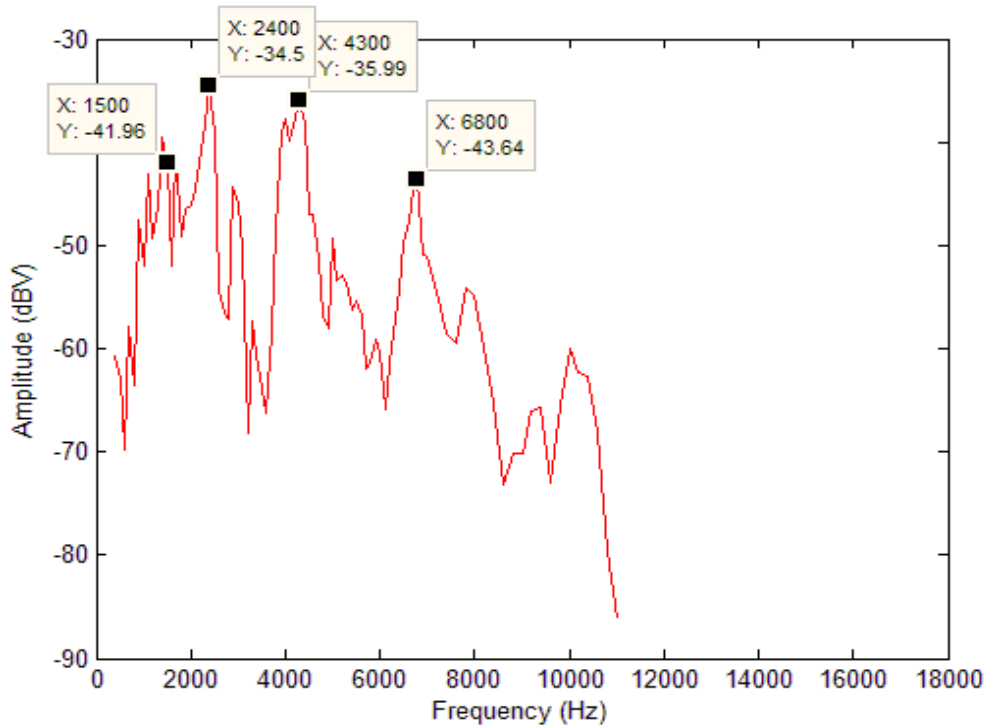
Figure 54 - Exciting the egg using different single tone acoustic waves.

Exciting egg using single tone frequency:

Since the energy content is spread out in the white noise excitation signal, a single tone was preferred to excite the egg. Significant difference between a cracked and intact egg was observed. Two of the results are illustrated in Figure 55 to 58.
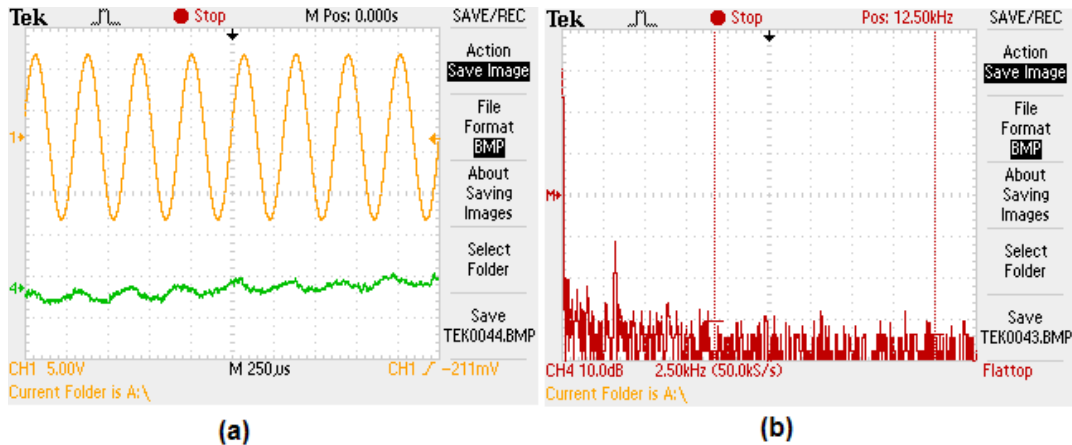
Figure 55 - (a) Time domain signal of an intact egg excited by 3.18 kHz sine wave;
(b) Frequency domain signal of an intact egg excited by 3.18 kHz sine wave.
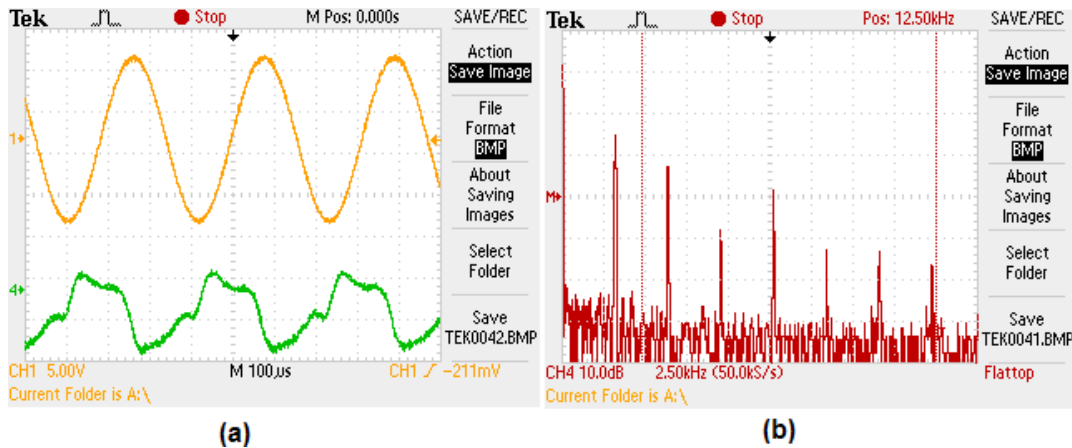
Figure 56 - (a) Time domain signal of a cracked egg excited by 3.18 kHz sine wave;
(b) Frequency domain signal of a cracked egg excited by 3.18 kHz sine wave.

As mentioned earlier, the eggs are size six with brown shell colour. In Figure 55(a), the upper trace represents the excitation signal. The excitation signal is the sine wave of 3.18 kHz and 20 V_{p-p}. The audio level of excitation signal is 101.4 dBA. The lower trace is the vibrometer signal of 38 mV_{p-p} (i.e., 0.05 μm_{p-p} of vibration) of an intact egg. The vertical scale for the upper trace is 5 V/division and the lower trace is 50 mV/division. Figure 55(b) is the FFT of the vibrometer

signal illustrated in Figure 55(a). The cracked egg used in this case has a hairline crack of 21.93 mm on the equator region running from one end to the other end. Figure 56(a) is the time domain signal observed in the cracked egg with the cracked side facing towards the vibrometer. The upper trace is the excitation signal of 20 V_{p-p}. The lower trace is the vibrometer signal of 204 mV_{p-p} i.e. 0.27 μm_{p-p}. The vertical scale for the upper trace is 5 V/division and the lower trace is 100 mV/division. Figure 56(b) is the FFT of the vibrometer signal illustrated in Figure 56(a). We can see the clear difference between the signal obtained from the cracked and the intact egg.

Figure 57 and 60 depict more example of the intact and cracked egg excited by the sine wave of 1.78 kHz and sound level of 126.7 dBA. In Figure 57(a), the upper trace is the excitation signal and the lower trace is the vibrometer signal of 100 mV_{p-p} i.e. 0.14 μm_{p-p} of vibration. The vertical scale for the upper trace is 5 V/division and the lower trace is 100 mV/division. Figure 57(b) is the FFT of the vibrometer signal illustrated in Figure 57(a). The upper trace of Figure 58(a) is the excitation signal and the lower trace is the vibrometer signal from the cracked egg with cracked part facing towards the vibrometer. The cracked area in this case is 25.43 mm wide and 30.40 mm long with multiple cracks in it. The vibrometer signal obtained is not locked as the peak to peak vibration of the cracked eggshell is beyond the range of our vibrometer. The vertical scale for the upper trace is 5 V/division and the lower trace is 100 mV/division. Figure 58(b) is the FFT of the vibrometer signal illustrated in Figure 58(a).

Figure 57 - (a) Time domain signal of an intact egg excited by 1.78 kHz sine wave; (b) Frequency domain signal of an intact egg excited by 1.78 kHz sine wave.
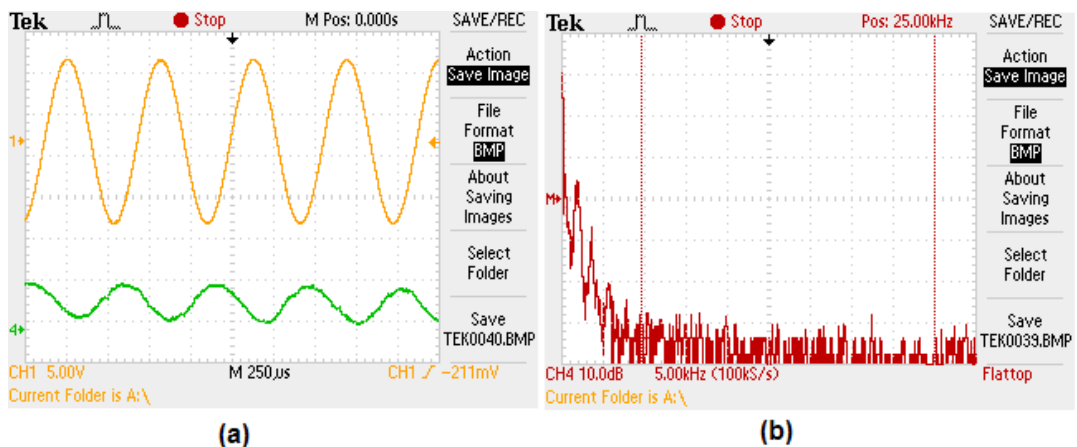
Figure 58 - (a) Time domain signal of a cracked egg excited by 1.78 kHz sine wave;
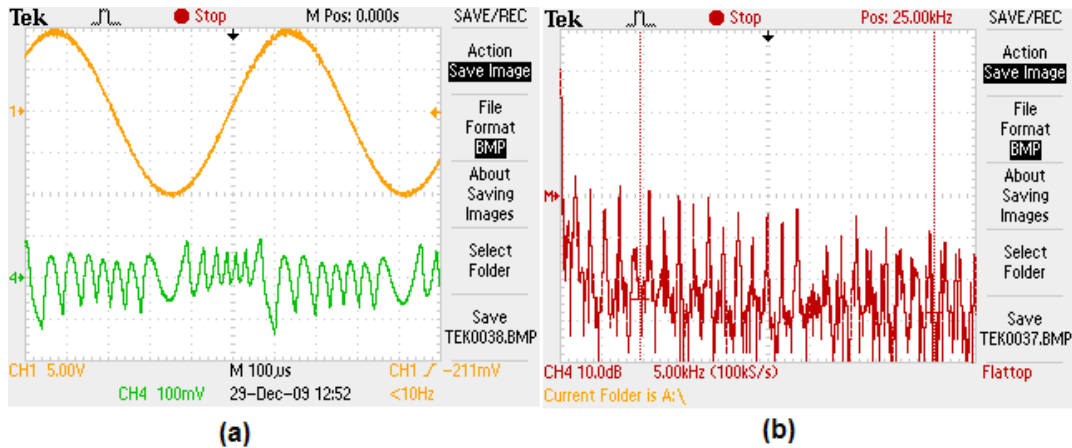**(b) Frequency domain signal of a cracked egg excited by 1.78 kHz sine wave.**

An algorithm to differentiate the cracked egg from an intact egg was developed based on the paper by De Ketelaere et al. (2000). Data acquisition and programming was done in the LabVIEW. The oscilloscope was connected to the laptop using USB and data was collected using LabVIEW Virtual Instrument (VI). Another VI was written to read the stored data from the files and to compute FFT of the signals and to compute the correlation.

Five sets of data were collected for each egg by rotating the egg each time by 72^0 and taking the measurement. Data from the intact side of the eggshell resembles Figure 55(b) and the data from the cracked side of the eggshell resembles Figure 56(b). Pearson correlation coefficients for ten different combinations from five data sets were computed. For an intact egg, the obtained Pearson correlation coefficient is close to 1 whereas for a cracked egg, it is close to 0. If the lowest correlation coefficient obtained was less than the chosen threshold value, then the egg was classified as cracked. The threshold value was set to be 0.3 for this experiment. The experiment was conducted in five intact and five cracked egg. The program was able to distinguish the cracked egg from the intact egg.

There is more room to develop a better algorithm as the excitation signal can be modulated as desired. The threshold value to classify the egg as a cracked egg can be optimised and the statistical study can be carried out to see the effectiveness of a system. However, our experiment is limited just to detect the crack on the eggshell due to time constraints. A crack on the eggshell is detected very easily down to hairline (almost invisible) cracks. However, one has to

measure the vibration closer to the crack. This in fact will determine the number of measurement required to detect the crack on an eggshell. Also it is important to mention that even though the egg was rotated on the roller, it was kept stationary during the time of excitation and measurement.

Chapter 6

Conclusion

The main objectives of this thesis as mentioned in chapter one, were to investigate and develop the self-mixing diode laser interferometer, reconstruct the target movement and apply the interferometry to the eggshell crack detection. The objectives were addressed in consecutive chapters. Chapter two performed the theoretical analysis of the self-mixing interferometry. The instrument was developed and results were recorded in chapter three. The results of the instrument were found to be in good agreement with the analytical results stated in chapter two. We developed three different algorithms in chapter four to reconstruct the target movement. This chapter goes through the background theory, algorithm and experimental results of each method.

The purpose of this research was to develop a self-mixing interferometer without directional ambiguity. However, when used with non-cooperative target, the self-mixing signal can lose the direction information or at least it can be very difficult to retrieve it. To overcome this problem, the phase locked interferometer was developed in the first part of chapter five. This interferometer was able to follow target movement without any additional circuitry. It was also able to measure below sub-wavelength (up to 1 nm) compared to the half of wavelength of normal self-mixing interferometer. However, dynamic range of this interferometer has a big room for improvement.

Finally in the second part of chapter five, the interferometer developed was applied for the eggshell crack detection. The crack on the eggshell was detected successfully. The research can be extended in few more areas, such as; statistical study can be carried out for crack detection rate and false rejection rate. The amount of time required to classify each egg as cracked or intact can be figured out and, algorithm for real time and online system can be developed.

References

Acket, G. A., D. Lenstra, A. J. den Boef and B. H. Verbeek. 1984. The influence of feedback intensity on longitudinal mode properties and optical noise in index-guided semiconductor lasers. *IEEE Journal of Quantum Electronics* QE-20(10) 1163-9.

Bell, D. D., W. D. Weaver and M. O. North. 2002. *Commercial chicken meat and egg production*. Norwell, Mass.: Kluwer Academic Publishers

Bosch, T., N. Servagent and S. Donati. 2001. Optical feedback interferometry for sensing application. *Optical Engineering* 40(1) 20-7.

Callan, E. A. and J. G. McInerney. 1992. Measurement of velocities by backscatter modulation in semiconductor injection lasers. *Proc. of SPIE* 1634 509-19.

Chapra, S. C. and R. P. Canale. 2002. *Numerical methods for engineers : with software and programming applications*. Boston: McGraw-Hill

Chui, C. K., L. Montefusco and L. Puccio. 1994. *Wavelets: theory, algorithms, and applications*, *Wavelet analysis and its applications, v. 5*. San Diego, Calif.: Academic Press

Coucke, P. 1998. Assessment of some physical quality parameters of eggs based on vibration analysis. Thesis or Dissertation thesis, Faculteit Landbouwkundige en Toegepaste Biologische Wetenschappen, Katholieke Univ. Leuven (Belgium), Leuven (Belgium).

Coucke, P., B. De Ketelaere and J. De Baerdemaeker. 2003. Experimental analysis of the dynamic, mechanical behaviour of a chicken egg. *Journal of Sound and Vibration* 266(3) 711-21.

Daubechies, I. 1992. *Ten lectures on wavelets*. Philadelphia, PA: Society for Industrial and Applied Mathematics

de Groot, P. J., G. M. Gallatin and S. H. Macomber. 1988. Ranging and velocimetry signal generation in a backscatter-modulated laser diode. *Applied Optics* 27(21) 4475-80.

De Ketelaere, B., F. Bamelis, B. Kemps, E. Decuypere and J. De Baerdemaeker. 2004. Non-destructive measurements of the egg quality. *World's Poultry Science Journal* 60(03) 289-302.

De Ketelaere, B., P. Coucke and J. De Baerdemaeker. 2000. Eggshell Crack Detection based on Acoustic Resonance Frequency

Analysis. *Journal of Agricultural Engineering Research* 76(2) 157-63.

de Mul, F. F. M., M. H. Koelink, A. L. Weijers, J. Greve, J. G. Aarnoudse, R. Graaff and A. C. M. Dassel. 1992. Self-mixing laser-Doppler velocimetry of liquid flow and of blood perfusion in tissue. *Applied Optics* 31(27) 5844-51.

Debnath, L. 2002. *Wavelet transforms and their applications*. Boston Birkhauser

Donati, S. 1978. Laser interferometry by induced modulation of cavity field. *Journal of Applied Physics* 49(2) 495-7.

Donati, S. 2004. *Electro-optical instrumentation : sensing and measuring with lasers*. Upper Saddle River, NJ: Prentice Hall

Donati, S., L. Falzoni and S. Merlo. 1996. A PC-interfaced, compact laser-diode feedback interferometer for displacement measurements. *IEEE Transactions on Instrumentation and Measurement* 45(6) 942-4.

Donati, S., G. Giuliani and S. Merlo. 1995. Laser diode feedback interferometer for measurement of displacements without ambiguity. *IEEE Journal of Quantum Electronics* 31(1) 113-9.

Donati, S., M. Norgia and G. Giuliani. 2006. Self-mixing differential vibrometer based on electronic channel subtraction. *Applied Optics* 45(28) 7264-8.

Donoho, D. L. 1993. Nonlinear wavelet methods for recovery of signals, densities, and spectra from indirect and noisy data, San Antonio, TX, United states, Publ by Am Math Soc, pp. 173-.

Donoho, D. L. 1995. De-noising by soft-thresholding. *IEEE Transactions on Information Theory* 41(3) 613-27.

Drain, L. E. 1980. *The laser doppler technique*. New York: J. Wiley

Egg Producers Federation of New Zealand. 2009. Egg Quality. http://www.eggfarmers.org.nz/egg-quality.asp (accessed 22 December 2009).

Giuliani, G., S. Bozzi-Pietra and S. Donati. 2003. Self-mixing laser diode vibrometer. *Measurement Science & Technology* 14(1) 24-32.

Giuliani, G., M. Norgia and S. Donati. 2008. Self-mixing laser diode vibrometer for the measurement of differential displacements. *Proc. of SPIE* 7098 709814.

Giuliani, G., M. Norgia, S. Donati and T. Bosch. 2002. Laser diode self-mixing technique for sensing applications. *Journal of Optics A: Pure and Applied Optics* 4(6) 283-94.

Goodrum, J. W. and R. T. Elster. 1992. Machine vision for crack detection in rotating eggs. *Transactions of the American Society of Agricultural Engineers* 35(4) 1323-8.

Gregory, M., S. Noel and B. Thierry. 2000. Distance measurement using the self-mixing effect in a three-electrode distributed Bragg reflector laser diode. *Optical Engineering* 39(3) 738-43.

Halliday, D., R. Resnick and J. Walker. 2003. *Fundamentals of physics. Pt. 1*. New York: Wiley

Halliday, D., J. Walker and R. Resnick. 2000. *Fundamental of physics, extended*. New York: Wiley

Hast, J., R. Myllyla, H. Sorvoja and J. Miettinen. 2002a. Arterial pulse shape measurement using self-mixing effect in a diode laser. *Quantum Electronics* 32(11) 975-80.

Hast, J., R. Myllyla, H. Sorvoja and J. Miettinen. 2002b. Comparison between the elasticity of the arterial wall and pulse wave velocity using the laser Doppler method. *Proc. of SPIE* 4619 259-68.

Hecht, J. 2008. *Understanding Lasers An Entry-level Guide*. Third ed. Hoboken, NJ: IEEE

Jentink, H. W., F. F. M. de Mul, H. E. Suichies, J. G. Aarnoudse and J. Greve. 1988. Small laser Doppler velocimeter based on the self-mixing effect in a diode laser. *Applied Optics* 27(2) 379-85.

Jentink, H. W., J. A. J. van Beurden, M. A. Helsdingen, F. F. M. de Mul, H. E. Suichies, J. G. Aarnoudse and J. Greve. 1987. A compact differential laser Doppler velocimeter using a semiconductor laser. *Journal of Physics E (Scientific Instruments)* 20(10) 1281-3.

Jong Sup, S. and S. Shylo. 2004. Compact vibration sensor for testing sub-resonance of slim optical pickup actuators. *Proc. of SPIE* 5532 332-9.

Karasik, A. Y., B. S. Rinkevichius and V. A. Zubov. 1995. *Laser interferometry principles*, *Advances in science and technology*. Boca Raton: Mir Publishers ; CRC Press

King, P. and G. Steward. 1963. Metrology with an optical laser. *New Scientist* 17 180.

Koelink, M. H., M. Slot, F. F. de Mul, J. Greve, R. Graaff, A. C. M. Sassel and J. G. Aarnoudse. 1992a. Glass-fibre self-mixing diode-laser Doppler velocimeter. *Measurement Science & Technology* 3(1) 33-7.

Koelink, M. H., M. Slot, F. F. M. de Mul, J. Greve, R. Graaff, A. C. M. Dassel and J. G. Aarnoudse. 1992b. Laser Doppler velocimeter based on the self-mixing effect in a fiber-coupled semiconductor laser: theory. *Applied Optics* 31(18) 3401-8.

Lang, R. and K. Kobayashi. 1980. External optical feedback effects on semiconductor injection laser properties. *IEEE Journal of Quantum Electronics* QE-16(3) 347-55.

Mallat, S. G. 1989. A theory for multiresolution signal decomposition: the wavelet representation. *IEEE Transactions on Pattern Analysis and Machine Intelligence* 11(7) 674-93.

Meigas, K., H. Hinrikus, R. Kattai and J. Lass. 2003. Self-mixing in a diode laser as a method for cardiovascular diagnostics. *Journal of Biomedical Optics* 8(1) 152-60.

Merlo, S. and S. Donati. 1997. Reconstruction of displacement waveforms with a single-channel laser-diode feedback interferometer. *IEEE Journal of Quantum Electronics* 33(4) 527-31.

Norgia, M., G. Giuliani and S. Donati. 2004. New absolute distance interferometric technique. *Proceedings of SPIE - The International Society for Optical Engineering* 5457 423-31.

Norgia, M. and C. Svelto. 2008. Novel measurement method for signal recovery in optical vibrometer. *IEEE Transactions on Instrumentation and Measurement* 57(8) 1703-7.

Ozdemir, S. K., I. Ohno and S. Shinohara. 2008. A comparative study for the assessment on blood flow measurement using self-mixing laser speckle interferometer. *IEEE Transactions on Instrumentation and Measurement* 57(2) 355-63.

Ozdemir, S. K., S. Takamiya, S. Ito, S. Shinohara and H. Yoshida. 1999. Blood flow measurements using self-mixing laser diode: effect of hematocrit level and background reflectance on measurements. *Pacific Rim Conference on Lasers and Electro-Optics, CLEO*, Piscataway, NJ, USA, IEEE, pp. 1008-9.

Patel, V. C., R. W. McClendon and J. W. Goodrum. 1998. Color computer vision and artificial neural networks for the detection of defects in poultry eggs. *Artificial Intelligence Review* 12(1-3) 163-76.

Peled, A. and B. Liu. 1976. *Digital signal processing: theory, design, and implementation*. New York: Wiley

Petermann, K. 1991. *Laser diode modulation and noise*. Dordrecht, Netherlands: Kluwer

Porta, P. A., D. P. Curtin and J. G. McInerney. 2002. Laser Doppler velocimetry by optical self-mixing in vertical-cavity surface-emitting lasers. *IEEE Photonics Technology Letters* 14(12) 1719-21.

Poularikas, A. D. 1996. *The transforms and applications handbook*, *The electrical engineering handbook series*. Boca Raton: CRC Press

Raoul, X., T. Bosch, G. Plantier and N. Servagent. 2004. A double-laser diode onboard sensor for velocity measurements. *IEEE Transactions on Instrumentation and Measurement* 53(1) 95-101.

Robertson, D. C., O. I. Camps, J. S. Mayer and W. B. Gish. 1996. Wavelets and electromagnetic power system transients. *IEEE Transactions on Power Delivery* 11(2) 1050-8.

Rovati, L. and F. Docchio. 1998. Low-coherence interferometry using a self-mixing super-luminescent diode. *IEEE Photonics Technology Letters* 10(1) 123-5.

Rudd, M. J. 1968. A laser Doppler velocimeter employing the laser as a mixer-oscillator. *Journal of Physics E (Scientific Instruments)* 1(7) 723-6.

Saleh, B. E. A. and M. C. Teich. 1991. *Fundamentals of photonics*, *Wiley series in pure and applied optics*. New York: Wiley

Scalise, L., W. Steenbergen and F. de Mul. 2001. Self-mixing feedback in a laser diode for intra-arterial optical blood velocimetry. *Applied Optics* 40(25) 4608-15.

C-program to dump data from a 3561 DSA, using VISA bus protocol.

Servagent, N., F. Gouaux and T. Bosch. 1998. Measurements of displacement using the self-mixing interference in a laser diode. *Journal of Optics* 29(3) 168-73.

Shibata, T., S. Shinohara, H. Ikeda, H. Yoshida and M. Sumi. 1999. Automatic measurement of velocity and length of moving plate using self-mixing laser diode. *IEEE Transactions on Instrumentation and Measurement* 48(6) 1062-7.

Shimizu, E. T. 1987. Directional discrimination in the self-mixing type laser Doppler velocimeter. *Applied Optics* 26(21) 4541-4.

Shinohara, S., A. Mochizuki, H. Yoshida and M. Sumi. 1986. Laser Doppler velocimeter using the self-mixing effect of a semiconductor laser diode. *Applied Optics* 25(9) 1417-19.

Shinohara, S., H. Naito, H. Yoshida, H. Ikeda and M. Sumi. 1989. Compact and versatile self-mixing type semiconductor laser Doppler velocimeters with direction-discrimination circuit, USA, pp. 574-7.

Sinha, D. N., R. G. Johnston, W. K. Grace and C. L. Lemanski. 1992. Acoustic resonances in chicken eggs. *Biotechnology Progress* 8(3) 240-3.

Suzuki, T., S. Hirabayashi, O. Sasaki and T. Maruyama. 1999. Self-mixing type of phase-locked laser diode interferometer. *Optical Engineering* 38(3) 543-8.

Tucker, J. R., J. L. Baque, Y. L. Lim, A. V. Zvyagin and A. D. Rakic. 2007. Parallel self-mixing imaging system based on an array of vertical-cavity surface-emitting lasers. *Applied Optics* 46(25) 6237-46.

Wang, J. and R. Jiang. 2005. Eggshell crack detection by dynamic frequency analysis. *Zeitschrift Fur Lebnsmittel Untersuchung Und Forschung* A221(1-2) 214-20.

Wang, M., M. Lu, H. Hao and J. Zhou. 2006. Statistics of the self-mixing speckle interference in a laser diode and its application to the measurement of flow velocity. *Optics Communications* 260(1) 242-7.

Wang, M., T. Sato, G. Lai and S. Shinohara. 2000. Self-mixing interferometry for distance and displacement measurement by Fourier transform method. *Proc. of SPIE* 3945 193-200.

Wang, W. M., W. J. O. Boyle, K. T. V. Grattan and A. W. Palmer. 1993. Self-mixing interference in a diode laser: experimental observations and theoretical analysis. *Applied Optics* 32(9) 1551-8.

Wolfson, R. and J. M. Pasachoff. 1990. *Physics : extended with modern physics*. Glenview, Ill.: Scott, Foresman/Little, Brown Higher Education

Zakian, C., M. Dickinson and T. King. 2005. Particle sizing and flow measurement using self-mixing interferometry with a laser diode. *Journal of Optics A: Pure and Applied Optics* 7(6) 445-52.